Lithium-ion Battery Modeling Using Non-equilibrium Thermodynamics

by

Todd R. Ferguson

B.S., Rensselaer Polytechnic Institute (2008)

Submitted to the Department of Chemical Engineering
in partial fulfillment of the requirements for the degree of

Doctor of Philosophy in Chemical Engineering

at the

MASSACHUSETTS INSTITUTE OF TECHNOLOGY

February 2014

Author .....
Department of Chemical Engineering
November 15, 2013

Certified by .....
Martin Z. Bazant
Professor
Thesis Supervisor

Accepted by .....
Patrick S. Doyle
Graduate Officer

Lithium-ion Battery Modeling Using Non-equilibrium Thermodynamics

by

Todd R. Ferguson

Submitted to the Department of Chemical Engineering
on November 15, 2013, in partial fulfillment of the
requirements for the degree of
Doctor of Philosophy in Chemical Engineering

Abstract

The focus of this thesis work is the application of non-equilibrium thermodynamics in lithium-ion battery modeling. As the demand for higher power and longer lasting batteries increases, the search for materials suitable for this task continues. Traditional battery modeling uses dilute solution kinetics and a fit form of the open circuit potential to model the discharge. This work expands on this original set of equations to include concentrated solution kinetics as well as thermodynamics-based modeling of the open circuit potential. This modification is advantageous because it does not require the cell to be built in order to be modeled. Additionally, this modification also allows phase separating materials to be modeled directly using phase field models. This is especially useful for materials such as lithium iron phosphate and graphite, which are currently modeled using a fit open circuit potential and an artificial phase boundary (in the case of lithium iron phosphate).

This thesis work begins with a derivation of concentrated solution theory, beginning with a general reaction rate framework and transition state theory. This derivation includes an overview of the thermodynamic definitions used in this thesis. After the derivation, transport and conduction in porous media are considered. Effective transport properties for porous media are presented using various applicable models. Combining concentrated solution theory, mass conservation, charge conservation, and effective porous media properties, the modified porous electrode theory equations are derived. This framework includes equations to model mass and charge conservation in the electrolyte, mass conservation in the solid intercalation particles, and electron conservation in the conducting matrix. These mass and charge conservation equations are coupled to self-consistent models of the charge transfer reaction and the Nernst potential. The Nernst potential is formulated using the same thermodynamic expressions used in the mass conservation equation for the intercalation particles. The charge transfer reaction is also formulated using the same thermodynamic expressions, and is presented in a form similar to the Butler-Volmer equation, which determines the reaction rate based on the local overpotential. This self-consistent set of equations allows both homogeneous and phase separating intercalation materials

to be modeled.

After the derivation of the set of equations, the numerical methods used to solve the equations in this work are briefly presented, including the finite volume method and solution methods for differential algebraic equations. Then, example simulations at constant current are provided for homogeneous and phase separating materials to demonstrate the effect of changing the solid diffusivity and discharge rate on the cell voltage. Other effects, such as coherency strain, are also presented to demonstrate their effect on the behavior of particles inside the cell (e.g. suppression of phase separation). After the example simulations, specific simulations for two phase separating materials are presented and compared to experiment. These simulations include slow discharge of a lithium iron phosphate cell at constant current, and electrolyte-limited discharge of a graphite cell at constant potential. These two simulations are shown to agree very well with experimental data. In the last part of this thesis, the most recent work is presented, which is based on modeling lithium iron phosphate particles including coherency strain and surface wetting. These results are qualitatively compared with experimental data. Finally, future work in this area is considered, along with a summary of the thesis.

Thesis Supervisor: Martin Z. Bazant
Title: Professor

Acknowledgments

When I first joined the Bazant Group, I had very little experience with simulation and modeling, so needless to say I was a little worried about running simulations with complicated phase behavior. The field was very interesting to me, though, and I was motivated to learn more about phase field modeling, simulation, and numerical methods. I was also fortunate enough to have lots of support and guidance.

I'd first like to thank my fiancée, Danielle, and my parents for their love and support over the past five years. Whether I was worried about presentations, papers, or exams, they were always able to keep me grounded, and their support has helped me through my time here at MIT. I wouldn't have been able to do it without them.

I'd also like to thank my advisor, Martin, for his guidance and giving me direction for my research. A large part of this thesis stems from concepts I learned in his course, 10.626, which I was fortunate enough to TA as well. Despite his schedule becoming increasingly busy over the past few years, he has always been able to make time to discuss my research, whether after class or via email late at night, and this was instrumental in my progress.

There are also a large number of post-docs, group members, and visitors I would like to thank for their guidance. Dan Cogswell, a recent post-doc in the group, helped me immensely with phase field modeling and numerics. His single particle simulations have also had a large impact on my work, as can be seen throughout my thesis. Damian Burch, who was graduating when I joined the group, helped me with my first simulations. Peng Bai, a current post-doc in the group, has helped me to better understand battery dynamics and experimental methods. I'd also like to thank Michael Hess, a visitor to the group, whose discussions on graphite and lithium iron phosphate helped me greatly. Moses Ender, who recently visited the group, helped me with porous media modeling as well as improving my understanding of how batteries are made. Finally, I'd like to thank Ray Smith and Edwin Sze Lun Khoo, current group members who helped me proofread this thesis and whose discussions have helped improve my equations and code.

Finally, this work would not have been possible without financial sponsors. I'd like to thank NSF and MITEI for funding this research and giving me the opportunity to research such a relevant and exciting field in energy engineering.

Contents

List of Figures

List of Tables

Chapter 1

Introduction

Modeling is a key component of any design process. An accurate model allows one to interpret experimental data, identify rate limiting steps and predict system behavior, while providing a deeper understanding of the underlying physical processes. In systems engineering, empirical models with fitted parameters are often used for design and control, but it is preferable, whenever possible, to employ models based on microscopic physical or geometrical parameters, which can be more easily interpreted and optimized.

1.1 Motivation

In the case of electrochemical energy storage devices, such as batteries, fuel cells, and supercapacitors, the systems approach is illustrated by equivalent circuit models, which are widely used in conjunction with impedance spectroscopy to fit and predict cell performance and degradation. This approach is limited, however, by the difficulty in unambiguously interpreting fitted circuit elements and in making predictions for the nonlinear response to large operating currents. There is growing interest, therefore, in developing physics-based porous electrode models and applying them for battery optimization and control [111]. Quantum mechanical computational methods have demonstrated the possibility of predicting bulk material properties, such as open circuit potential and solid diffusivity, from first principles [40], but coarse-

grained continuum models are needed to describe the many length and time scales of interfacial reactions and multiphase, multicomponent transport phenomena.

Mathematical models could play a crucial role in guiding the development of new intercalation materials, electrode microstructures, and battery architectures, in order to meet the competing demands in power density and energy density for different envisioned applications, such as electric vehicles or renewable (e.g. solar, wind) energy storage. Porous electrode theory, pioneered by J. Newman and collaborators, provides the standard modeling framework for battery simulations today [98]. As reviewed in the next section, this approach has been developed for over half a century and applied successfully to many battery systems. The treatment of the active material, however, remains rather simple, and numerous parameters are often needed to fit experimental data.

In porous electrode theory for Li-ion batteries, transport is modeled via volume averaged conservation equations [50]. The solid active particles are modeled as spheres, where intercalated lithium undergoes isotropic linear diffusion [51, 52]. For phase separating materials, such as Li_xFePO_4 (LFP), each particle is assumed to have a spherical phase boundary that moves as a "shrinking core", as one phase displaces the other [123, 46, 132]. In these models, the local Nernst equilibrium potential is fitted to the global open circuit voltage of the cell, but this neglects non-uniform composition, which makes the voltage plateau an emergent property of the porous electrode [54, 53, 8, 45]. For thermodynamic consistency, all of these phenomena should derive from common thermodynamic principles and cannot be independently fitted to experimental data. The open circuit voltage reflects the activity of intercalated ions, which in turn affects ion transport in the solid phase and Faradaic reactions involving ions in the electrolyte phase [12, 13].

In this thesis, porous electrode theory is extended to non-ideal active materials, including those capable of phase transformations. The starting point is a general phase-field theory of ion intercalation kinetics developed by the Bazant group over the past five years [13, 120, 33, 16, 32, 8], which has recently led to a quantitative understanding of phase separation dynamics in LFP nanoparticles [45, 44]. The ionic

fluxes in all phases are related to electrochemical potential gradients, consistent with non-equilibrium thermodynamics [62, 10]. This approach has been used extensively in recent years to model transport in electrochemical systems [74, 88, 87, 90, 89, 21, 79, 80, 102, 17] and nonlinear electrokinetic phenomena [16, 15, 20, 126]. For thermodynamic consistency, we also relate the Faradaic reaction rate to electrochemical potential differences between the oxidized, reduced, and transition states, leading to a generalized Butler-Volmer equation [13, 8, 45] suitable for phase-separating materials. These elements are integrated in a general porous electrode theory, where the active material can be described by a Cahn-Hilliard phase-field model [10, 97], as in nanoscale simulations of Li-ion battery materials [66, 61, 120, 33, 32, 128, 76, 8, 45]. This allows us to describe the non-equilibrium thermodynamics of porous battery electrodes in terms of well established physical principles for ion intercalation in nanoparticles.

1.2 Brief History of Porous Electrode Theory

We begin by reviewing volume-averaged porous electrode theory, which has been the standard approach in battery modeling for the past 50 years. The earliest papers dealing with porous electrode theory were published in the late 1950's and early 1960's, by Ksenzhek and Stender [83, 84, 85] and Euler and Nonnenmacher [57]. This work treated current density distributions in porous electrodes, which were characterized by volume averaged properties, such as porosity, average surface area per volume, and conductivity.

A few years later, Newman and Tobias expanded the analysis to account for the effects of concentration variations on kinetics with concentration independent electrolyte properties. [100] This paper also introduced the well known equation for mass conservation inside a porous electrode undergoing reactions. Around the same time, de Levie published his work modeling diffusion inside pores, capacitance effects, and combined effects of double layer capacitance, diffusion, and kinetics. [47, 48] These models included linear capacitance effects for the double layer and utilized

equivalent circuit models for the porous electrode.

Another notable paper is by Ksenzhek, which incorporated concentrated solution theory in the transport equations inside a porous electrode, and referred to gradients in electrochemical potential as the driving force for transport. [82] (for more on force and flux coupling, refer to [10]) Ksenzhek's paper introduced many of the same concepts used in this paper to treat transport processes in the electrode. Much of the earlier work on modeling porous electrodes relied on deriving the volume averaged governing equations as well as some analytical results for small overpotential (i.e. linearized) or high overpotential (i.e. Tafel) regime kinetics. [72] Other notable papers include modeling transport effects in steady state operation [63] and transient behavior of a porous electrode subjected to galvanostatic discharge with sinusoidal perturbations. [112]

Many of the volume averaged principles have underlying assumptions regarding properties of the cell that can be critical to performance. The validity of these assumptions was reviewed by Grens. [71] It was found that the assumption of constant conductivity can be used over a wide range of operating conditions. The assumption of constant electrolyte concentration, which was used to simplify systems in early papers, is only valid over a narrow range of operating conditions, as is expected.

In 1975, Newman and Tiedemann published a review of porous electrode theory. [99] This paper summarized mass and charge conservation equations and kinetic equations for batteries and other types of electrochemical systems. A few years later, Atlung *et al.* investigated the dynamics of solid solution (i.e. intercalation) electrodes for different time scales with respect to the limiting current. [6] Pollard and Newman investigated the transient behavior of porous electrodes at high exchange current densities (i.e. small overpotential). [107] These two papers appear to be some of the earliest studies of the time dependence of porous electrode systems. Up to this point, the literature was predominantly based on linearized Butler-Volmer and exponential Tafel kinetics, due to limited computational power.

As computers and numerical methods advanced, so did simulations of porous electrodes. West *et al.* demonstrated the use of numerical methods to simulate

discharge of a porous TiS_2 electrode (without the separator), and how the main limiting factor is the depletion of the electrolyte. [138] This is one of the earliest demonstrations of solving the porous electrode equations using numerical methods. About ten years later, Doyle, Fuller and Newman modeled a separator and porous electrode under constant current discharge. [51] This paper was one of the first to model the reaction rate with the Butler-Volmer equation, instead of linearized kinetics or a Tafel equation. The next year, Fuller, Doyle and Newman published a similar model of a dual lithium-ion insertion cell (graphite anode and manganese oxide cathode) [59]. Doyle et al. then published a comparison of model predictions with experimental data for the full lithium-ion battery (anode and cathode) [52] These papers are of great importance in the field, as they developed the first complete simulations of lithium-ion batteries and solidified the role of porous electrode theory in modeling these systems. The same theoretical framework has been applied to many other types of cells, such as lithium-sulfur [86] and LFP [123, 46] batteries. This framework has also been applied to lithium polymer batteries, for which Arora *et al.* have demonstrated good agreement with experimental data for high-rate discharge. [3]

Battery models invariably assume electroneutrality, but diffuse charge in porous electrodes has received increasing attention over the past decade, driven by applications in energy storage and desalination. The effects of double-layer capacitance in a porous electrode were originally considered using only linearized low-voltage models [75, 134], which are equivalent to transmission line circuits [47, 48, 55]. Recently, the full nonlinear dynamics of capacitive charging and salt depletion have been analyzed and simulated in both flat [18, 102] and porous [22] electrodes. The combined effects of electrostatic capacitance and pseudo-capacitance due to Faradaic reactions have also been incorporated in porous electrode theory [23, 24], using Frumkin-Butler-Volmer kinetics [19, 14, 29, 81, 73]. These models have been successfully used to predict the nonlinear dynamics of capacitive desalination by porous carbon electrodes [25, 109].

Computational and experimental advances have also been made to study porous electrodes at the microstructural level and thus test the formal volume-averaging,

which underlies macroscopic continuum models. Garcia et al. performed finite-element simulations of ion transport in typical porous microstructures for Li-ion batteries [61], and Garcia and Chang simulated hypothetical inter-penetrating 3D battery architectures at the particle level [60]. Recently, Smith, Garcia and Horn analyzed the effects of microstructure on battery performance for various sizes and shapes of particles in a $Li_{1-x}C_6/Li_xCoO_2$ cell [122]. The study used 3D image reconstruction of a real battery microstructure by focused ion beam milling, which has led to detailed studies of microstructural effects in porous electrodes [133, 131, 78]. In this paper, we will discuss mathematical bounds on effective diffusivities in porous media, which could be compared to results for actual battery microstructures. Recently, it has also become possible to observe lithium ion transport at the scale in individual particles in porous Li-ion battery electrodes [9, 137], which could be invaluable in testing the dynamical predictions of new mathematical models.

1.3 Phase Separating Electrodes

1.3.1 Lithium Iron Phosphate

The discovery of LFP as a cathode material by the Goodenough group in 1997 has had a large and unexpected impact on the battery field, which provides the motivation for our work. LFP was first thought to be a low-power material, and it demonstrated poor capacity at room temperature. [104] The capacity has since been improved via conductive coatings and the formation of nanoparticles. [113, 69], and the rate capability has been improved in similar ways [68, 92]. With high carbon loading to circumvent electronic conductivity limitations, LFP nanoparticles can now be discharged in 10 seconds [76]. Off-stoichiometric phosphate glass coatings contribute to this high rate, not only in LFP, but also in $LiCoO_2$ [127].

It has been known since its discovery that LFP is a phase separating material, as evidenced by a flat voltage plateau in the open circuit voltage [104, 129]. There are a wide variety of battery materials with multiple stable phases at different states of

charge [70], but Li_xFePO_4 has a particularly strong tendency for phase separation, with a miscibility gap (voltage plateau) spanning across most of the range from $x = 0$ to $x = 1$ at room temperature. Padhi et al. first depicted phase separation inside LFP particles schematically as a "shrinking core" of one phase being replaced by an outer shell of the other phase during charge/discharge cycles [104]. Srinivasan and Newman encoded this concept in a porous electrode theory of the LFP cathode with spherical active particles, containing spherical shrinking cores. [123] Recently, Dargaville and Farrell have expanded this approach to predict active material utilization in LFP electrodes. [46] Thorat *et al.* have also used the model to gain insight into rate-limiting mechanisms inside LFP cathodes. [132]

To date, the shrinking-core porous electrode model is the only model to successfully fit the galvanostatic discharge of an LFP electrode, but the results are not fully satisfactory. Besides neglecting the microscopic physics of phase separation, the model relies on fitting a concentration-dependent solid diffusivity, whose inferred values are orders of magnitude smaller than *ab initio* simulations [96, 92] or impedance measurements [105]. More consistent values of the solid diffusivity have since been obtained by different models attempting to account for anisotropic phase separation with elastic coherency strain. [139] Most troubling for the shrinking core picture, however, is the direct observation of phase boundaries with very different orientations. In 2006, Chen, Song, and Richardson published images showing the orientation of the phase interface aligned with iron phosphate planes and reaching the active facet of the particle. [41] This observation was supported by experiments of Delmas *et al.*, who suggested a "domino-cascade model" for the intercalation process inside LFP [49]. With further experimental evidence for anisotropic phase morphologies [103, 137], it has become clear that a new approach is needed to capture the non-equilibrium thermodynamics of this material.

1.3.2 Phase-Field Models

Phase-field models are widely used to describe phase transformations and microstructural evolution in materials science [10, 42], but they are relatively new to electro-

chemistry. In 2004, Guyer, Boettinger, Warren and McFadden [64, 65] first modeled the sharp electrode/electrolyte interface with a continuous phase field varying between stable values 0 and 1, representing the liquid electrolyte and solid metal phases. As in phase-field models of dendritic solidification [77, 27, 26, 28], they used a simple quartic function to model a double-welled homogeneous free energy. They described the kinetics of electrodeposition [65] (converting ions in the electrolyte to solid metal) by Allen-Cahn-type kinetics [2, 42], linear in the thermodynamic driving force, but did not make connections with the Butler-Volmer equation. Several groups have used this approach to model dendritic electrodeposition and related processes [5, 118, 108]. Also in 2004, Han, Van der Ven and Ceder [66] first applied the Cahn-Hilliard equation[34, 35, 39, 36, 10, 42] to the diffusion of intercalated lithium ions in LFP, albeit without modeling reaction kinetics.

Building on these advances, Bazant developed a general theory of charge-transfer and Faradaic reaction kinetics in concentrated solutions and solids based on non-equilibrium thermodynamics [13, 11, 12], suitable for use with phase-field models. The exponential Tafel dependence of the current on the overpotential, defined in terms of the variational chemical potentials, was first reported in 2007 by Singh, Ceder and Bazant [120, 119], but with spurious pre-factor, corrected by Burch [31, 32]. The model was used to predict "intercalation waves" in small, reaction-limited LFP nanoparticles in 1D [120], 2D [33], and 3D [128], thus providing a mathematical description of the domino cascade phenomenon [49]. The complete electrochemical phase-field theory, combining the Cahn-Hilliard with Butler-Volmer kinetics and the cell voltage, appeared in 2009 lectures notes [11, 12] and was applied to LFP nanoparticles [8, 45].

The new theory has led to a quantitative understanding of intercalation dynamics in single nanoparticles of LFP. Bai, Cogswell and Bazant [8] generalized the Butler-Volmer equation using variational chemical potentials (as derived in the supporting information) and used it to develop a mathematical theory of the suppression of phase separation in LFP nanoparticles with increasing current. This phenomenon, which helps to explain the remarkable performance of nano-LFP, was also suggested by Malik

and Ceder based on bulk free energy calculations [93], but the theory shows that it is entirely controlled by Faradaic reactions at the particle surface [8, 45]. Cogswell and Bazant [45] have shown that including elastic coherency strain in the model leads to a quantitative theory of phase morphology and lithium solubility. Experimental data for different particles sizes and temperatures can be fitted with only two parameters (the gradient penalty and regular solution parameter, defined below).

The goal of the present work is to combine the phase-field theory of ion intercalation in nanoparticles with classical porous electrode theory to arrive at a general mathematical framework for non-equilibrium thermodynamics of porous electrodes. Our work was first presented at the Fall Meeting of the Materials Research Society in 2010 and again at the Electrochemical Society Meetings in Montreal and Boston in 2011. Around the same time, Lai and Ciucci were thinking along similar lines [87, 89] and published an important reformulation of Newman's porous electrode theory based non-equilibrium thermodynamics [90], but they did not make any connections with phase-field models or phase transformations at the macroscopic electrode scale. (Their treatment of reactions also differs from Bazant's theory of generalized Butler-Volmer or Marcus kinetics [13, 12, 11].)

In this thesis, a variational thermodynamic description of electrolyte transport, electron transport, electrochemical kinetics, and phase separation is developed and applied to Li-ion batteries in what appears to be the first mathematical theory and computer simulations of *macroscopic phase transformations in porous electrodes*. Simulations of discharge into a cathode consisting of multiple phase-separating particles interacting via an electrolyte reservoir at constant chemical potential were reported by Burch [31], who observed "mosaic instabilities", where particles transform one-by-one at low current. This phenomenon was elegantly described by Dreyer et al. in terms of a (theoretical and experimental) balloon model, which helps to explain the noisy voltage plateau and zero-current voltage gap in slow charge/discharge cycles of porous LFP electrodes [54, 53]. These studies, however, did not account for electrolyte transport and associated macroscopic gradients in porous electrodes undergoing phase transformations, which are the subject of this work. To do this, we must

reformulate Faradaic reaction kinetics for concentrated solutions, consistent with the Cahn-Hilliard equation for ion intercalation and Newman's porous electrode theory for the electrolyte.

This thesis also presents fitting of the voltage gap data data presented by Dreyer *et al.*. [54] A pseudocapacitor model with a voltage gap fit to the work of Cogswell and Bazant [44] is used to fit a particle size distribution and contact resistance and demonstrate why different experiments observe different values of the voltage gap, and why the observed voltage gap does not match the voltage gap predicted by thermodynamics alone.

Additionally, a model for the free energy of graphite is presented and fit to data for the case of electrolyte transport limited potentiostatic discharge. This new graphite free energy model captures three phase behavior of lithiated graphite (i.e. empty, half full, and full states) by using two representative graphite layers along with an interaction energy and what can be thought of as a strain energy. Although graphite actually has more than three phases [101], for the purpose of this simulation (i.e. matching to experimental data) three phases are sufficient. The data the simulations are fit to determines the concentration of lithium in graphite using the color change associated with lithiation, and only three colors are presented, corresponding to the three phases (i.e. empty, half, and full).

Building on the recent work of Cogswell and Bazant [44], surface wetted $LiFePO_4$ particles inside a porous electrode with approximated coherency strain are also presented in this thesis. These simulations are compared qualitatively to experimental data from Li and Chueh. [43] Finally, a simulation including electron conduction with the aforementioned surface wetted $LiFePO_4$ particles and coherency strain is compared to experimental data.

1.4 Thesis Outline

This thesis will begin with a brief overview of the thermodynamics used as well as a derivation of concentrated solution theory that will be used throughout the rest of

the chapters. This overview is followed by the derivation of the full set of modified porous electrode theory equations, as well as the non-dimensionalization that is used in later simulations. Additional examples demonstrating the use of the Cahn-Hilliard free energy functional are also included.

After the derivation of the full set of equations, some numerical methods are briefly discussed. The focus of this thesis work is on the model development itself. The chapter on numerics is not intended to be a full review of all methods available, but to present some potential methods that can be used as well as how the equations were formulated and discretized for the simulations in this thesis work. After the chapter on numerics, some example simulations from the first publication as a result of this work are presented. The purpose of these simulations is to demonstrate the effect of changing parameters in the model, namely the discharge rate (i.e. the current) and solid diffusivity.

After the general simulation results, more specific results along with a comparison to data will be presented. The first data set analyzed is that of Dreyer *et al.*. [53] Using a "pseudocapacitor" model, which assumes all solid particles are homogeneous, a particle size distribution and contact resistance are fit to the voltage gap. The size distribution is based on simulations from Cogswell and Bazant. [44] Then, a new graphite free energy model is used to fit the experimental data of Harris *et al.* [67] using an electrolyte diffusion limited cell.

The second to last chapters of this thesis represents the most recent work. It includes simulations using the surface wetted $LiFePO_4$ particles with coherency strain from Cogswell and Bazant [44] inside a porous electrode. The results are qualitatively compared to recent experimental data from Li and Chueh (similar to previous work by Chueh *et al.* [43]). The final section considers the surface wetted particles with bulk electronic conduction effects and compares this to data from Ender. [56] The final chapter is a summary of the work presented in this thesis as well as future work.

Chapter 2

Non-equilibrium Thermodynamics

Classical thermodynamics deals with equilibrium states. However, time evolution is a non-equilibrium process. Non-equilibrium thermodynamics allows the evolution of energy states to be modeled using thermodynamic models. The underlying assumption is that the system proceeds through small perturbations from equilibrium, such that changes can be linearized. More specifically, this requires that processes are reversible, which implies that entropy is conserved.

2.1 Chemical Potential

Chemical potential is the change in energy associated with the change in mass of a system. It is an additional term in the energy equations which accounts for the inherent energy particles bring as they are added or removed form the system. The chemical potential has a different definition based on the state variables of the system. For the four different types of energy (Gibbs free energy, Helmholtz free energy,

enthalpy, and internal energy), the chemical potential is defined as

$$\mu_i = \left(\frac{\partial U}{\partial n_i}\right)\Big|_{S,V,n_i \neq n_j} \tag{2.1}$$

$$= \left(\frac{\partial H}{\partial n_i}\right)\Big|_{S,P,n_i \neq n_j} \tag{2.2}$$

$$= \left(\frac{\partial A}{\partial n_i}\right)\Big|_{T,V,n_i \neq n_j} \tag{2.3}$$

$$= \left(\frac{\partial G}{\partial n_i}\right)\Big|_{T,P,n_i \neq n_j}. \tag{2.4}$$

These relations can be obtained via partial Legendre transforms of the Gibbs-Duhem equation. (for more on thermodynamics, the reader is directed to [110] and [130]) Regardless of the state variables, the chemical potential relates a system's energy change to the change in mass (or number) of a specific species while keeping the number of other species in the system constant.

This definition implies that at equilibrium, the energy change by moving mass from one state to another must be zero, which means that at equilibrium, the chemical potential of two states are identical. This definition is upheld in the general reaction rate equation. To simplify the notation and indicate a system's deviation from a standard state (which is often picked to exhibit ideal behavior), we introduce the concept of chemical activity. The chemical activity is defined as

$$\mu_i = k_B T \ln(a_i) + \mu_i^o \tag{2.5}$$

The activity can be further decomposed via

$$a_i = c_i \gamma_i \tag{2.6}$$

to denote concentration effects as well as additional non-ideal effects, which are contained in the activity coefficient, γ_i. The chemical potential is defined in reference to some well defined standard state. The reference chemical potential is μ_i^o, which is defined to have unit activity (i.e a_i^o=1). We can insert the activity from Equation

(2.6) into Equation (2.5) to obtain

$$\mu_i = k_B T \ln(\tilde{c}_i) + \mu_i^{EX}, \tag{2.7}$$

where concentration $\tilde{c}_i = c_i/c_i^o$ and μ_i^{EX} is the excess chemical potential given by

$$\mu_i^{EX} = k_B T \ln(\gamma_i) + \mu_i^o. \tag{2.8}$$

From this, it can be seen that the activity coefficient is

$$\gamma_i = \exp\left(\frac{\mu_i^{EX} - \mu_i^o}{k_B T}\right). \tag{2.9}$$

In the dilute limit μ_i^{EX} approaches the reference chemical potential, μ_i^o, and the activity coefficient approaches unity.

These definitions allow us to define the change in energy of a particle between two states, which is necessary if one wishes to define how systems proceed out of equilibrium. Furthermore, it allows us to define reference states for a given system, and define the non-ideality using the activity coefficient. If non-ideal behavior is neglected, the system can be treated as an ideal system using the dimensionless concentration. It is important to remember that in the dilute limit, the chemical potential scales with the natural log of the dimensionless concentration. Furthermore, the activity of the reference state is unity.

2.2 General Theory of Reactions

The derivation of concentrated solution theory and the following transport and reaction equations used in this research begins with a general theory of reactions. This equation is the starting point for all subsequent derivations. Consider two states, 1 and 2. As a particle proceeds from state 1 to state 2, it travels through some transition state, as shown in Figure 2-1. Reactions are considered rare events and the reaction barrier is assumed to be much larger than the thermal energy, $k_B T$. The

transition state is considered to be short lived, such that any concentration effects can be factored out into a constant. Also, particles that reach the transition state are assumed to proceed through the reaction with unity probability.

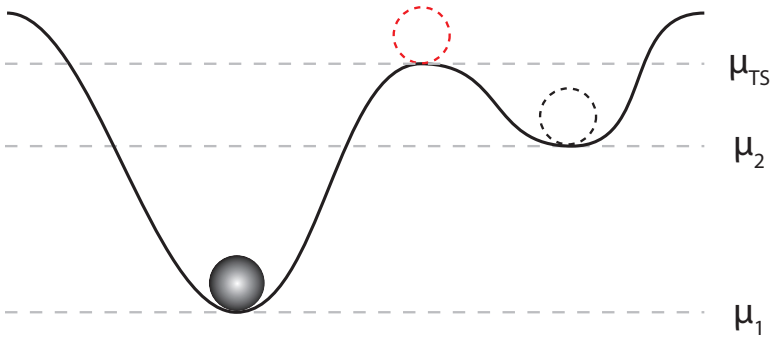

Figure 2-1: **Typical reaction energy landscape**. The set of atoms involved in the reaction travels through a transition state as it passes from one state to the other in a landscape of total excess chemical potential as a function of the atomic coordinates.

A general reaction rate for particles proceeding between two states, denoted 1 and 2, can be written as

$$R = k_o \left[\exp\left(-\frac{\left(\mu_{TS}^{EX} - \mu_1\right)}{k_B T} \right) - \exp\left(-\frac{\left(\mu_{TS}^{EX} - \mu_2\right)}{k_B T} \right) \right], \tag{2.10}$$

where R is the reaction rate in units of inverse time. The rate constant k_o is the attempt frequency, and μ_1, μ_2 are the chemical potentials of states 1 and 2. The energy barrier for the forward and reverse reaction rates are $\mu_{TS}^{EX} - \mu_1$ and $\mu_{TS}^{EX} - \mu_2$, respectively. The transition state is assumed to be short lived, and the concentration has been factored out into the rate constant. This general reaction rate satisfies the de Donder relation, and the reaction rate is zero at equilibrium, when the chemical potential of states 1 and 2 are equal.

This general reaction rate can be used to derive equations for concentrated solution theory (CST) and relate the diffusivity to activity coefficients of the species and the transition state. This fundamental equation will be the starting point for the derivations presented here.

2.3 Concentrated Solution Theory

Concentrated solution theory is the foundation for the equations used in this thesis. Solid materials, especially phase separating materials, demonstrate very complicated behavior which is a function of the local concentration. Prior to the derivation of the CST equation, we will first establish definitions of chemical potential and then derive an expression for the diffusivity. Finally, we derive the CST equation and combine with the derived diffusivity to obtain a transport equation which can address a wide variety of materials, including homogeneous and higher order phase transitions.

2.3.1 Diffusivity

Using the definition of the chemical potential presented here, along with the general reaction rate, we will first derive an expression for the diffusivity of a species diffusing through a medium. During diffusion, particles undergo a random walk through a medium in an excess chemical energy landscape, as shown in Figure 2-2. The random walk diffusivity can be expressed as

$$D = \frac{(\Delta x)^2}{2\tau}, \tag{2.11}$$

where Δx is the average step length (i.e. the length of one diffusive "hop") and τ is the mean time between transitions. The factor of two in the denominator represents the probability that a particle will go in the positive direction. The time between transitions can be thought of as the inverse rate. The rate of transitions can be expressed as

$$R_t = k_o \exp\left(-\frac{\left(\mu_{TS}^{EX} - \mu^{EX}\right)}{k_B T}\right) \tag{2.12}$$

where k_o is the barrier-less rate, and the exponential term is the Boltzmann probability that a particle has enough energy to hop to an adjacent site.

It is important to note that the excess chemical potential is what influences the diffusivity. The excess chemical potential determines the drift, which skews the rate away from the ideal rate. Without the excess chemical potential, all diffusivities

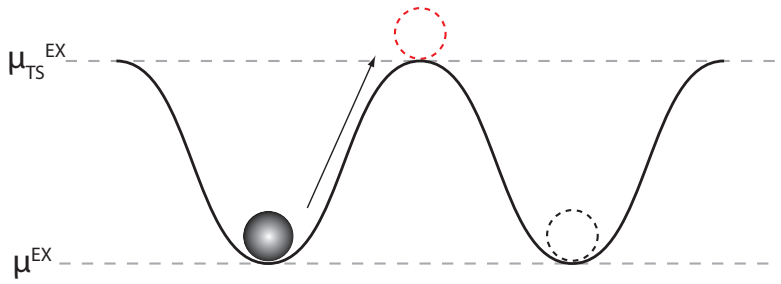

Figure 2-2: **Typical diffusion energy landscape**. The same principles for reactions can also be applied to solid diffusion, where the diffusing molecule explores a landscape of excess chemical potential, hopping by thermal activation between nearly equivalent local minima.

would be simply dependent on temperature and entropic effects. Therefore, inside a specific medium, the excess chemical potential is what is important in determining the diffusivity. The mean time between transitions is the inverse rate,

$$\tau = \tau_o \exp\left(\frac{\mu_{TS}^{EX} - \mu^{EX}}{k_B T}\right), \tag{2.13}$$

where $\tau_o = 1/k_o$ is the time between barrier-less transitions, or the inverse attempt frequency. Inserting this expression into Equation (2.11), we obtain the diffusivity,

$$D = \frac{(\Delta x)^2}{2\tau_o}\frac{\gamma}{\gamma_{TS}}, \tag{2.14}$$

where γ and γ_{TS} are the activity coefficients of the particle and the transition state, respectively. To model the diffusivity, an appropriate thermodynamic model for the solid is required. Figure 2-3 demonstrates the lattice gas model for diffusion, which is one model that can be used. The lattice gas model ignores pairwise interactions (i.e. enthalpic energy) and treats purely entropic effects on a grid. Next, the equation for concentrated solution theory will be derived.

2.3.2 Derivation

Now that we have a proper definition for the chemical potential and an expression for the diffusivity, we begin with the general reaction rate presented in Equation (2.10).

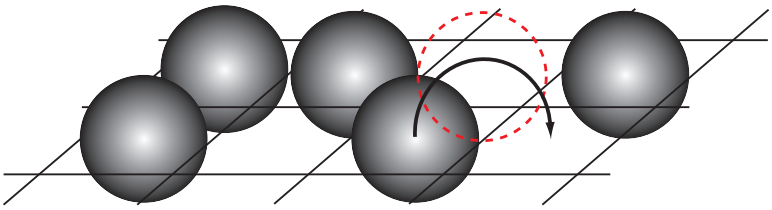

Figure 2-3: **Lattice gas model for diffusion**. The atoms are assigned a constant excluded volume by occupying sites on a grid. Atoms can only jump to an open space, and the transition state (red dashed circle) requires two empty spaces.

We assume that our particle is close to equilibrium, which allows us to linearize the equation. Furthermore, we assume transition state theory can be applied, and that all particles that reach the transition state proceed with unity probability.

First, we postulate the chemical potential of states 1 and 2 using a Taylor expansion near x,

$$\mu_1 = \mu(x) - \frac{\Delta x}{2}\frac{\partial \mu}{\partial x}, \tag{2.15}$$

$$\mu_2 = \mu(x) + \frac{\Delta x}{2}\frac{\partial \mu}{\partial x}, \tag{2.16}$$

where x is a spatial direction. Figure 2-4 shows the atom diffusing through a solid. These chemical potential expressions are inserted into the general reaction rate equation. We can replace the exponential terms with a hyperbolic sine function. Simplifying, we obtain

$$R = -\frac{2R_o a(x)}{\gamma_{TS}} \sinh\left(\frac{\Delta x}{2k_B T}\frac{\partial \mu}{\partial x}\right), \tag{2.17}$$

where $R_o = 1/2\tau_o$ is the barrier-less reaction rate. The factor of two comes from the probability of the reaction proceeding in the positive x-direction. Before proceeding, we need to relate the reaction rate to the species flux, $\mathbf{F}$. The flux can be expressed as

$$\mathbf{F}_x = \frac{R}{A}\mathbf{e}_x, \tag{2.18}$$

where $\mathbf{e}_x$ is a vector indicating the direction (in this case, the x-direction, as indicated in the flux subscript).

Since we are close to equilibrium, the spatial derivative of the chemical potential

is small and we can linearize the hyperbolic sine term about zero. The activity, $a(x)$, can be expressed as $c(x)V\gamma$. Simplifying and inserting our equation into the flux definition, we obtain

$$\mathbf{F}_x = -\frac{1}{\tau_o A}\frac{\Delta x}{2k_B T}\frac{c(x)V\gamma}{\gamma_{TS}}. \tag{2.19}$$

The volume can be expressed as $V = A\Delta x$. Substituting and moving terms around we obtain

$$\mathbf{F}_x = -\frac{(\Delta x)^2}{2\tau_o}\left(\frac{\gamma}{\gamma_{TS}}\right)\frac{c(x)}{k_B T}\frac{\partial \mu}{\partial x}. \tag{2.20}$$

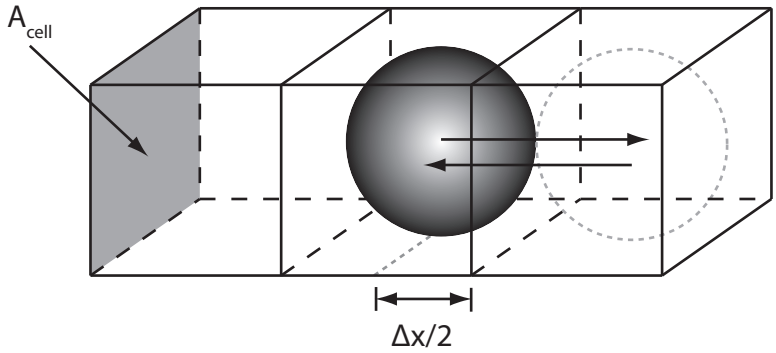

Figure 2-4: **Diffusion through a solid**. The flux is given by the reaction rate across the area of the cell, A_{cell}. In this lattice model, atoms move between available sites.

From this form, we see the previously derived diffusivity falls out of our flux equation, $D = D_o\gamma/\gamma_{TS}$, where $D_o = (\Delta x)^2/2\tau_o$. Using the Einstein relation, which states $D = Mk_BT$, where M is the species mobility, and expanding the equation to three dimensions, we can substitute the mobility back into Equation (2.20) to obtain the classical concentrated solution theory equation for the flux

$$\mathbf{F} = -Mc\nabla\mu. \tag{2.21}$$

This equation is the starting point for our porous electrode theory derivation. First, however, it's beneficial to connect this equation to Fick's Law and dilute solution theory. Inserting our definition of activity into Equation (2.21) and expressing the

flux in terms of the concentration gradient, we obtain

$$\mathbf{F} = -D\left(1 + \frac{\partial \ln \gamma}{\partial \ln c}\right)\nabla c. \tag{2.22}$$

This prefactor can be referred to as the chemical diffusivity, D_{chem}. This chemical diffusivity can be rewritten as

$$D_{chem} = \frac{D_o}{\gamma_{TS}}\frac{\partial a}{\partial c}. \tag{2.23}$$

From this definition, we see that in the dilute limit, our activity approaches c, γ_{TS} approaches one, and we recover the dilute limit diffusivity, D_o, thus recovering Fick's Law from Equation (2.22).

2.4 Conclusion

This chapter laid the framework for the thermodynamics and transport equations used throughout the rest of this thesis. We began with thermodynamic definitions of the chemical potential and a generic reaction rate equation. These were used to derive the diffusivity and concentrated solution theory equation. The concentrated solution theory equation will be used to derive the set of equations used in the Modified Porous Electrode Theory framework throughout this thesis.

This chapter is only intended to introduce the source of specific equations used throughout the rest of this thesis. It is not intended to act as a substitute for the underlying thermodynamics, and it assumes the reader has a basic understanding of entropy, enthalpy, and Gibbs free energy. For more on thermodynamics, we refer the reader to [110] and [130]. The next chapter will introduce equations and modeling effective properties of porous media, which are important in Modified Porous Electrode Theory.

Chapter 3

Porous Media

This chapter summarizes the methods used to model porous media using continuum equations. Different models for conductivity and diffusion in porous media are presented here. This chapter is adapted from Ferguson and Bazant. [58]

In batteries, the electrodes are typically composites consisting of active material (e.g. graphite in the anode, iron phosphate in the cathode), conducting material (e.g. carbon black), and binder. The electrolyte penetrates the pores of this solid matrix. This porous electrode is advantageous because it substantially increases the available active area of the electrode. However, this type of system, which can have variations in porosity (i.e. volume of electrolyte per volume of the electrode) and loading percent of active material throughout the volume, presents difficulty in modeling. To account for the variation in electrode properties, various volume averaging methods for the electrical conductivity and transport properties in the electrode are employed. In this chapter, we will present a brief overview of modeling the conductivity and transport of a heterogeneous material, consisting of two or more materials with different properties. [95, 135, 124, 114]

3.1 Electrical Conductivity of the Porous Media

To characterize the electrical conductivity of the porous media, we will consider rigorous mathematical bounds over all possible microstructures with the same volume

fractions of each component. First we consider a general anisotropic material as shown in Figure 3-1, in which case the conductivity bounds, due to Wiener, are obtained by simple microstructures with parallel stripes of the different materials [135]. The left image in Figure 3-1 represents the different materials as resistors in parallel, which produces the lowest possible resistance and the upper limit of the conductivity of the heterogeneous material. The right image represents the materials as resistors in series, which produces the highest possible resistance, or lower limit of the conductivity. These limits are referred to as the upper and lower Wiener bounds, respectively. Let Φ_i be the volume fraction of material i. For the upper Wiener bound, obtained by stripes parallel to the current, the effective conductivity is simply the arithmetic mean of the individual conductivities, weighted by their volume fractions,

$$\overline{\sigma}_{max} = \langle \sigma \rangle = \sum_i \Phi_i \sigma_i. \tag{3.1}$$

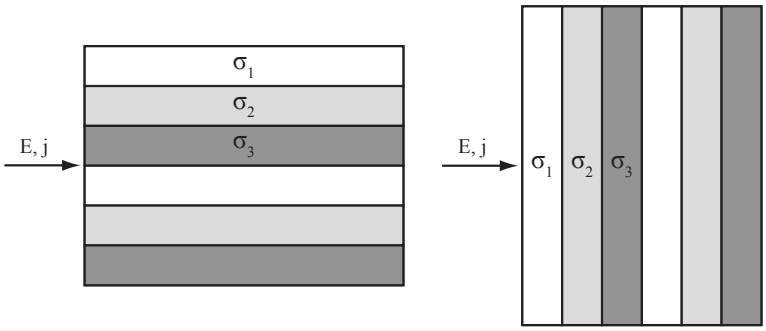

Figure 3-1: **Wiener bounds on the effective conductivity of a two-phase anisotropic material**. The left figure demonstrates the upper conductivity limit achieved by stripes aligned with the field, which act like resistors in parallel. The right figure demonstrates the lower bound with the materials arranged in transverse stripes to act like resistors in series.

The lower Wiener bound is obtained by stripes perpendicular to the current, and the effective conductivity is a weighted harmonic mean of the individual conductivities, as for resistors in parallel,

$$\overline{\sigma}_{min} = \langle \sigma^{-1} \rangle^{-1} = \frac{1}{\sum_i \frac{\Phi_i}{\sigma_i}}. \tag{3.2}$$

For a general anisotropic material, the effective conductivity, $\overline{\sigma}$, must lie within the Wiener bounds,

$$\langle \sigma^{-1} \rangle^{-1} \leq \overline{\sigma} \leq \langle \sigma \rangle. \tag{3.3}$$

There are tighter bounds on the possible effective conductivity of isotropic media, which have no preferred direction, due to Hashin and Shtrikman (HS) [135]. There are a number of microstructures which obtain the HS bounds, such as a space-filling set of concentric circles or spheres, whose radii are chosen to set the given volume fractions of each material. The case of two components is shown in Figure 3-2. The HS lower bound on conductivity is obtained by ordering the individual materials so as to place the highest conductivity at the core and the lowest conductivity in the outer shell, of each particle. For the HS upper bound, the ordering is reversed, and the lowest conductivity material is buried in the core of each particle, while the highest conductivity is in the outer shell, forming a percolating network across the system.

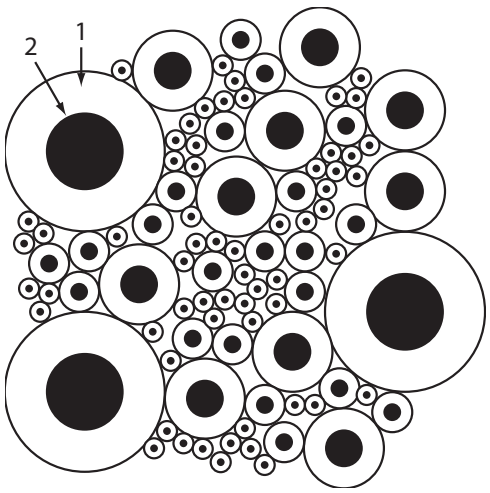

Figure 3-2: **Hashin-Shtrikman bounds on the effective conductivity of a two-phase isotropic material**. Isotropic random composite of space-filling coated spheres which attain the bounds. The white represents material with conductivity σ_1 and the black represents material with conductivity σ_2. Maximum conductivity is achieved when $\sigma_1 > \sigma_2$ and minimum conductivity is obtained when $\sigma_2 > \sigma_1$. The volume fractions Φ_1 and Φ_2 are the same.

For the case of two components, where $\sigma_1 > \sigma_2$, the HS conductivity bounds for

an isotropic two-component material in d dimensions are

$$\langle\sigma\rangle - \frac{(\sigma_1-\sigma_2)^2\,\Phi_1\Phi_2}{\langle\tilde{\sigma}\rangle+\sigma_2\,(d-1)} \leq \overline{\sigma} \leq \langle\sigma\rangle - \frac{(\sigma_1-\sigma_2)^2\,\Phi_1\Phi_2}{\langle\tilde{\sigma}\rangle+\sigma_1\,(d-1)}, \tag{3.4}$$

where

$$\langle\sigma\rangle = \Phi_1\sigma_1 + \Phi_2\sigma_2$$

and

$$\langle\tilde{\sigma}\rangle = \Phi_1\sigma_2 + \Phi_2\sigma_1.$$

The Wiener and Hashin-Shtrikman bounds above provide us with possible ranges for isotropic and anisotropic media with two components. Figure 3-3 gives the Wiener and Hashin-Shtrikman bounds for two materials, with conductivities of 1.0 and 0.1.

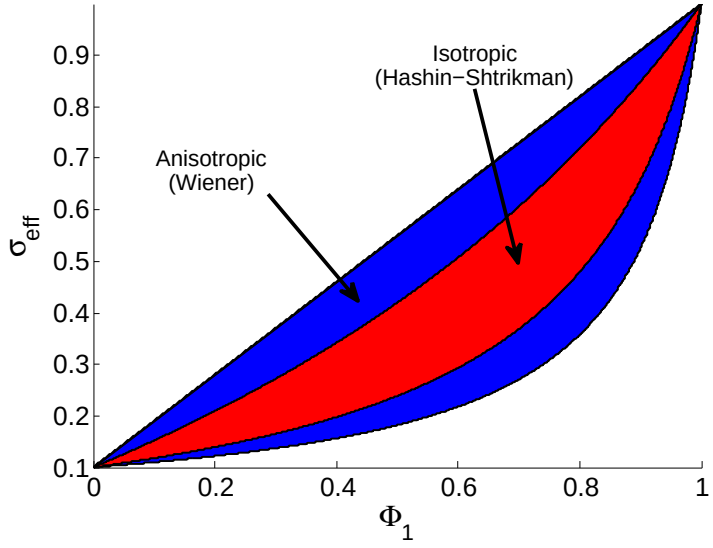

Figure 3-3: **Conductivity bounds for two-phase composites versus volume fraction**. The above figure shows the Wiener bounds (blue) for an anisotropic two component material and Hashin-Shtrikman bounds (red) for an isotropic two component material versus the volume fraction of material 1. The conductivities used to produce the figure are $\sigma_1 = 1$ and $\sigma_2 = 0.1$.

Next, we consider ion transport in porous media. Ion transport in porous media often consists of a solid phase, which has little to no ionic conductivity (i.e. slow or no diffusion) permeated by an electrolyte phase which has very high ionic conductivity (i.e. fast diffusion). In the next section, we will compare different models for effective

porous media properties.

3.2 Conduction in Porous Media

For the case of ion transport in porous media, there is an electrolyte phase, which has a non-zero diffusivity, and the solid phase, through which transport is very slow (essentially zero compared to the electrolyte diffusivity). Here, we consider the pores (electrolyte phase) and give the solid matrix a zero conductivity. The volume fraction of phase 1 (the pores), Φ_1, is the porosity:

$$\Phi_1 = \epsilon_p,\ \sigma_1 = \sigma_p.$$

The conductivity for all other phases is zero. This reduces the Wiener (anisotropic) and Hashin-Shtrikman (isotropic) lower bounds to zero. Figure (3-4) demonstrates a typical volume of a porous medium.

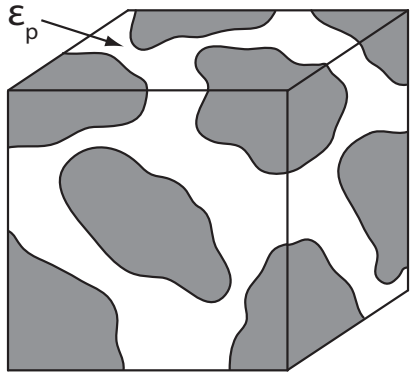

Figure 3-4: **Example of a porous volume**. This is an example of a typical porous volume. A mixture of solid particles is permeated by an electrolyte. The porosity, ϵ_p, is the volume of electrolyte as a fraction of the volume of the cube.

In porous electrode models for batteries [51, 59, 123], the Bruggeman formula [30] is used to relate the conductivity to the porosity,

$$\overline{\sigma}_B = \epsilon_p^{3/2}\sigma_p. \tag{3.5}$$

As shown in Figure 3-5, the Bruggeman formula is below the HS upper bound and corresponds to a highly conducting isotropic material, similar to a core-shell microstructure with solid cores and conducting shells (which is reasonable, since Bruggeman derived this expression for an isotropic medium). This makes sense for ionic conductivity in liquid-electrolyte-soaked porous media, but not for electronic conductivity based on networks of touching particles.

To understand the possible range of conductivity, we consider the rigorous bounds above. If we assume the media consists of two phases ($\Phi_2 = 1 - \epsilon_p$, $\sigma_2 = 0$), then the Wiener and Hashin-Shtrikman upper bounds can be simplified to

$$\overline{\sigma}_{max}^{Wiener} = \Phi_1 \sigma_1 = \epsilon_p \sigma_p, \tag{3.6}$$

and

$$\overline{\sigma}_{max}^{HS} = \sigma_p \epsilon_p \left(\frac{d-1}{d-\epsilon_p} \right). \tag{3.7}$$

where again d is the embedding dimension. The HS upper bound is attained by spherical core-shell particles with the conducting pore phase spanning the system via conducting shells on non-conducting solid cores, similar to electron-conducting coatings on active battery particles [7].

The lower bounds vanish because it is always possible that the conducting phase does not "percolate", or form a continuous path, across the system. Equivalently, the non-conducting matrix phase can percolate and block conduction. In such situations, however, the bounds are of little use, since they give no sense of the probability of finding percolating paths through a random microstructure. For ionic conduction through the electrolyte, which permeates the matrix, percolation may not be a major issue, but for electron conduction it is essential to maintain a network of touching conducting particles (such as carbon black in a typical battery electrode) [7].

In statistical physics, percolation models serve to quantify the conductivity of random media due to geometrical connectivity of particles [124, 114]. The simplest percolation models corresponds to randomly coloring a lattice of sites or bonds with a probability equal to the mean porosity and measuring the statistics of conduction

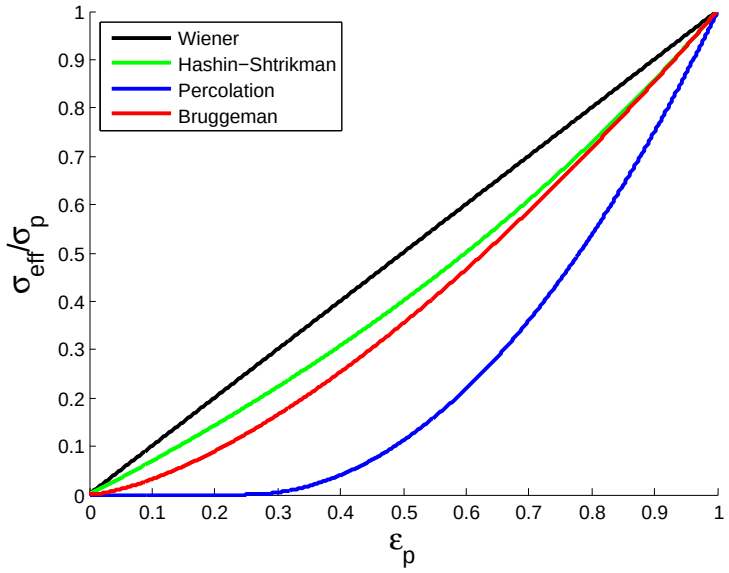

Figure 3-5: **Various models for effective conductivity in 3D**. This figure demonstrates the effective conductivity (scaled by the pore conductivity) using Wiener bounds, Hashin-Shtrikman bounds, a percolation model, and the Bruggeman formula. The percolation model uses a critical porosity of $\epsilon_c = 0.25$.

through clusters of connected sites or bonds. Continuum percolation models, such as the "swiss cheese model", correspond to randomly placing or removing overlapping particles of given shapes to form clusters. The striking general feature of such models is the existence of a critical porosity ϵ_c in the thermodynamic limit of an infinite system, below which the probability of a spanning infinite cluster is zero, and above which it is one. The critical point depends on the specific percolation model, and for lattice models it decreases with increasing coordination number (mean number of connected neighbors), as more paths across the system are opened. Just above the critical point, the effective conductivity scales as a power law,

$$\overline{\sigma}_{perc} \sim (\epsilon_p - \epsilon_c)^{t_p}\,, \tag{3.8}$$

where the exponent is believed to be universal for all percolation models in the same embedding dimensions and equal to $t_p = 2$ in three dimensions. A simple form to

capture this behavior is

$$\overline{\sigma}_{perc} \cong \begin{cases} \sigma_p \left(\frac{\epsilon_p - \epsilon_c}{1 - \epsilon_c} \right)^2 & \epsilon_c \leq \epsilon_p \leq 1 \\ 0 & 0 \leq \epsilon_p \leq \epsilon_c \end{cases}. \tag{3.9}$$

3.3 Diffusion in Porous Media

We now relate the conductivity to the effective diffusivity of the porous medium. The porosity is the volume of the electrolyte as a fraction of the total volume. If the porosity is assumed to be constant throughout the volume, then the area of each face of the volume is proportional to the porosity. Also, the total mass inside the volume is given by the volume averaged concentration, $\overline{c} = \epsilon_p c$. We begin with a mass balance on the volume,

$$\frac{\partial \overline{c}}{\partial t} + \nabla \cdot \mathbf{F} = 0, \tag{3.10}$$

where $\mathbf{F}$ is the flux at the surfaces of the volume. The net flux is

$$\mathbf{F} = -\overline{\sigma}_d \nabla c, \tag{3.11}$$

where c is the concentration in the pores and $\overline{\sigma}_d$ is the mean diffusive conductivity of the porous medium (with the same units as diffusivity, m^2/s), which, as the notation suggests, can be approximated or bounded by the conductivity formulae in the previous section, with σ_p replaced by the "free-solution" diffusivity D_p within the pores. It is important to recognize that fluxes are driven by gradients in the microscopic concentration within the pores, c, and not the macroscopic, volume-averaged concentration, $\bar{c}$. Regardless of porosity fluctuations in space, at equilibrium the concentration within the pores, which determines the local chemical potential, is constant throughout the volume.

Combining Equations (3.10) and (3.11), we get

$$\frac{\partial c}{\partial t} = \overline{D} \nabla^2 c, \tag{3.12}$$

where the effective diffusivity in a porous medium, $\overline{D}$, is given by

$$\overline{D} = \frac{\overline{\sigma}_d}{\epsilon_p}. \tag{3.13}$$

The reduction of the diffusivity inside a porous medium can be interpreted as a reduction of the mean free path. The tortuosity, τ_p, is often used to related the effective macroscopic diffusivity to the microscopic diffusivity within the pores,

$$\overline{D} = \frac{D_p}{\tau_p}, \tag{3.14}$$

as suggested long ago by Peterson [106]. One must keep in mind, however, that the tortuosity is just a way of interpreting the effective diffusivity in a porous medium, which is not rigorously related to any geometrical property of the microstructure. In Fick's Law, which involves one spatial derivative, the tortuosity can be interpreted as the ratio of an effective microscopic diffusion path length L_p to the macroscopic geometrical length: $L_p = \tau_p L$, although it is usually not clear exactly what kind of averaging is performed over all possible paths. Indeed, other definitions of tortuosity are also used [117]. (In particular, if the length rescaling concept is applied to the diffusion equation, which has two spatial derivatives, then the definition $\overline{D} = D_p/\tau^2$ is more natural, but equally arbitrary.)

In any case, using the definition above, the effective conductivity can be expressed as

$$\overline{\sigma}_d = \frac{D_p \epsilon_p}{\tau_p} \tag{3.15}$$

which allows us to interpret all the models and bounds above in terms of Peterson's tortuosity τ_p. The upper bounds on conductivity become lower bounds on tortuosity. The Wiener lower bound tortuosity for anisotropic pores is

$$\tau_p^{Wiener} = 1. \tag{3.16}$$

For the Hashin-Shtrikman model, the lower bound of the tortuosity is

$$\tau_p^{HS} = \frac{d - \epsilon_p}{d - 1} \tag{3.17}$$

in d dimensions. The percolation model produces a piecewise function for the tortuosity, above and below the critical porosity, which is given by

$$\tau_p^{perc} \cong \begin{cases} \epsilon_p \left(\frac{1-\epsilon_c}{\epsilon_p - \epsilon_c}\right)^2 & \epsilon_c \leq \epsilon_p \leq 1 \\ \infty & 0 \leq \epsilon_p \leq \epsilon_c \end{cases} \tag{3.18}$$

Note that, as the conductivity approaches zero, the tortuosity makes no physical sense as it no longer represents the extra path length. Instead it represents the decreasing number of available percolating paths, which are the cause of the lowered conductivity. Finally, from the Bruggeman relation we get the tortuosity formula,

$$\tau_p^B = \epsilon^{-1/2}, \tag{3.19}$$

which is widely used in porous electrode models for batteries, stemming from the work of J. Newman and collaborators. The different tortuosity models are plotted in Figure 3-6, and we note again the close comparison of the Bruggeman-Newman formula to the rigorous Hashin-Shtrikman upper bound for an isotropic porous medium.

3.4 Conclusion

This chapter introduced different models used to model effective transport properties of porous media. These effective properties are used throughout the rest of the thesis when dealing with porous transport. In the next chapter, the set of equations for Modified Porous Electrode Theory are derived. These equations, which are based on mass and charge conservation, use principles from this chapter, namely the effective diffusivity given by Equation 3.13 combined with a respective model of the conductivity. Later, when simulations are presented, the Bruggeman relation is used. Even

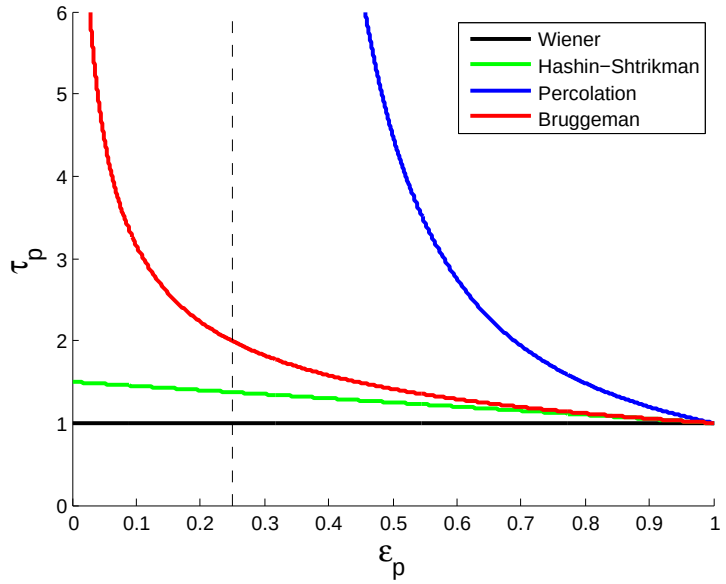

Figure 3-6: **Tortuosity versus porosity for different effective conductivity models**. This plot gives the tortuosity for different porosity values. While the Wiener and Hashin-Shtrikman models produce finite tortuosities, the percolation and Bruggeman models diverge as porosity goes to zero.

for cases of electrolyte transport limited discharge, which is shown in one of the later chapters, this model does a good job at fitting experimental data.

Chapter 4

Modified Porous Electrode Theory

This chapter will focus on the derivation of Modified Porous Electrode Theory (MPET). This derivation is the main focus of this thesis work as it combines a modified form of the Butler-Volmer equation with concentrated solution theory and the classical Porous Electrode Theory equations to create a set of thermodynamically consistent equations that can be used to model phase separating battery materials. This chapter is adapted from Ferguson and Bazant. [58] Changes have been made to clarify the derivation and correct mistakes in the original paper.

We begin with mass and charge conservation to derive the classical porous electrode theory equation. Then a modified form of the Butler-Volmer equation will be derived using the general reaction rate equation presented in Chapter 2. After that, modeling the potential of the electrons will be addressed, followed by how to model the intercalation particles. Finally, an overview of non-dimensionalization and scaling will be presented.

4.1 Mass and Charge Conservation

With concentrated solution theory, we can begin developing a self consistent set of equations, coupled to thermodynamics, to model transport and kinetics inside a porous electrode. The foundations of porous electrode theory are mass and charge conservation. Instead of simple diffusion, however, we now have to account for charged

species. First, we postulate the electrochemical potential of a charged particle as

$$\mu_{i,\pm} = \mu_i^o + k_B T \ln a_i \mp e z_i \phi, \tag{4.1}$$

where z_i is the species charge number (in this case, the absolute value), e is the charge per electron, and ϕ is the local potential. Inserting the electrochemical potential into the concentrated solution theory equation for the flux in Equation (2.21), we obtain the Nernst-Planck equation,

$$\mathbf{N}_{i,\pm} = -\epsilon D_{chem,i} \nabla c_i \mp z_i D_i \epsilon c_i \nabla \tilde{\phi}, \tag{4.2}$$

where the potential is scaled to the thermal voltage, $k_B T/e$. Note the chemical diffusivity of species i, $D_{chem,i}$, that was derived in Chapter 2. Also, since we want to address porous media, the area correction ϵ, the porosity, has been inserted. It is important to note that for the rest of this thesis, when the porosity precedes the diffusivity, it is implied that the diffusivity is the effective diffusivity, which can be modeled using the results of Chapter 3. For the case of the Bruggeman relation, which will be used in later chapters, the effective diffusivity is given by $D_{eff} = \epsilon^{1/2} D$.

Now, we make some assumptions regarding the electrolyte of this porous electrode in order to simplify some of the equations. First, we assume that the bulk is electroneutral, with a non-zero current density. Furthermore, we assume the electrolyte can be modeled as binary, although we do not assume it is symmetric.

For a binary system, we can write the cation and anion conservation equations as

$$\epsilon \frac{\partial c_+}{\partial t} = \nabla \cdot \left(\epsilon D_{chem,+} \nabla c_+ + z_+ D_+ \epsilon c_+ \nabla \tilde{\phi} \right) - R_+ \tag{4.3}$$

$$\epsilon \frac{\partial c_-}{\partial t} = \nabla \cdot \left(D_{chem,-} \nabla c_- - z_- D_- \epsilon c_- \nabla \tilde{\phi} \right) - R_-, \tag{4.4}$$

where $R_\pm$ is the volumetric consumption of the species via faradaic reaction. Electroneutrality approximates the charge density, ρ, as zero, and relates the cation and anion concentrations via

$$\rho = e z_+ c_+ - e z_- c_- \approx 0. \tag{4.5}$$

We use this to define our neutral concentration variable, c, given by

$$c = z_+ c_+ = z_- c_-. \tag{4.6}$$

In this binary system, the current density is given by the sum of the fluxes times the charge carried by the species. The current density is

$$\mathbf{i} = \sum_{i=1}^{N} e z_i \mathbf{N}_i, \tag{4.7}$$

where N is the number of species. Using the Nernst-Planck equation for a binary electrolyte, along with the electroneutrality approximation, the current density is

$$\mathbf{i} = -e\epsilon \left(D_{chem,+} - D_{chem,-}\right) \nabla c - e \left(z_+ D_+ + z_- D_-\right) \epsilon c \nabla \tilde{\phi}. \tag{4.8}$$

The electroneutrality approximation adds an additional constraint to the system. For a binary electrolyte, this additional constraint allows one of the variables to be eliminated. In this case, we can eliminate the electric field and derive an effective diffusivity for the electrolyte. Solving equation 4.8 for $\epsilon c \nabla \tilde{\phi}$ and assuming we have a non-zero current density, we obtain

$$\epsilon c \nabla \tilde{\phi} = -\frac{\epsilon \left(D_{chem,+} - D_{chem,-}\right)}{z_+ D_+ + z_- D_-} \nabla c - \frac{\mathbf{i}}{e \left(z_+ D_+ + z_- D_-\right)}. \tag{4.9}$$

Using this expression along with our electroneutrality approximation and conservation equations, we obtain

$$\epsilon \frac{\partial c}{\partial t} = \nabla \cdot \left(\epsilon D_{amb} \nabla c\right) - \nabla \cdot \left(\frac{t_+ \mathbf{i}}{e}\right) + \nabla \cdot \frac{\mathbf{i}}{2e} - \frac{z_+ R_+}{2} - \frac{z_- R_-}{2}, \tag{4.10}$$

where

$$D_{amb} \equiv \frac{z_+ D_+ D_{chem,-} + z_- D_- D_{chem,+}}{z_+ D_+ + z_- D_-}. \tag{4.11}$$

Charge conservation,

$$e z_+ R_+ - e z_- R_- = -\nabla \cdot \mathbf{i}, \tag{4.12}$$

can be used to eliminate the anion reaction rate, yielding our conservation equation,

$$\epsilon \frac{\partial c}{\partial t} = \nabla \cdot (\epsilon D_{amb} \nabla c) - \nabla \cdot \left(\frac{t_+ \mathbf{i}}{e} \right) - z_+ R_+ \tag{4.13}$$

In a lithium-ion battery, if we assume that only the cation reacts(which is reasonable if SEI formation at the graphite anode is ignored), the cation reaction rate can be replaced via

$$z_+ R_+ = a_p j_{in}, \tag{4.14}$$

where a_p is the active particle area per active particle volume and j_{in} is the reaction rate (typically as a function of local concentrations and potential). This substitution recovers the classical Porous Electrode Theory (PET) mass conservation equation,

$$\epsilon \frac{\partial c}{\partial t} + a_p j_{in} = \nabla \cdot (\epsilon D_{amb} \nabla c) - \nabla \cdot \left(\frac{t_+ \mathbf{i}}{e} \right). \tag{4.15}$$

To complete the set of equations, we require a thermodynamically consistent reaction rate that depends on species activities. This reaction rate is the modified Butler-Volmer equation and will be derived later in the chapter. First, an expression for the equilibrium potential is required. This equilibrium potential is necessary because it is later combined with two Tafel expressions to form the modified Butler-Volmer equation.

4.2 Faradaic Reaction Kinetics

To complete the reaction-diffusion equation, a suitable model for the reaction rate is needed. In electrochemistry, the Butler-Volmer equation is the standard for modeling reaction kinetics. The Butler-Volmer equation combines two Tafel expressions to handle the forward and reverse reaction rates. The exchange current density represents the background current (e.g. an attempt frequency) and the Tafel expressions skew the forward or reverse reaction depending on the sign of the applied overpotential. Classical Porous Electrode Theory uses an exchange current density model that

depends on local concentrations of the solid and the electrolyte.

While this is suitable in the dilute limit and generally for materials that behave homogeneously, it is unclear whether or not this model is applicable for phase separating materials that demonstrate complex dynamics and have concentration gradients at the surface. In this chapter, starting with the general reaction rate expression in 2.10, a modified form of the Butler-Volmer equation is derived. This modified form uses the activity of the particle surface to calculate an exchange current density to account for more complex behavior, such as phase separation, surface energy, and coherency strain.

4.2.1 The Nernst Equation

We begin with a general charge transfer reaction, where an oxidant is combined with n electrons to become a reductant,

$$\mathrm{O} + ne^- \leftrightharpoons \mathrm{R}. \tag{4.16}$$

We use Equation (4.1) and assume that the potentials of the oxidant and reductant are ϕ, and that the electron enters at a different potential, ϕ_M. Using this equation, the chemical potentials are modeled as

$$\mu_O = \mu_O^o + k_B T \ln a_O + e z_O \phi, \tag{4.17}$$

$$\mu_R = \mu_R^o + k_B T \ln a_R + e z_R \phi, \tag{4.18}$$

$$\mu_e = \mu_e^o + k_B T \ln a_e - ne\phi_M. \tag{4.19}$$

At equilibrium, the sum of the chemical potentials on each side of the equation is equal,

$$\mu_O + n\mu_e = \mu_R. \tag{4.20}$$

We can define the observed potential difference as $\Delta\phi = \phi_M - \phi$. At equilibrium, we denote this as $\Delta\phi_{eq}$. Charge conservation dictates that $z_O - n - z_R = 0$. Substituting

the chemical potentials into the equilibrium condition and solving for the equilibrium potential, $\Delta\phi_{eq}$, we obtain the Nernst Equation,

$$\Delta\phi_{eq} = V^o + \frac{k_B T}{ne} \ln \frac{a_O a_e^n}{a_R}, \tag{4.21}$$

where V^o, the standard potential, is

$$V^o = \frac{\mu_O^o + \mu_e^o - \mu_R^o}{ne}. \tag{4.22}$$

The standard potential relates the equilibrium potential to the reference state. It is important to note that at the reference state, the activities are unity and the standard potential is recovered.

The activities of the oxidant and reductant can be modeled using any appropriate thermodynamic model and activity coefficient data are even listed for some materials and electrolyte solutions. However, modeling the chemical potential of the electron is not as straightforward, and can play a large role in materials where electron conduction is poor.

4.2.2 The Modified Butler-Volmer Equation

Modeling the charge transfer reaction to use in the porous electrode theory equation requires a different approach from the classical Butler-Volmer equation. The activity of the reactants and products needs to be accounted for, and the transition state needs to be considered. To derive the modified Butler-Volmer equation, we begin with the general reaction rate presented in Equation (2.10). To use this general reaction rate equation, we need to postulate forms of the chemical potentials of the reactants, products, and transition state for the general charge transfer reaction presented in Equation (4.16).

Modeling the chemical potentials of the oxidant and reductant are straightforward using the electrochemical potential equation presented in Equation (4.1). However, modeling the excess chemical potential of the transition state requires some assump-

tions. Here we make the assumption that the potential of the transition state is a linear combination of the two present potentials (i.e. the ion potential ϕ and the electron potential ϕ_M). The coefficient α denotes the symmetry of the transition state. This coefficient is referred to as the charge transfer coefficient.

For simplicity, here we refer to dimensionless chemical potentials, denoted by a tilde and scaled to the thermal energy (k_BT), $\tilde{\mu} = \mu/k_BT$. The potential is scaled to the thermal voltage (k_BT/e). Here, state 1 is the oxidant and electron and state 2 is the reductant. The postulated chemical potentials are

$$\tilde{\mu}_1 = \tilde{\mu}_O^o + \tilde{\mu}_e^o + \ln a_O + \ln a_e^n + q_O\tilde{\phi} - n\tilde{\phi_M} \tag{4.23}$$

$$\tilde{\mu}_2 = \tilde{\mu}_R^o + \ln a_R + q_R\tilde{\phi} \tag{4.24}$$

$$\tilde{\mu}_{TS}^{EX} = \tilde{\mu}_{TS}^o + \ln \gamma_{TS} + \alpha q_R\tilde{\phi} + (1-\alpha)\left(q_O\tilde{\phi} - n\tilde{\phi}_M\right). \tag{4.25}$$

Next, we define the potential difference $\Delta\tilde{\phi}$ as before, as

$$\Delta\tilde{\phi} \equiv \tilde{\phi}_M - \tilde{\phi}. \tag{4.26}$$

Finally, we define the overpotential η (has units of volts) as the difference between the observed potential, $\Delta\phi$, and the equilibrium potential, given by the Nernst equation, $\Delta\phi_{eq}$,

$$\tilde{\eta} \equiv \Delta\tilde{\phi} - \Delta\tilde{\phi}_{eq}. \tag{4.27}$$

Using the chemical potentials, the potential difference, and the overpotential, we substitute all of these into the generic reaction rate expression in Equation (2.10). After simplification, we obtain an expression for the charge transfer reaction,

$$R = \frac{k^o a_R^\alpha \left(a_O a_e^n\right)^{1-\alpha}}{\gamma_{TS}} \left[\exp\left(-\alpha n\tilde{\eta}\right) - \exp\left((1-\alpha)\, n\tilde{\eta}\right)\right], \tag{4.28}$$

where the modified rate constant, k^o, is given by

$$k^o = k_o \exp\left[(1-\alpha)\left(\tilde{\mu}_O^o + \tilde{\mu}_e^o\right) + \alpha\tilde{\mu}_R^o - \tilde{\mu}_{TS}^o\right]. \tag{4.29}$$

Finally, to relate this faradaic reaction rate to the Butler-Volmer expression (which has units of current), the reaction rate is converted to a current via $i = neAR$ (the rate constant has units of $\mathrm{m}^{-2}\mathrm{s}^{-1}$). This yields our modified Butler-Volmer expression for the current,

$$i = i_o \left[\exp\left(-\alpha n\tilde{\eta}\right) - \exp\left(\left(1-\alpha\right) n\tilde{\eta}\right)\right], \tag{4.30}$$

where the exchange current, i_o, is given by

$$i_o = \frac{neAk^o a_R^{\alpha} \left(a_O a_e^n\right)^{1-\alpha}}{\gamma_{TS}}. \tag{4.31}$$

4.3 Potential Drop in the Solid Conducting Phase

The importance of the electron potential has been shown in the reaction rate, where it contributes to the potential difference, $\Delta\phi$. For a porous electrode, electrons conduct through the solid matrix (e.g. carbon black). The aforementioned modeling methods for porous media (in Chapter 3) can also be applied to this solid matrix.

Regardless of the model used, charge conservation dictates the general behavior of the potential drop of the electrons. The electronic current in the electrode is denoted here by $\mathbf{i}_M$. Current conservation throughout the entire electrode is given by

$$\mathbf{i} + \mathbf{i}_M = I/A_{sep}, \tag{4.32}$$

where $\mathbf{i}$ is the current density in the electrolyte, $\mathbf{i}_M$ is the current density in the solid phase (i.e. the flux of electrons in the solid matrix), I is the total current, and A_{sep} is the area of the separator. This expression shows how during constant current discharge, while the electronic or ionic current may go to zero at the boundaries, the total current is conserved throughout the cell.

For constant current discharge (i.e. I is constant), taking the divergence of Equation (4.32) gives the relation between the ionic and electronic current densities,

$$\nabla \cdot \mathbf{i} = -\nabla \cdot \mathbf{i}_M. \tag{4.33}$$

Using the charge conservation for the electrolyte phase, which relates the divergence of the current density to the local reaction rate, we obtain an expression that can be used to obtain the potential drop in the solid conducting phase,

$$ez_+R_+ - ez_-R_- = \nabla \cdot \mathbf{i}_M. \tag{4.34}$$

To complete this equation, an expression is needed for the current density in the solid conducting phase. This current density can be modeled using an Ohmic drop,

$$\mathbf{i}_M = -\sigma_m \nabla \phi_M. \tag{4.35}$$

The conductivity of the solid matrix, σ_M can be modeled any of the previous porous media models. Furthermore, more complicated effects can be included in this term to account for the conductivity of the active material and the variable loading percent of active material throughout the electrode. Incorporating this potential drop into the porous electrode theory equations involves using Equation (4.34) to calculate the potential field of the electrons, and then using this field to calculate $\Delta\phi$ and the overpotential, η.

While this derivation was for constant current (to demonstrate charge conservation throughout the electrode), the same principle can be applied for constant potential discharge. Regardless of the discharge method (i.e. constant current/potential/power), local charge conservation still applies throughout the electrode, and must be applied on a per volume (or element) basis in the numerical scheme. For a discretized volume of the electrode, Equation 4.34 applies, regardless of the type of discharge being simulated.

4.4 Diffusion in the Solid

Modeling transport inside the active particles requires the use of concentrated solution theory. The flux, as given by Equation 2.21, is given by

$$\mathbf{N}_s = -Mc_s\nabla\mu, \tag{4.36}$$

where c_s denotes the lithium concentration inside the solid particle. Since there are no source or sink terms inside the particles, and lithium only enters via the interface with the electrolyte, the conservation equation is

$$\frac{\partial c_s}{\partial t} = -\nabla\cdot\mathbf{N}_s. \tag{4.37}$$

This conservation equation requires two boundary conditions. In classical porous electrode theory, the solid intercalation particles are modeled as spheres, with the Butler-Volmer reaction giving the surface flux, and a no-flux/symmetry condition at the center of the particles. These boundary conditions are given by

$$D_s\frac{\partial c_s}{\partial r}\bigg|_{r=R} = j_{in}, \text{ and} \tag{4.38}$$

$$\frac{\partial c_s}{\partial r}\bigg|_{r=0} = 0. \tag{4.39}$$

Another particle geometry presented in this work, is the surface reaction limited model, in which the surface of a particle is modeled and the concentration in the depth direction is averaged. In this case, only Equation (4.38) is used, since diffusion in the solid is no longer modeled and the additional boundary condition is not used. This model will be explained in depth in later sections.

At this point, a suitable free energy equation is needed to model the transport inside the solid. For homogeneous materials, a suitable model is the regular solution model, which models entropic effects and pairwise enthalpic effects. For phase separating materials, the Cahn-Hilliard free energy functional [34, 36] can be used. Other effects, such as interfacial energies and coherency strain can also be included

in the free energy. In this section, an overview of the regular solution model and the Cahn-Hilliard free energy functional (with an approximate strain energy) will be presented.

4.4.1 The Regular Solution Model

The regular solution model includes entropic and pairwise enthalpic effects. The model is

$$g = k_B T \left[\tilde{c}_s \ln \tilde{c}_s + (1 - \tilde{c}_s) \ln (1 - \tilde{c}_s)\right] + \Omega \tilde{c}_s (1 - \tilde{c}_s), \tag{4.40}$$

where $\tilde{c}_s$ is the dimensionless solid concentration ($c_s/c_{s,max}$) and Ω is the pairwise interaction energy. The regular solution model is capable of producing homogeneous free energy curves with a minimum at half filling, as well as double-well free energy profiles, that have a tendency to phase separate (with the two local minima representing the concentrations of each phase, and a tie line with which the lever rule can be used to determine the amount of each phase). The concentration range between these minima is referred to as the *miscibility gap*. The inflection points in the free energy curve (i.e. where the second derivative is zero) are referred to as the *spinodal points* and the range in between them is referred to as the *spinodal gap*. For $\Omega > 2k_B T$, there are two local minima. If $\Omega \leq 2k_B T$, a single global minimum exists and all concentrations are accessible. Figure 4-1 shows the energy profiles for different values of Ω.

For the case of two local minima (i.e. $\Omega > 2k_B T$), the spinodal points are of interest as they represent the limit of a homogeneous mixture. Inside the spinodal gap, the mixture is unstable with respect to infinitesimal perturbations. This can be seen graphically using a tie line. Inside the spinodal gap, small concentration fluctuations grow, as small deviations from the homogeneous concentration lower the free energy. This instability continues until the concentrations at the edge of the miscibility gap are attained, producing a phase separation. Modeling phase separation requires additional terms not in the regular solution model, however, and will be addressed in the next section.

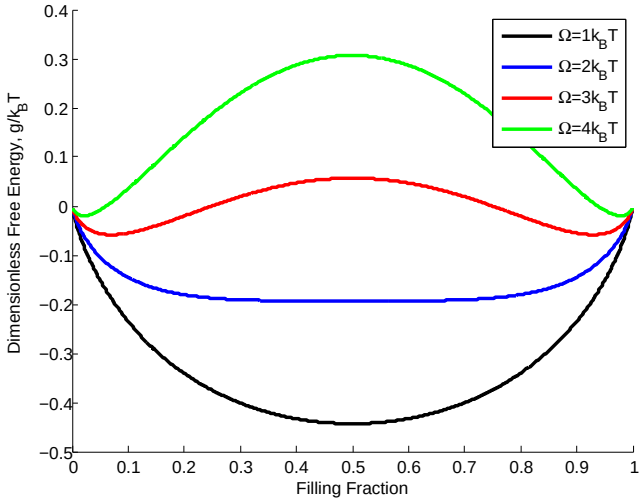

Figure 4-1: **Regular solution model for the free energy of a homogeneous mixture**. This figure shows the effect of the regular solution parameter Ω (mean pair interaction energy) and temperature T on the free energy versus filling fraction c of a regular solution of atoms and vacancies on a lattice. For $\Omega < 2k_BT$, there is a single minimum. For $\Omega > 2k_BT$, there are two minima. This produces phase separation, as the system is unstable with respect to infinitesimal perturbations near the spinodal concentration, which is where the curvature of the free energy changes.

In this section we aim to connect concentrated solution theory with Fick's Law. The chemical potential is calculated by taking the derivative of the free energy with respect to concentration. The chemical potential of the regular solution model is

$$\mu \equiv \frac{\partial g}{\partial \tilde{c}_s} = k_B T \ln\left(\frac{\tilde{c}_s}{1-\tilde{c}_s}\right) + \Omega\left(1-2\tilde{c}_s\right). \tag{4.41}$$

Using this equation, the chemical diffusivity can be calculated using the definition of the chemical diffusivity in Equation (2.23). Additionally, a model of the transition state is required. Here it will be assumed that the transition state occupies two lattice sites (i.e. the transition state sits between lattice sites). Equation (4.37) can be rewritten as

$$\frac{\partial c_s}{\partial t} = \nabla \cdot \left(D_{chem} \nabla c_s\right), \tag{4.42}$$

where D_{chem} is given by

$$D_{chem} = D\left(1 + \frac{\partial \ln \gamma}{\partial \ln \tilde{c}_s}\right), \tag{4.43}$$

and $D = D_o\gamma/\gamma_{TS}$. Substituting the regular solution chemical potential into Equations (4.42) and (4.43), along with the diffusivity definition, the chemical diffusivity for the regular solution model is

$$D_{chem,rs} = D_o\left(2\tilde{\Omega}\tilde{c}_s^2 - 2\tilde{\Omega}\tilde{c}_s + 1\right)\exp\left(\tilde{\Omega}\left(1 - 2\tilde{c}_s\right)\right), \tag{4.44}$$

where $\tilde{\Omega} = \Omega/k_BT$. In the dilute limit, we find that we obtain the dilute limit diffusivity multiplied by some constant. This constant is related to the particle-hole interaction energy given by Ω. Interestingly enough, this model recovers some interesting phenomena for different values of Ω. For $\Omega < 0$, the chemical diffusivity increases and approaches a constant value at full filling. For $\Omega = 0$, the dilute limit (i.e. ideal) diffusivity is recovered. Finally, for $\Omega > 0$, there is a minimum in the diffusivity between zero and half filling. As $\Omega \to 2k_BT$, the minimum diffusivity approaches zero at half filling. Beyond $2k_BT$, the diffusivity is negative, indicative of phase separation (i.e. "uphill diffusion").

In order to simulate this regime, an additional energetic term is required. Uphill diffusion is not only numerically difficult, it also doesn't accurately represent experimental data. When modeling phase separating systems, this negative diffusivity is handled by using an additional gradient penalty, so that the problem is formulated as diffusion down an energy gradient, instead of up a concentration gradient. This method also more accurately represents experimental data. This is the purpose of the Cahn-Hilliard free energy functional, which will be introduced in the next section.

4.4.2 The Cahn-Hilliard Free Energy Functional

The Cahn-Hilliard free energy functional includes a "gradient penalty" that stabilizes the interface between phases of high and low concentration. Instead of apparent uphill diffusion, which is numerically unstable, the resulting equation is always a minimization in energy, and particles travel down the energy gradient. The functional is

$$G[\tilde{c}(x)] = \int_V \left[\rho_s\overline{g}(\tilde{c}) + \frac{1}{2}\kappa\left(\nabla\tilde{c}\right)^2\right]dV + \int_A \gamma_s\left(\tilde{c}\right)dA, \tag{4.45}$$

where ρ_s is the site density, $\overline{g}$ is the homogeneous free energy, κ is the gradient energy (energy per length) and γ_s is the surface tension (energy per area). During phase separation, the gradient penalty controls the structure of the phase interface. Balancing the terms in Equation (4.45) with the regular solution model as the homogeneous free energy, it can be shown that the width of the phase interface scales as $\lambda_i \approx \sqrt{\kappa/\Omega}$ and the interphasial tension scales as $\gamma_i \approx \rho_s\sqrt{\kappa\Omega}$.

The concentrated solution theory formulation requires the chemical potential. To calculate the chemical potential from the Cahn-Hilliard free energy functional (which is a total free energy), the Euler-Lagrange variational derivative with respect to concentration is required. This is the continuum equivalent to the change in free energy to add an atom to the system. The chemical potential per site is

$$\mu = \frac{1}{\rho_s}\frac{\delta G}{\delta \tilde{c}} = \overline{\mu}\left(\tilde{c}\right) - \nabla\cdot\left(\frac{\kappa}{\rho_s}\nabla\tilde{c}\right) \tag{4.46}$$

Inserting this chemical potential into concentrated solution theory flux in Equation (4.36) and the overall conservation equation in Equation (4.37) results in a fourth order partial differential equation. This higher order differential equation requires an additional boundary condition. The additional boundary condition comes from the variational calculus, and is given by

$$\hat{n}\cdot\kappa\nabla\tilde{c} = \frac{\partial\gamma_s}{\partial\tilde{c}}. \tag{4.47}$$

This term ensures continuity of the chemical potential [32] and controls surface wetting and nucleation. [8, 45, 44] Additional effects such as coherency strain can be included in the Cahn-Hilliard model as well. If the surface term is neglected, but the elastic strain energy and homogeneous component of the total strain are included, the free energy equation becomes

$$G[\tilde{c}(x)] = \int_V \left[\rho_s\overline{g}(\tilde{c}) + \frac{1}{2}\kappa\left(\nabla\tilde{c}\right)^2 + \frac{1}{2}C_{ijkl}\varepsilon_{ij}\varepsilon_{kl} - \overline{\sigma}_{ij}\overline{\varepsilon}_{ij}\right]dV. \tag{4.48}$$

These additional effects of coherency strain can be approximated by a volume av-

eraged stress term. [36, 37, 38] The homogeneous component of the total strain becomes

$$\frac{1}{2}C_{ijkl}\varepsilon_{ij}\varepsilon_{kl} \approx \frac{1}{2}B\left(\tilde{c} - X\right)^2, \tag{4.49}$$

where X is the volume averaged concentration. This term penalizes concentration fluctuations from the volume averaged concentration and suppresses phase separation depending on the value of B, which typically depends on orientation. [45] Including this approximate strain term in the chemical potential as in Equation (4.46) yields

$$\mu = \overline{\mu} - \nabla \cdot \left(\frac{\kappa}{\rho_s}\nabla\tilde{c}\right) + \frac{B}{\rho_s}\left(\tilde{c} - X\right). \tag{4.50}$$

This additional strain term effectively suppresses phase separation inside the nanoparticles. The effects of different values of this parameter will be shown in model simulations in later chapters. Adding the strain term represents just one of the additional features that can be included in the solid particles. The benefit of this modified porous electrode theory formulation is that any energetic model can be included, allowing for more complicated phenomena such as phase separation and stress effects to be modeled via simply changing the free energy function. This allows the same framework to be used and prevents having to adapt the equations to artificially insert these phenomena.

4.5 Non-dimensionalization and Scaling

At this point, the equations governing the dynamics of the battery system have all been introduced. Mass and charge conservation equations govern the dynamics of lithium inside the electrolyte. In the porous electrode, models of effective diffusivity and conductivity are used for volume averaged continuum modeling. A modified form of the Butler-Volmer equation along with the Nernst potential and the potential drop in the solid conducting phase have also been presented. These terms allow the reaction rate to be modeled throughout the electrode. Additionally, concentrated solution theory can be used inside the solid particles, allowing more complicated

dynamics such as phase separation to be modeled in a coupled and self-consistent manner.

Prior to solving these equations, however, suitable scalings allow dimensionless quantities to be identified. These dimensionless quantities often govern the behavior of the equations and allow different regimes to be identified. Additionally, proper scaling makes the set of equations more numerically stable by removing some of the stiffness associated with different time and length scales in the equations. This section will deal with scaling of one of the electrodes. The scale can easily be extended to the other electrode. It is important to note, though, that when scaling two electrodes in this manner, a reference capacity is required. It is best to choose the smallest capacity electrode as the scaling, so the total capacity of the cell is scaled to one. Choosing the larger capacity electrode will lead to dimensionless currents that don't scale to one.

To begin, the total current (i.e. the integral of all fluxes times the area of the particles) is scaled by the total electrode capacity. The total current is an integral over the entire area of the solid, A_s, given by

$$I = \int_{A_s} e j_{in} dA_s = \int_{V_s} e a_v j_{in} dV_s. \tag{4.51}$$

The term a_v, the interfacial area per particle volume, relates the solid interfacial area to particle area. This is slightly different from the total particle area per electrode volume, a_p. The two terms are related via

$$a_p = (1 - \epsilon) L_p a_v, \tag{4.52}$$

where L_p is the volume fraction of the active material of the total solid volume. The total current integrates over the entire solid volume in the electrode.

To scale the current, a time scale and charge scale are required. It is most convenient to use the diffusive time scale, t_d, and the total charge of the electrode. The diffusive time scale is set by electrode length, L, and the dilute limit ambipolar diffusivity, $D_{amb,o}$. The time scale is $t_d = L^2/D_{amb,o}$. The total charge capacity of

the electrode is given by $e\left(1-\epsilon\right)L_pVc_{s,max}$, where e is the charge per particle, ϵ is the porosity, V is the total volume of the electrode, and $c_{s,max}$ is the maximum concentration of lithium in the active material. The dimensionless current is

$$\tilde{I} = \frac{It_d}{e\left(1-\epsilon\right)L_pVc_{s,max}} = \int_{\tilde{V}} \tilde{j}_{in} d\tilde{V}. \tag{4.53}$$

The dimensionless current is effectively a dimensionless C-rate. The term C-rate is used for constant current battery discharge to denote the time in hours taken to discharge the entire cell. An "n" C-rate is the same as discharging a cell in 1/n hours. Since the diffusive time is on the order of 10 seconds, dimensionless C-rates are typically much less than 1. A dimensionless C-rate of 0.003 is on the order of a dimensional C-rate of 1. The dimensionless surface flux, j_{in} is

$$\tilde{j}_{in} = \frac{a_v j_{in} t_d}{c_{s,max}}. \tag{4.54}$$

Next a proper scaling of the current density in the electrolyte is necessary. Since the current density depends on the electrolyte concentration, it is scaled to the initial electrolyte concentration, c_o. This is the concentration of lithium in the electrolyte at open circuit conditions. The dimensionless current density is

$$\tilde{i} = -\epsilon\left(\tilde{D}_{chem,+} - \tilde{D}_{chem,-}\right)\tilde{\nabla}\tilde{c} - \left(z_+\tilde{D}_+ + z_-\tilde{D}_-\right)\epsilon\tilde{c}\tilde{\nabla}\tilde{\phi}, \tag{4.55}$$

where the diffusivities have been scaled to the dilute limit ambipolar diffusivity. For the case of a symmetric (i.e. $z_+ = z_-$) binary electrolyte, the dimensionless cation and anion diffusivities are controlled by the transference number (Note: $t_+ + t_- = 1$ by definition). The dimensionless diffusivities (for the symmetric case) can be expressed as

$$\tilde{D}_+ = \left(2t_-\right)^{-1}, \text{and} \tag{4.56}$$

$$\tilde{D}_- = \left(2t_+\right)^{-1}. \tag{4.57}$$

Using these scalings, the dimensionless current density is given by

$$\tilde{i} = \frac{it_d}{Lec_o}, \tag{4.58}$$

where L is the length of the electrode. Next the charge conservation is non-dimensionalized. The divergence of the current density is equal to the local charge consumption. Since the electrolyte concentration is scaled to the initial electrolyte concentration, and the reaction flux is scaled to the solid concentration, a scaling parameter remains after non-dimensionalization. The charge conservation equation is

$$\epsilon\beta\tilde{j}_{in} = -\tilde{\nabla}\cdot\tilde{\mathbf{i}}, \tag{4.59}$$

where $\beta = V_s c_{s,max}/V_e c_o$, and represents the ratio of lithium in the solid to lithium in the electrolyte at open circuit conditions. This parameter is important as it represents the different regimes of charge storage. For $\beta \gg 1$, the system behaves as a battery, with high storage in the solid intercalation material. When $\beta \ll 1$, the system behaves like a super capacitor, which allows very fast charge storage. When $\beta \sim 1$, the system can be considered a pseudocapacitor, as this ratio of charge storage represents a combination of surface storage and faradaic reactions.

Applying these scalings to the mass conservation equation, all scaling terms drop out except for the β parameter. The dimensionless mass conservation equation is

$$\epsilon\frac{\partial\tilde{c}}{\partial\tilde{t}} + \epsilon\beta\tilde{j}_{in} = \tilde{\nabla}\cdot\left(\epsilon\tilde{D}_{amb}\tilde{\nabla}\tilde{c}\right) - \tilde{\nabla}\cdot\left(t_+\tilde{\mathbf{i}}\right). \tag{4.60}$$

All gradient operators are scaled by the electrode length, L, and the ambipolar diffusivity is scaled by the dilute limit ambipolar diffusivity, $D_{amb,o}$.

The solid diffusion equation must be scaled as well. The natural time scale in the solid conservation equation is the solid diffusive time, L_s^2/D_{chem}, where L_s is the length of the solid particle. However, since a single dimensionless time scale is

required, the parameter δ_d is introduced, which is a ratio of the diffusive time scales,

$$\delta_d = \frac{L_s^2 D_{amb}}{L^2 D_{s,o}}, \tag{4.61}$$

where $D_{s,o}$ is the dilute limit solid diffusivity (considered constant). Applying this to the solid conservation equation, we obtain

$$\delta_d \frac{\partial \tilde{c}_s}{\partial \tilde{t}} = \tilde{\nabla}_s \cdot \left(\tilde{D}_s \tilde{c}_s \tilde{\nabla}_s \tilde{\mu} \right), \tag{4.62}$$

where $\tilde{\nabla}_s$ are the gradient operators scaled by the characteristic solid length scale, L_s, $\tilde{c}_s$ is the solid concentration scaled by the maximum solid concentration $c_{s,max}$, D_s is the solid diffusivity scaled by the dilute limit solid diffusivity, $D_{s,o}$, and the dimensionless chemical potential of the solid $\tilde{\mu}$ is scaled by the thermal energy, $k_B T$. This equation allows the solid dynamics to be modeled with respect to the diffusive time chosen in the electrolyte conservation equation. The parameter δ_d scales inversely with the solid diffusivity (i.e. slower diffusion is a larger δ_d) and proportionally with the square of the characteristic solid particle length.

4.6 Conclusion

This chapter showed the derivation of the MPET equations as well as some free energy equations and ways to handle phase separating materials. Table 4.1 lists the full set of dimensional equations used in MPET along with suitable boundary conditions. Other boundary conditions, such as the no-flux conditions for lithium at the current collectors and walls of the electrodes, are not explicitly stated here. Depending on the simulation (i.e. half cell or full cell) these boundary conditions are obvious. The not as obvious boundary conditions, such as the flux into the separator, are given for constant current discharge. In the case of constant potential discharge, the potential boundary condition is held constant and the flux is varied to satisfy mass conservation. Constant power discharge can also be performed by solving for the cell potential that satisfies the constant power condition (i.e. the instantaneous potential multiplied by

the instantaneous current).

Equation	Boundary Conditions
$\epsilon\frac{\partial c}{\partial t} + a_p j_{in} = \nabla \cdot (\epsilon D_{amb} \nabla c) - \nabla \cdot \left(\frac{t_+ \mathbf{i}}{e}\right)$	$\mathbf{i}\|_{x=-\delta_s} = I/A_{sep}$
$\mathbf{i} = -e\left(D_+ - D_-\right)\epsilon\nabla c - \frac{e^2}{k_B T}\left(z_+ D_+ + z_- D_-\right)\epsilon c \nabla\phi$	
$j_{in} = -\frac{\nabla\cdot\mathbf{i}}{e a_p} = i_o\left[\exp\left(-\frac{\alpha e\eta}{k_B T}\right) - \exp\left(\frac{(1-\alpha)e\eta}{k_B T}\right)\right]$	
$i_o = \frac{e(k_c^o a_O)^{1-\alpha}(k_a^o a_R)^{\alpha}}{\gamma_\ddagger}$	
$\eta \equiv \Delta\phi - \Delta\phi_{eq}$	
$\Delta\phi_{eq} = V^o - \frac{k_B T}{ne}\ln\left(\frac{a_R}{a_O}\right)$	
$\frac{\partial c_s}{\partial t} = \nabla \cdot \left(\frac{D_s c_s}{k_B T}\nabla\mu\right)$	$-\frac{D_s c_s}{k_B T}\frac{\partial\mu}{\partial r}\Big\|_{r=R} = j_{in}$

Table 4.1: **Dimensional set of equations**. A list of the set of dimensional equations for Modified Porous Electrode Theory. The boundary conditions listed here are for constant current discharge.

The conservation equation applies throughout the electrode volume. The current density equation is used to calculate the potential drop in the electrolyte. This term is important because it is required to calculate the observed potential, $\Delta\phi$. The reaction rate equation, which is based on a modified form of the Butler-Volmer equation, is used to calculate the reaction rate of the intercalation particles. This reaction rate governs the flux of lithium into or out of the particles. This is the only way the

particles interact with the electrolyte. The dynamics inside the particles are handled using concentrated solution theory. The type of coordinates for the particles should be selected to best handle the particle geometry.

The Nernst potential of the intercalation particles is modeled using the same thermodynamics used in the reaction rate and diffusion equations. This open circuit potential is what controls the cell of the electrode as the particles fill. This feature is what makes the MPET set of equations unique. The equations are fully self consistent and the dynamics and potential of the cell are governed by the thermodynamics of the material. While this is a strength of the model, this can also be problematic, because the model itself relies on a thorough understanding of the material's thermodynamic properties in order to predict non-equilibrium dynamics. Neglecting one feature of the material can result in a model which cannot fit experimental data. However, if the thermodynamics are well known, then the model has the potential to provide a much deeper understanding of the behavior of the material inside the electrode.

Chapter 5

Numerical Methods

Numerical methods are not the focus of this research, but it is necessary to comment on which methods were used to solve the set of equations. The set of PDE's was reduced to a set of ODE's using the finite volume method to approximate the spatial derivatives. The problem was then formulated as a differential algebraic equation (DAE) in order to solve the time integration. DAE's consist of differential equations (e.g. a time derivative) with algebraic constraints, which in this case are the charge conservation conditions. Additionally, for the constant current, the integral of the reaction rate is controlled (i.e. the potential that satisfies the current is simultaneously solved for). For constant power discharge, the power is controlled (i.e. the potential is solved for such that the product of the instantaneous potential and current is constant).

This set of equations is well suited to be formulated as an index 1 DAE. The index of a DAE is defined as the number of derivatives required to turn the equations into an explicit ODE. Often the most difficult part of solving DAE's is finding a consistent set of initial conditions that satisfies the algebraic constraints. Higher index DAE's (i.e. index greater than 1) are difficult to solve because the initial conditions must also satisfy derivatives of the constraints in the system. A brief overview of DAE properties and solution approaches will be presented here. For more on DAE's, DAE index, and solution methods, the reader is directed to Ascher and Petzold. [4]

The solver used for this work is MATLAB's `ode15s`, which is a variable first to

fifth order stiff equation solver. The solver uses a mass matrix formulation of the DAE, which will be explained later in this chapter. First a brief overview of the finite volume method will be presented, followed by a brief section on DAE formulation using a mass matrix. Finally, an example of setting up a half cell for constant current discharge will be given along with various constraints for different simulation types (constant current, constant potential, constant power, etc.).

5.1 The Finite Volume Method

In this section, a brief overview of the centered finite volume method will be given. The finite volume method conserves mass perfectly by tracking fluxes over the boundaries of a control volume. We refer to the method presented here as "centered" because field variables (e.g. concentration and potential) represent values at the center of the volume. Fluxes are therefore defined on the boundaries of the volume.

The advantage of this discretization method is that mass is perfectly conserved. All fluxes in and out of a control volume are balanced with the local reaction rate and accumulation term. For Neumann boundary conditions, setting the flux on the boundary is straightforward. This can be accomplished by placing a dummy volume outside the grid, or changing the value after the gradient is computed (i.e. altering a value inside a "flux" vector).

Dirichlet boundary conditions require an approximation. Approximating the value of a dummy volume outside the grid is one way to apply a Dirichlet boundary condition. As a rough first approximation, the dummy volume right outside the boundary can be set to the boundary value. If higher accuracy is required, a Taylor approximation for this dummy volume can be used which takes into account the set value of the boundary. Approximating a function $f(x)$ using a Taylor expansion around $x = a$ is given by

$$f(x) \approx f(a) + \frac{1}{1!}\left.\frac{df}{dx}\right|_{x=a}(x-a) + \frac{1}{2!}\left.\frac{d^2f}{dx^2}\right|_{x=a}(x-a)^2 + ... \tag{5.1}$$

Using finite difference methods to approximate the derivatives, an expression that satisfies the boundary condition can be calculated for the dummy volume.

The finite volume method integrates the conservation equation over the discretized volume. Consider a 1D conservation equation with no reaction rate and a constant diffusivity, given by

$$\frac{\partial c}{\partial t} = D\frac{\partial^2 c}{\partial x^2}. \tag{5.2}$$

First, we consider a grid of discrete elements each with length Δx. Integrating Equation (5.2) over the spatial direction, x, yields

$$\int_{x_o}^{x_o+\Delta x} \frac{\partial c}{\partial t} dx = \int_{x_o}^{x_o+\Delta x} D\frac{\partial^2 c}{\partial x^2} dx. \tag{5.3}$$

Carrying out the integration over the length of the finite volume (i.e. x_o to $x_o + \Delta x$) and applying the Fundamental Theorem of Calculus, this equation becomes

$$\frac{\partial c}{\partial t}\Delta x = \left(D\frac{\partial c}{\partial x}\bigg|_{x_o+\Delta x} - D\frac{\partial c}{\partial x}\bigg|_{x_o} \right) \tag{5.4}$$

Next we divide both sides by Δx. Then, recalling that the species flux is given by

$$F = -D\frac{\partial c}{\partial x}, \tag{5.5}$$

we can substitute F into Equation (5.4) to obtain

$$\frac{\partial c}{\partial t} = \frac{F_{in} - F_{out}}{\Delta x}, \tag{5.6}$$

where F_{in} is the flux at x_o and F_{out} is the flux at $x_o + \Delta x$. Here it can be seen that the finite volume method is an application of Gauss's Theorem to a control volume. By tracking species fluxes across the boundaries of the control volume, as demonstrated in Equation (5.6), the finite volume method conserves mass throughout the system.

This integration over the volume can be expanded to other geometries and grid types as well. Consider the spherical coordinate diffusion equation in the radial

direction,

$$\frac{\partial c}{\partial t} = \frac{D}{r^2}\frac{\partial}{\partial r}\left(r^2\frac{\partial c}{\partial r}\right). \tag{5.7}$$

Once again, both sides are integrated over the spatial direction, which in this case is r. First, the r^{-2} term is moved to the time derivative side. The integration becomes

$$\int_{r_o}^{r_o+\Delta r} r^2\frac{\partial c}{\partial t}dr = \int_{x_o}^{x_o+\Delta x} D\frac{\partial}{\partial r}\left(r^2\frac{\partial c}{\partial r}\right)dr. \tag{5.8}$$

The time derivative can be pulled out of the derivative on the left side. Once again the Fundamental Theorem of Calculus is applied to the right side. The integration yields

$$\frac{1}{3}r^3\Big|_{r_o}^{r_o+\Delta r}\frac{\partial c}{\partial t} = \left(r^2\frac{\partial c}{\partial r}\right)\Big|_{r_o}^{r_o+\Delta r}. \tag{5.9}$$

If we multiply the entire equation through by 4π, we recognize that the r^3 term on the left side is a volume and the r^2 term on the right side is an area term. Substituting ΔV in to the equation and simplifying we obtain

$$\frac{\partial c}{\partial t} = \frac{4\pi\left(r^2\frac{\partial c}{\partial r}\big|_{r_o+\Delta r} - r^2\frac{\partial c}{\partial r}\big|_{r_o}\right)}{\Delta V}. \tag{5.10}$$

Once again, we can substitute the flux terms in for the spatial derivatives. Also, the area terms can be substituted. This yields the finite volume equation in the radial direction in spherical coordinates,

$$\frac{\partial c}{\partial t} = \frac{A_{in}F_{in} - A_{out}F_{out}}{\Delta V}. \tag{5.11}$$

This example demonstrates how the finite volume method is capable of conserving mass. The fluxes and respective areas are balanced and scaled by the volume of the discrete element.

5.2 Differential Algebraic Equations

This section, as well as the next section, will loosely follow the work of Ascher and Petzold. [4] The key property of a differential algebraic equation (DAE) is the combination of differential equations and algebraic constraints. These constraints could be a result of physical phenomena (e.g. conservation, continuity, etc.) or additional constraints put on the system (e.g. constant current discharge). The most general form of a DAE is

$$\mathbf{F}(t, \mathbf{y}, \mathbf{y}') = 0, \tag{5.12}$$

where the function $\mathbf{F}$ returns a vector and the inputs are all vectors (denoted by the bold typeface). This form can be broken down into a mass matrix formulation, which is taken as the input for the solver used in this work, `ode15s`. The mass matrix formulation combines the differential and algebraic equations into a single expression,

$$\frac{\partial}{\partial t}\left(\mathbf{M}\mathbf{y}\right) = \mathbf{f}\left(t, \mathbf{y}\right). \tag{5.13}$$

In this equation, $\mathbf{M}$ is a rank 2 tensor. The mass matrix can be a function of time. Furthermore, it can be singular. Here, it will be assumed that the mass matrix is independent of time and can therefore be moved in front of the derivative,

$$\mathbf{M}\frac{\partial \mathbf{y}}{\partial t} = \mathbf{f}\left(t, \mathbf{y}\right). \tag{5.14}$$

This is the form preferred by MATLAB's `ode15s` solver. The solver takes arguments for the mass matrix, right hand side function (shown here as $\mathbf{f}$), and is capable of treating situations where the mass matrix is time dependent and/or singular. The benefit of using a commercial package to solve the equations it that the software is often tested rigorously and contains many additional features, such as adaptive time stepping and error control properties.

However, the disadvantage is that when the solver fails, it's difficult to know why the solver failed. Frequently, it fails due to a mistake in the input. But sometimes, parameter ranges produce errors for unknown reasons, and it may not be entirely clear

how to fix these errors. Additionally, commercial software packages often come with distribution limitations, which could make it difficult to distribute the code to the community. For this reason, it is often better to go with tested open source software that is easily obtainable.

As was stated previously, numerical methods were not the focus of this research. However, their importance cannot be overlooked, especially for the results presented later in this thesis, which will demonstrate behavior not seen before in these types of systems.

5.3 Solving DAE's

One popular discretization method for the time derivative is the Backwards Differentiation Formula (BDF). The BDF method fits a Newton polynomial to previous time steps, then differentiates to obtain the term coefficients. BDF is an implicit multi-step method, in that the next time step appears on both sides of the function. To solve this, Newton's method can be used.

Here we assume a constant mass matrix, and start with Equation (5.14). Let $\mathbf{y}_n$ represent the value we wish to solve for (that is, the values at the next time step). The equation for the kth order BDF is

$$\sum_{i=0}^{k} \alpha_i \mathbf{y}_{n-i} - h\beta_0 f\left(t_n, \mathbf{y}_n\right) = 0, \tag{5.15}$$

where α and β_0 are parameters and h is the time step, Δt. [4] Table 5.1 lists the BDF coefficients for up to sixth order.

Upon closer inspection, it can be seen that first order BDF is the same as the backwards Euler method. The summation term can be separated into two components: the value at the next time step, and the value at previous time steps. Breaking up the summation, Equation 5.15 becomes

$$\mathbf{y}_n + \mathbf{A} - h\beta_0 f\left(t_n, \mathbf{y}_n\right) = 0, \tag{5.16}$$

k	β_0	α_0	α_1	α_2	α_3	α_4	α_5	α_6
1	1	1	-1					
2	$\frac{2}{3}$	1	$-\frac{4}{3}$	$\frac{1}{3}$				
3	$\frac{6}{11}$	1	$-\frac{18}{11}$	$\frac{9}{11}$	$-\frac{2}{11}$			
4	$\frac{12}{25}$	1	$-\frac{48}{25}$	$\frac{36}{25}$	$-\frac{16}{25}$	$\frac{3}{25}$		
5	$\frac{60}{137}$	1	$-\frac{300}{137}$	$\frac{300}{137}$	$-\frac{200}{137}$	$\frac{75}{137}$	$-\frac{12}{137}$	
6	$\frac{60}{147}$	1	$-\frac{360}{147}$	$\frac{450}{147}$	$-\frac{400}{147}$	$\frac{225}{147}$	$-\frac{72}{137}$	$\frac{10}{147}$

Table 5.1: **BDF coefficients** This table lists the BDF coefficients, for up to sixth order (k is the order). This table is adapted from [4].

where

$$\mathbf{A} = \sum_{i=1}^{k} \alpha_i \mathbf{y}_{n-i}. \tag{5.17}$$

This separation demonstrates how the time derivative can be separated into the current value (which is solved for and changes) and the previous time steps (which in the summation) that are constant with respect to time. If we combine the BDF method with the mass matrix DAE formulation in Equation (5.14), we obtain

$$\mathbf{F}\left(t_n, \mathbf{y}_n\right) = \mathbf{M}\left(\mathbf{y}_n + \mathbf{A}\right) - h\beta_0 f\left(t_n, \mathbf{y}_n\right) = 0. \tag{5.18}$$

Next, Newton's method is used to solve this equation for $\mathbf{y}_n$. Newton's method uses a Taylor expansion approximation to iterate towards the roots of the equation. The Taylor expansion is

$$0 = \mathbf{y}_n^{i+1} \approx \mathbf{y}_n^i + \mathbf{J}\left(\mathbf{y}_n^i\right) \Delta \mathbf{y}_n, \tag{5.19}$$

where $\Delta \mathbf{y}_n = \mathbf{y}_n^{i+1} - \mathbf{y}_n^i$, is known as the Newton step. We wish to obtain the root of the function, so the next iteration, $\mathbf{y}_n^{i+1}$, is set to zero. Then, the equation is solved for $\mathbf{y}_n^{i+1}$, yielding

$$\mathbf{y}_n^{i+1} = -\mathbf{J}^{-1}\mathbf{y}_n^i + \mathbf{y}_n^i, \tag{5.20}$$

where the Jacobian, $\mathbf{J}$, is defined as

$$\mathbf{J}_{i,j} = \frac{\partial \mathbf{F}_i}{\partial \mathbf{y}^i_{n,j}}. \tag{5.21}$$

The Jacobian in Equation 5.21 is the derivative of the ith row of the output $\mathbf{F}$ with respect to the jth component of the $\mathbf{y}^i_n$ vector. The Jacobian of the left hand side of Equation (5.18) is

$$\mathbf{J} = \mathbf{M} - h\beta_0 \mathbf{J}_f, \tag{5.22}$$

where $\mathbf{J}_f$ is the Jacobian of the function f, in Equation 5.18. The purpose is to solve for the next value, $\mathbf{y}^{i+1}_n$. This can be accomplished either by inverting the Jacobian (as in Equation 5.20), or using Gaussian elimination on Equation 5.19. This iteration continues until some tolerance is reached, typically when the norm of the function is below some absolute tolerance, a_{tol}, as in

$$||\mathbf{F}\left(t_n, \mathbf{y}^{i+1}_n\right)|| \leq a_{tol}. \tag{5.23}$$

This is one method that can be used to solve the non-linear equation. MATLAB's `ode15s` uses a different implementation. For more on the method used by `ode15s`, the reader is referred to [116]. In the last part of this chapter, an example of the DAE formulation for the case of constant current will be presented.

5.4 DAE Formulation for Constant Current Discharge

To demonstrate the DAE formulation, an example of a half cell discharged at constant current will be presented. For this half cell, the pseudocapacitor approximation is applied, which allows diffusion in the solid particles to be neglected. The solid particles are then replaced by sink terms (i.e. simple time derivatives). The metal potential (ϕ_m) is set to 0 (reference potential) and it is assumed that electron transport is fast

(i.e. no potential drop for the electrons). The dimensionless equations become

$$\epsilon\frac{\partial\tilde{c}}{\partial\tilde{t}} + \epsilon\beta\frac{\partial\tilde{c}_s}{\partial\tilde{t}} = \tilde{\nabla}\cdot\left(\epsilon\tilde{\nabla}\tilde{c}\right), \tag{5.24}$$

$$\frac{\partial\tilde{c}_s}{\partial\tilde{t}} = -2\tilde{i}_o\sinh\left(\frac{\tilde{\eta}}{2}\right), \tag{5.25}$$

$$\epsilon\beta\frac{\partial\tilde{c}_s}{\partial\tilde{t}} = -\tilde{\nabla}\cdot\tilde{\mathbf{i}}. \tag{5.26}$$

This set of equations has three field variables: $\tilde{c}$, $\tilde{c}_s$, and $\tilde{\phi}$, which is inside the equation for $\tilde{\mathbf{i}}$. The spatial derivatives are handled using the finite volume method earlier in this chapter. This DAE formulation focuses more on how to set up the mass matrix.

For this example, a simple 1D grid will be used, consisting of 3 volumes, with 1 in the separator and 2 in the electrode. The anode is not modeled here and is treated as having very fast kinetics. The electrolyte concentration, $\tilde{c}$, and electrolyte potential, $\tilde{\phi}$, exist throughout the separator and electrode, whereas the solid concentration, $\tilde{c}_s$, only exists in the electrode. There are no flux conditions at the end of the electrode and a continuity condition at the electrode/separator interface. The flux of lithium into the separator is set by the constant current (which is set in the simulation). However, the electrolyte potential at the separator/anode boundary is unknown. This value must be set to satisfy the constant current condition,

$$\int_0^1 \frac{\partial\tilde{c}_s}{\partial\tilde{t}}d\tilde{x} = \tilde{I}, \tag{5.27}$$

where $\tilde{I}$ is the constant dimensionless current (defined in Equation 4.53). In this equation, $\tilde{x} = 0$ is the separator-anode interface and $\tilde{x} = 1$ is the cathode-current collector interface.

Combining everything, there are 9 total variables: 3 field values of $\tilde{c}$, 3 field values of $\tilde{\phi}$, 2 field values of $\tilde{c}_s$, and the potential boundary condition, $\tilde{\phi}_o$. The mass matrix has 81 values (most of them are 0). Rewriting Equations (5.24), (5.25), and (5.26) into the form of Equation (5.14) becomes

$$\begin{bmatrix} \epsilon & - & - & - & - & - & - & - & - \\ - & \epsilon & - & - & - & - & \epsilon\beta & - & - \\ - & - & \epsilon & - & - & - & - & \epsilon\beta & - \\ - & - & - & - & - & - & - & - & - \\ - & - & - & - & - & - & \epsilon\beta & - & - \\ - & - & - & - & - & - & - & \epsilon\beta & - \\ - & - & - & - & - & - & 1 & - & - \\ - & - & - & - & - & - & - & 1 & - \\ - & - & - & - & - & - & \Delta\tilde{x} & \Delta\tilde{x} & - \end{bmatrix} \frac{\partial}{\partial \tilde{t}} \begin{bmatrix} \tilde{c}_1 \\ \tilde{c}_2 \\ \tilde{c}_3 \\ \tilde{\phi}_1 \\ \tilde{\phi}_2 \\ \tilde{\phi}_3 \\ \tilde{c}_{s,1} \\ \tilde{c}_{s,2} \\ \tilde{\phi}_0 \end{bmatrix} = \begin{bmatrix} \tilde{\nabla} \cdot \left(\epsilon \tilde{\nabla} \tilde{c}\right) \\ \tilde{\nabla} \cdot \left(\epsilon \tilde{\nabla} \tilde{c}\right) \\ \tilde{\nabla} \cdot \left(\epsilon \tilde{\nabla} \tilde{c}\right) \\ -\tilde{\nabla} \cdot \left(\tilde{\mathbf{i}}\right) \\ -\tilde{\nabla} \cdot \left(\tilde{\mathbf{i}}\right) \\ -\tilde{\nabla} \cdot \left(\tilde{\mathbf{i}}\right) \\ -2\tilde{i}_o \sinh\left(\frac{\tilde{\eta}}{2}\right) \\ -2\tilde{i}_o \sinh\left(\frac{\tilde{\eta}}{2}\right) \\ \tilde{I} \end{bmatrix}. \tag{5.28}$$

The equations on the right hand side should be discretized and represented using the aforementioned finite volume method. The value for ϕ_0 is the boundary condition at the separator side. It is important to recognize that the mass matrix (the 9x9 matrix on the left) is singular. Furthermore, there are no time derivatives for the potential conditions. These are the algebraic constraints set by the charge conservation. Additionally, the DAE controls the boundary condition via the constant current condition (the last row). This equation can be formulated as Equation (5.18) and solved via Newton's Method.

5.5 Conclusion

The purpose of this chapter was to prevent a brief overview of DAE's as they apply to porous electrode theory and demonstrate how to formulate the set of equations as a DAE. For the case of solid diffusion, then the solid concentration values in Equation (5.28) should be replaced by the solid concentration inside the particles and the reaction rate becomes the flux into the particles at the solid-electrolyte interface.

There are many different software packages available to solve DAE's. This work uses MATLAB's `ode15s` because of its ease of use and robustness. Another good

solver to use is Assimulo in Python, which uses the Sundials (`https://computation.llnl.gov/casc/sundials/main.html`) solver IDA. In the next chapter, some example simulations will be presented. Later in this thesis, simulations will be compared to experiment.

Chapter 6

Simulations

This chapter will present some example constant current simulations of the MPET equations using the aforementioned `ode15s`. First, the case of homogeneous particles will be considered. Various effects will be demonstrated including changing the discharge rate, changing the exchange current density, and changing the solid diffusivity.

Additionally, phase separating particles will be considered. These particles will be modeled in the surface reaction limit (SRL), allowing the depth concentration to be neglected. The Cahn-Hilliard free energy functional will be used to model the particles and stress effects will be considered. However, other important effects such as surface wetting will not be considered in this section. For the case of no stress and coherency strain, changes in the discharge rate will be demonstrated.

The values given in the simulation are dimensionless. Chapter 4 gives the scalings for each of the values. Approximate dimensional values will be given in this chapter as well to denote what regime the cell is in (e.g. fast/slow discharge). The figures and results here are adapted from Ferguson and Bazant. [58]

6.1 Homogeneous Particles

The main features that will be investigated in this section are the discharge rate, the exchange current density, and the solid diffusivity. The exchange current density is a parameter that is often very difficult to accurately model. Many assumptions about

the reaction rate (i.e. the reaction steps and rate constants) are required. In phase separating materials, where not all of the material's surface area is necessarily active, this can be even more difficult.

Prior to showing simulation results, it's important to denote the axes used in the figures. For the case of a 1D half cell, there are two directions lithium can diffuse in: the depth direction into the electrode, and into the particles. These two axes are combined into a signal contour plot which denotes the lithium concentration inside the solid particles as well as the particles location inside the electrode. Figure 6-1 denotes the axes used in the homogeneous particle simulations.

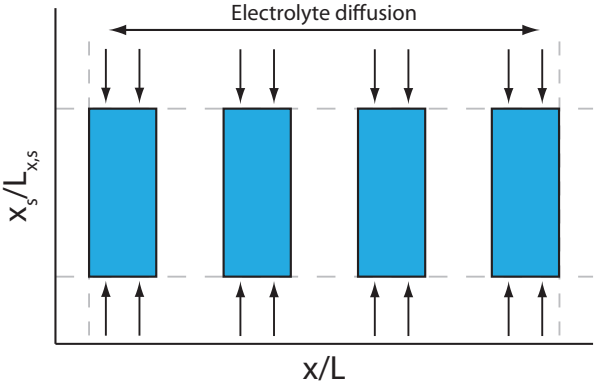

Figure 6-1: **Plot axes for diffusion-limited solid-solution particles**. This figure shows how the simulation results below are plotted for porous electrodes with isotropic solid solution particles. The y-axis of the contour plots represent the depth of the particles while the x-axis represents the depth into the electrode. The particles are modeled in 1D.

For these simulations of homogeneous particles, a porosity of 0.4 was used. The dimensionless parameter $\epsilon\beta$ was set to 22.8, which is a little larger than typical electrodes, and is used to demonstrate electrolyte depletion. The volume percent of active material was set to 0.7. This results in a max concentration of 54 M lithium in the solid.

Ion diffusivities in the electrolyte were considered constant and taken from Valoen and Reimers [136]. The cation diffusivity was set to 1.25e-10 m^2/s and the anion diffusivity was 4e-10 m^2/s, which results in an ambipolar diffusivity of 1.9e-10 m^2/s. The electrode length was 50 μm and the particles were plate-like particles that are 50

nm x 200 nm x 100 nm thick (half of this was modeled, and a symmetry boundary condition is used at the center), with the top and bottom as active surfaces. The charge transfer coefficient is set to 0.5. The separator is assumed to be 25 μm thick. The electrode is discretized into 20 volumes and the separator is discretized into 10 volumes. The solid particles were discretized into 50 volumes. The dimensionless exchange current density was 0.01, which corresponds to a dimensional exchange current density of approximately 0.2 A/m^2.

The first simulation demonstrates the effect of increasing the current. In these particles, the ratio of diffusive times, δ_d, is given by Equation 4.61. It is set to one in this simulation so that solid diffusion has the same diffusive time as the electrode. This gives fast diffusion in the solid. The result is that the voltage dropoff is caused by an electrolyte limitation. Figure 6-2 shows the voltage diagrams and solid concentration profiles for different discharge rates.

A dimensionless current of 0.001 is equivalent to a dimensional discharge rate of approximately C/3. The other dimensionless current values of 0.01 and 0.05 are approximately 3C and 15C, respectively. The red dots on the voltage curves correspond to the solid concentration profiles, from top to bottom, left to right in the figures below. At the slowest discharge rate, the particles fill homogeneously throughout the electrode. As the current is increased, it can be seen that particles closer to the separator (on the left) have a higher lithium concentration than particles deeper in the electrode. At the fastest discharge rate, there is a large difference between particles next to the separator and particles deeper in the electrode. The voltage drop-off in the fastest discharge curve is actually due to an electrolyte transport limitation. Figure 6-3 demonstrates this depletion.

Figure 6-3 shows the voltage curve for the 15C discharge in figure 6-2. The three dots correspond to the diagrams below which show the solid concentration profiles throughout the electrode (left) and the electrolyte concentration (right), including the separator (note: the discontinuity is the separator/electrode interface and the slope change is the result of a porosity change). The figures show how the electrolyte depletes, resulting in increased overpotential. This proceeds until the electrolyte is

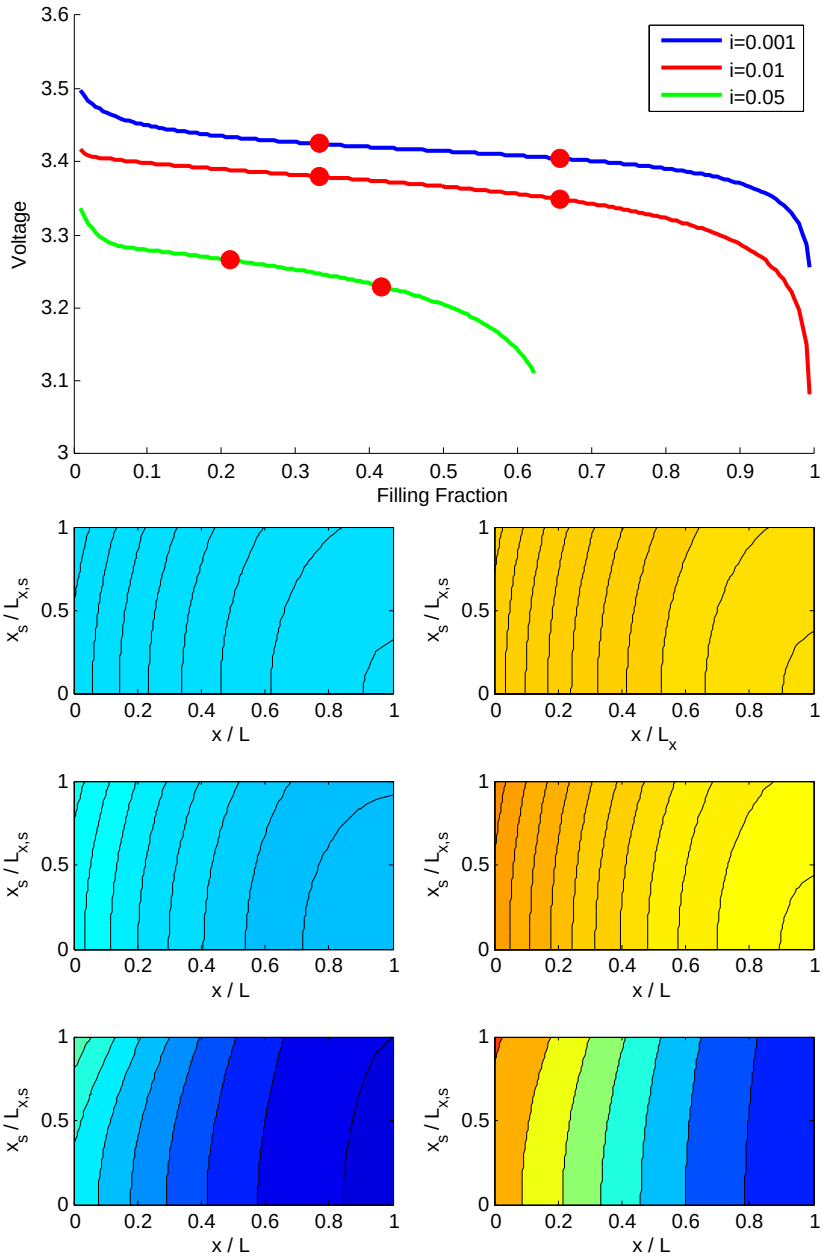

Figure 6-2: **Effect of current on homogeneous particles**. This figure demonstrates the effect of different discharge rates on the voltage profile. The non-dimensional currents correspond to roughly C/3, 3C, and 15C. The solid diffusion is fast, with $\delta_d = 1$.

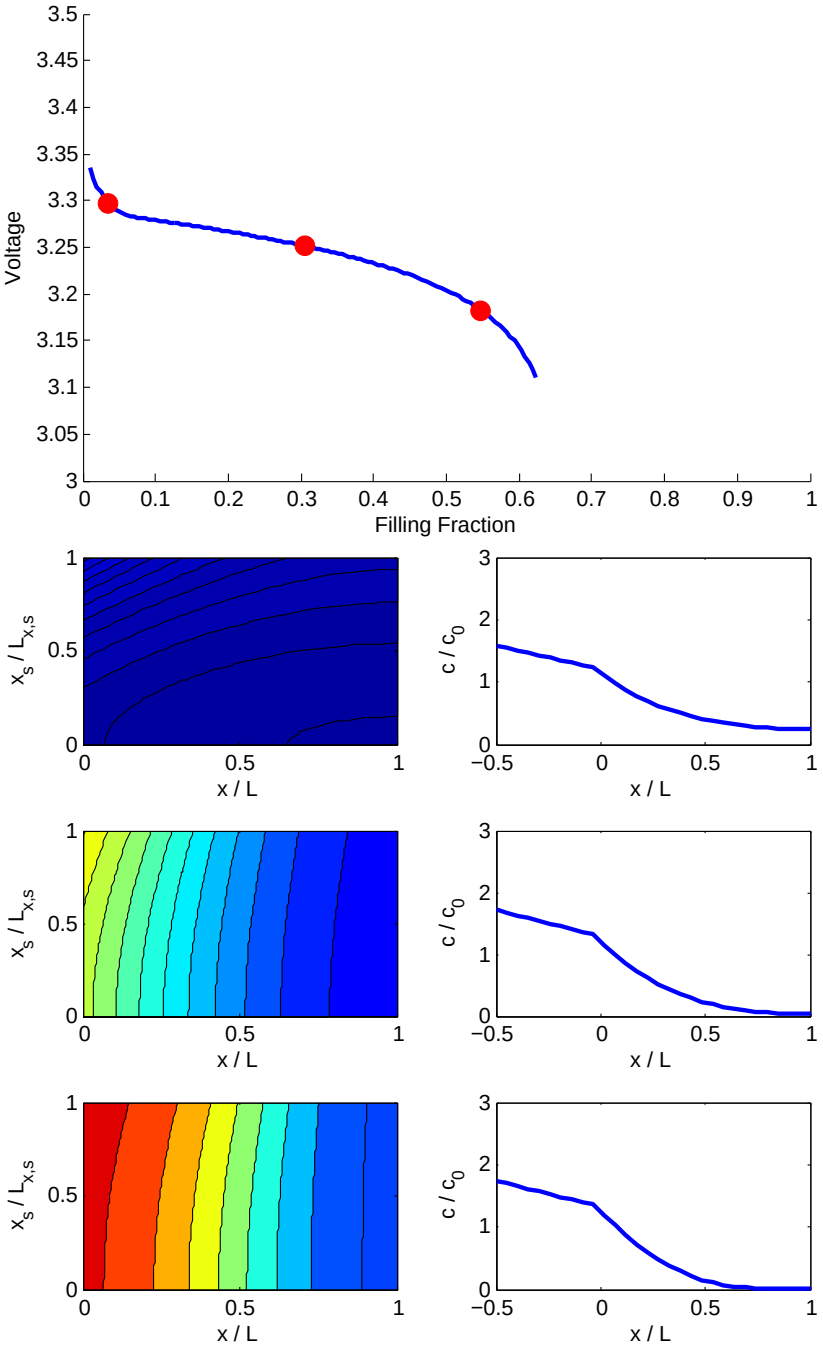

Figure 6-3: **Depletion of the electrolyte at higher current**. This figure shows the depletion of the electrolyte accompanying Figure 6-2 for the 15C discharge. The left figure shows the solid concentration while the right figure demonstrates the electrolyte concentration profile in the separator and electrode.

completely depleted, at which point the constant current can longer be sustained, leading to a sharp drop off in potential.

Next, the effect of slower solid diffusion is considered. To control solid diffusion, the value of δ_d is varied. This parameter is the ratio of the diffusive time of the solid to that of the electrolyte (given by Equation 4.61). Typically, this value is larger than one, but it scales with the solid diffusivity (a material property) and the particle size. The solid diffusivity usually needs to be fit. Figure 6-4 demonstrates the effect of increasing current on particles with slower solid diffusion. The δ_d value has been changed from 1 to 100, meaning the solid diffusion time (L_s^2/D_s) is 100 times larger than the electrolyte diffusive time (L^2/D_{amb}). This leads to a solid transport limitation, causing lithium to build at the surface of the particles, leading to increased overpotential.

Figure 6-4 shows the same discharge rates as Figure 6-2 but with slower solid diffusion. The three red dots correspond to the solid concentration profiles below, left to right, top to bottom. At C/3 discharge ($\tilde{I} = 0.001$), the particles fill homogeneously throughout the electrode. As the current is increased to 3C, the particles start to exhibit concentration gradients throughout the electrode. Eventually, high concentrations at the surface of the particles lead to increased overpotential and a voltage dropoff around half filling. At 15C, this effect is even more pronounced, leading to a sharp voltage dropoff near 10% filling. This figure demonstrates the model's sensitivity to solid diffusivity and demonstrates how reduced solid transport affects the cell voltage.

Next, the effect of solid diffusivity will be demonstrated for a single current. Figure 6-5 demonstrates the effect of solid diffusivity at a discharge rate of 3C. Here the effect of decreasing the solid diffusivity is much more pronounced. By increasing the value of δ_d from 1 to 100, half the capacity of the cell is lost. This change in δ_d corresponds a solid diffusion pathway that is 10 times longer, or a solid diffusivity that is reduced by a factor of 100. Even a value of $\delta_d = 50$, which represents a solid diffusion pathway approximately 7 times longer, or a solid diffusivity that is reduced by a factor of 50, shows a decrease of 20% capacity.

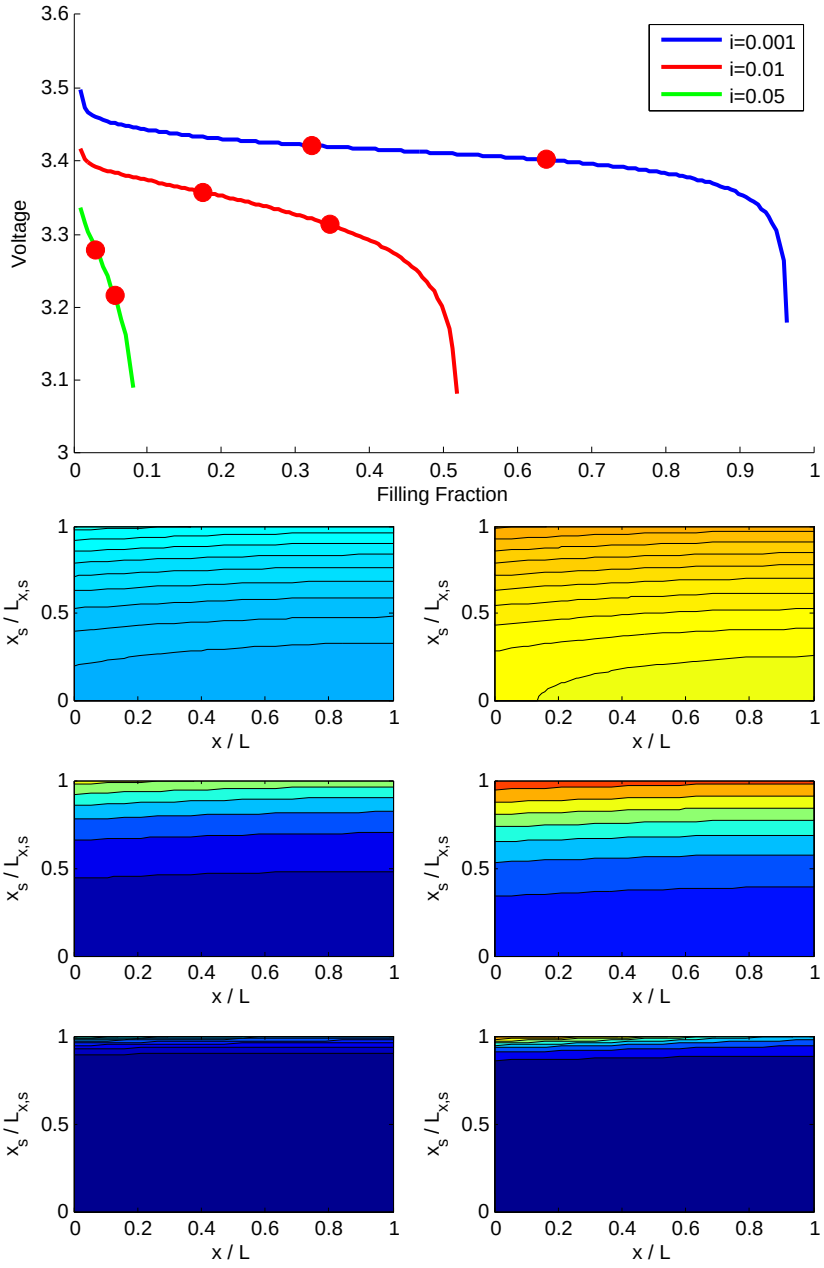

Figure 6-4: **Effect of current on homogeneous particles with slower solid diffusion**. This figure demonstrates the effect of different discharge rates on the voltage profile. The non-dimensional currents correspond to roughly C/3, 3C, and 15C. The solid diffusion is slower than the electrolyte diffusion ($\delta_d = 100$).

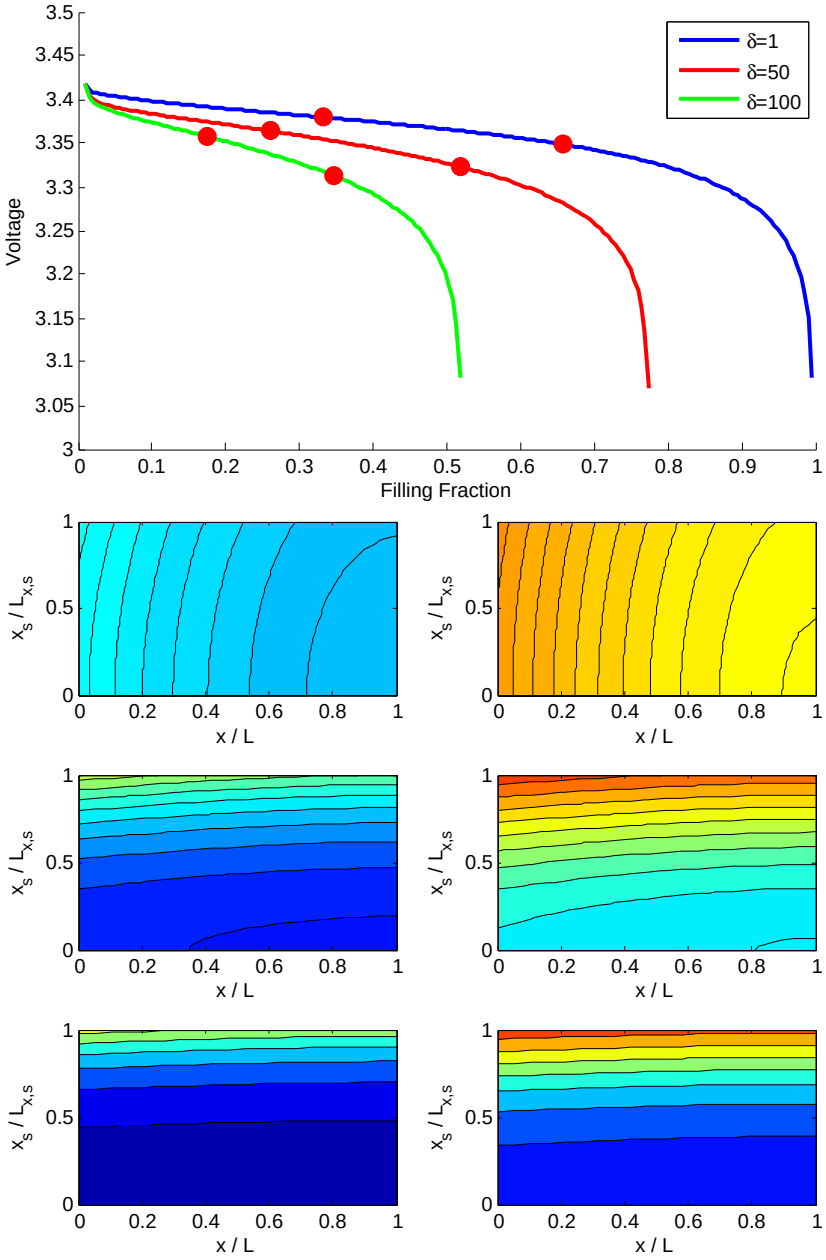

Figure 6-5: **Effect of solid diffusivity on homogeneous particles**. This figure demonstrates the effect of decreasing solid diffusivity on the voltage profile. Each of these simulations was run at a dimensionless exchange current density of 0.01 and a dimensionless current of 0.01.

This section provided examples of homogeneous particle behavior with different discharge rates and solid diffusivity values. The next section will cover phase separating particles.

6.2 Phase Separating Particles

The model presented here inside the MPET framework is the surface reaction limited (SRL) model first presented by Bai *et al.*. [8] This model was applied to lithium iron phosphate (LFP) particles. While the simulations presented here are similar, different values were used for the gradient penalty, κ. Additionally, coherency strain will be approximated later in the section. These results are not intended to accurately capture the behavior of LFP in a porous electrode.

Accurately modeling LFP requires additional effects, including surface wetting and particle size effects. [45, 44] Also, since LFP is not a good electrical conductor, electron transport in the porous media, and possibly even the carbon coating of the individual nanoparticles, could play an important role. In the next chapter, a model based on these effects to describe the small current voltage gap observed in LFP electrodes will be presented and compared to data. [54] For now, though, the simplified case will be presented to demonstrate the model's ability to use phase field models to model phase separating materials.

Figure 6-6 shows how the solid concentration data is presented in this section. In the previous section, the y-axis denoted the particle's solid concentration in the depth direction. In this section, it is assumed that the depth direction has fast diffusion, allowing the particles to be depth averaged. [96] The y-axis in the contour plots shown display the solid concentration across the surface of the particles. The x-axis, as before, shows the particle's location relative to the separator.

The same electrolyte transport properties were used as for the homogeneous particles. The length of the electrode was 50 μm, with a separator length of 25 μm. The value of $\epsilon\beta$ was 24. The particle dimensions were assumed to be 50 nm x 50 nm x 30 nm (30 nm is the depth), with one active surface. A dimensionless exchange current

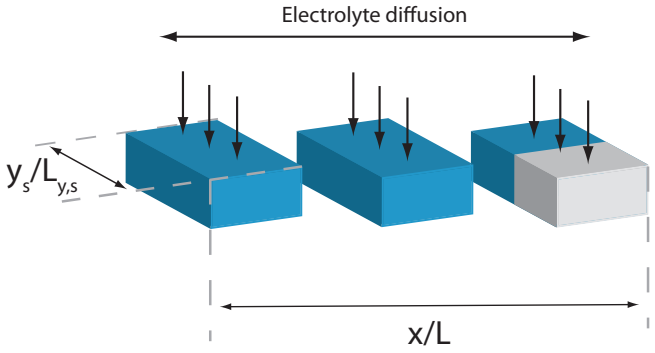

Figure 6-6: **Plot axes for reaction-limited phase separating particles**. This figure shows how the results are plotted below for porous electrodes with reaction-limited phase separating nanoparticles. The y-axis of the contour plots represent the length along the surface of the particle, since diffusion is assumed to be fast in the depth direction. The x-axis represents the depth in the electrode.

density of 0.1 was used, which corresponds to an exchange current density of approximately 1.25 A/m^2. The value of the dimensionless gradient penalty, $\tilde{\kappa} = \kappa/k_B T \rho_s L_s^2$, was 0.001. For the case of an approximated bulk coherency strain, the dimensionless parameter $\tilde{b} = b/k_B T \rho_s$, was set to 1.6. The porosity was set to 0.4.

Three results will be presented to demonstrate the effect of increasing the discharge rate and adding coherency strain. First, a slow discharge curve is presented (C/30). Then an approximate coherency strain term is added. This term suppresses phase separation. Finally, the effect of increasing the discharge rate is demonstrated.

Figure 6-7 shows the effect of slowly discharging the phase separating particles. The discharge rate corresponds to approximately C/30. While a single particle would have a strong tendency to phase separate at this discharge rate, a porous electrode of these particles (all uniform in size) does not exhibit the same behavior. Instead, a sharp front emerges that separates filled and empty particles, and the particles undergoing lithiation fill quickly and homogeneously. It is not until the end of the simulation, where single particle behavior becomes more evident (since the number of remaining particles is small), that phase separation occurs.

One way to explain this is that the local current density is actually much larger than the total current of the cell. Bai *et al.* demonstrated that for single particles

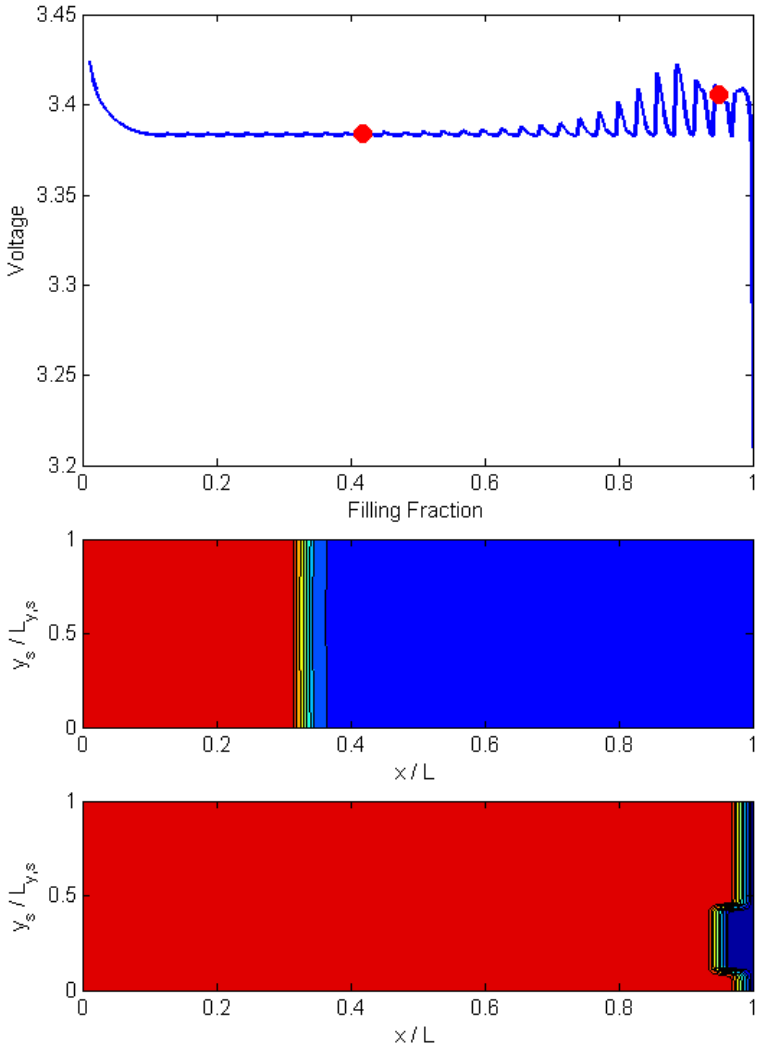

Figure 6-7: **Phase separating particles slowly discharged**. This figure shows slow discharge (approx. C/30) of phase separating particles. Adequate electrolyte diffusion and discrete filling don't allow time for the particles to phase separate early on. At the end of the discharge, sufficient time allows the particles to phase separate.

(using the same model here), if the local current density is much less than the exchange current density, phase separation occurs. [8] While the total current (i.e. the integral of the reaction rate over all the particles) is less than the exchange current density, the local current density shown here is not. This leads to particles filling homogeneously and discretely.

Not only do the particles at the front fill discretely, but low concentration particles actually delithiate while these particles are filling. This is due to the non-monotonic shape of the open circuit voltage profile of the material when it behaves homogeneously. The particle voltage oscillates between the miscibility and spinodal concentrations. The flat voltage plateau produced in the figure is the result of the difference between the miscibility voltage and spinodal voltage. There is a finite overpotential that is required before the particles can be lithiated. On lithiation, there is also a finite overpotential required to drive lithiation. In the limit of zero current, this produces a "voltage gap", which was explained by Dreyer *et al.*. [54] This simulation demonstrates the importance of particle-particle effects in the cell.

It was later shown by Cogswell and Bazant that coherency strain on lithiation can further suppress the phase separation of these particles. [45] To simulate this system, an additional coherency strain energy penalty was included. This additional term penalizes deviations from the particles average concentration, which promotes homogeneous filling. Figure 6-8 demonstrates the effect of this additional energy penalty. At the same C/30 discharge rate, this additional penalty term further suppresses phase separation in the particles, and all particles fill homogeneously throughout the electrode.

Another effect to be demonstrated is the current induced suppression of phase transformation at the porous electrode scale. This idea was first introduced by Bai *et al.*. It was shown that as current is increased for a single particle, phase separation is suppressed, leading to homogeneous filling. [8] Interestingly enough, a similar effect can be seen on the porous electrode scale. If we consider discrete filling to be similar to phase separation (i.e. when particles fill discretely, it's similar to having lithiated and delithiated regions with an active region between them), then the same effect is

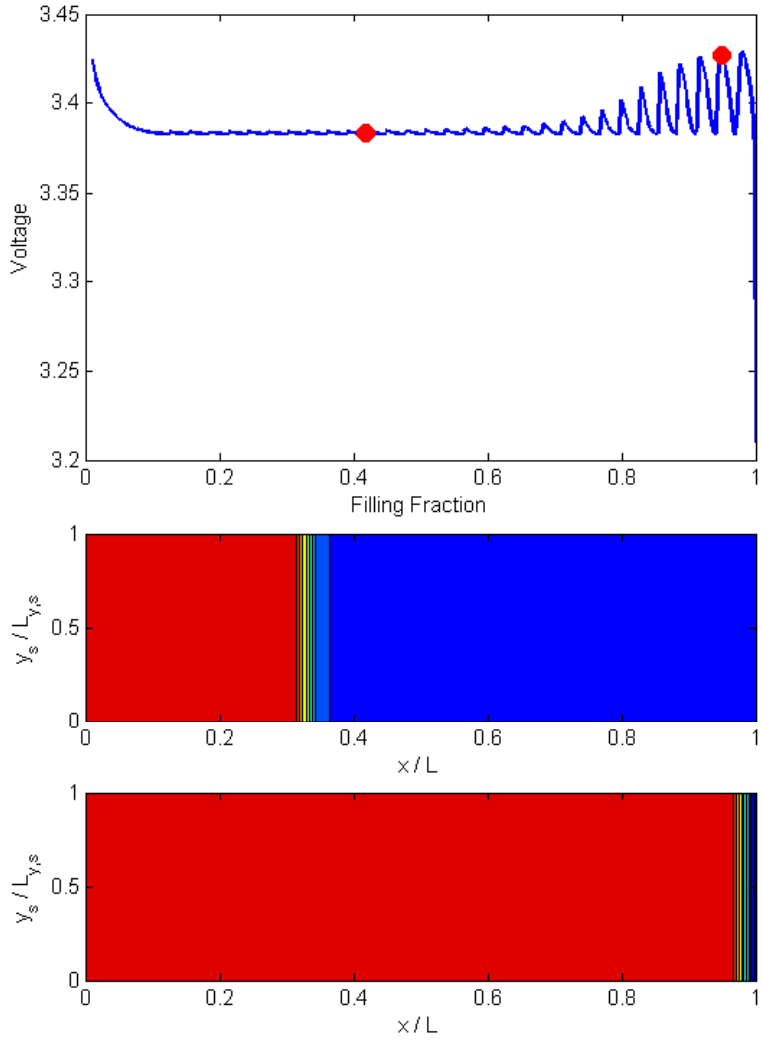

Figure 6-8: **Phase separating particles including coherent stress effects slowly discharged**. This figure shows slowly discharge (approx. C/30) phase separating particles. The inclusion of the coherent stress effects suppresses phase separation inside the particles. This figure is the same as Figure 6-7, with an additional coherent stress term.

observed on the electrode scale. As the discharge rate is increased, the number of active particles in the electrode increases. This number increases until all the particles in the electrode are active, at which point the electrode fills homogeneously.

Interestingly enough, this occurs when the dimensionless current is roughly on the order of the dimensionless exchange current, which is similar to the results observed by Bai *et al.*. [8] Figure 6-9 shows discharge at a dimensionless current of 0.01, which is approximately 3C. The increased discharge rate increases the number of active particles, and instead of discrete filling of individual particles, discrete filling of clusters of particles is observed. The number of particles increases until the entire electrode fills homogeneously. This behavior is very different from the slow discharge case. This effect can be described with an equivalent circuit model.

Figure 6-10 shows an equivalent circuit for the porous electrode. Each particle can be characterized using a representative time scale for charge/discharge. This time scale, t_c, can be expressed as

$$t_c \sim R_{ct} C_p, \tag{6.1}$$

where R_{ct} is non-linear charge transfer resistance, and C_p is the non-linear capacitance. These values are non-linear, as they will vary based on filling, location, and other particle properties. The number of active particles, n_{ap}, should scale with the dimensionless current,

$$n_{ap} \sim t_c \tilde{I}. \tag{6.2}$$

As the discharge rate is increased, the number of active particles scales as well. For fast kinetics (or slow discharge rates), the number of active particles is small, leading to discrete filling of the particles. Slower kinetics (or fast discharge rates) requires more active particles to sustain the discharge rate, leading to a larger number of active particles.

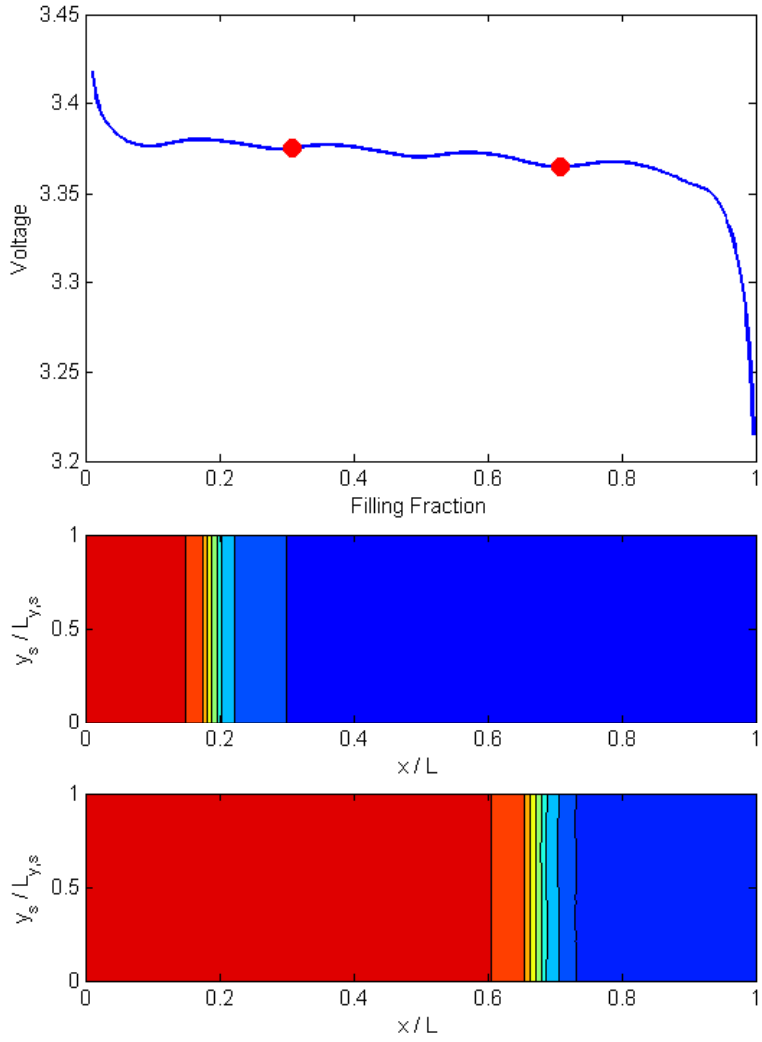

Figure 6-9: **Effect of current on phase separating particles**. When discharged at a higher C-rate (in this example, 3C), the size of the discrete particle filling is larger, leading to more particles filling simultaneously and a voltage curve that resembles solid solution behavior.

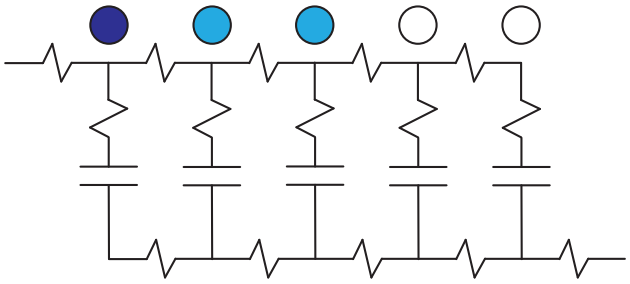

Figure 6-10: **Equivalent circuit model for a porous electrode**. This equivalent circuit represents a typical porous electrode in cases without significant electrolyte depletion, where the pore phase maintains nearly uniform conductivity. Resistors represent the contact, transport, and charge transfer resistances, and the capacitance of the particles is represented by a capacitor. All elements are not necessarily linear.

6.3 Conclusion

These results demonstrate the behavior of the model for phase separating and homogeneous solid materials in the porous electrode. For homogeneous materials, the discharge is sensitive to solid diffusivity and concentration gradients inside the particles can lead to large overpotentials. The simulations also demonstrated the effect of increasing the discharge rate and depleting the electrolyte. The simulations of phase separating materials demonstrated the effect of the current on how the electrode fills. They also showed how coherency strain inside these phase separating particles can suppress phase separating. While this is the case for uniform electrodes (i.e. all particles have the same shape/size), results in the next two chapters will demonstrate how particle size can break this symmetry, leading to preferential filling of particles deeper in the electrode.

For application to real phase separating systems, such as $LiFePO_4$, more complicated models of the solid material are required. Recent work by Cogswell and Bazant demonstrated that surface wetting and coherency strain can play a large role in the overpotential required to lithiate LFP particles. [44] They found that the side facets of LFP energetically prefer to be wetted (i.e. lithiated). The ratio of the wetted surface area to the volume of the particle, combined with coherency strain, causes smaller particles to preferentially fill. This model will be incorporated into the MPET

framework later in this thesis and qualitatively compared with experiments.

In the next chapter, comparison with experiments will be presented. First, an LFP electrode will be simulated using a simplified form of Cogswell and Bazant's model along with the MPET framework to fit the small current voltage gap experiments by Dreyer *et al.*. [54] The model demonstrates the importance of size effects in the electrode. Additionally, a new graphite model will be presented and used to fit the experiments of Harris *et al.*. [67] Harris "unrolled" a graphite electrode and put a glass slide on top to observe the color change associated with lithiation of the graphite. The free energy model, along with MPET, are used to fit the observed color profiles.

Chapter 7

Modeling Phase Separating Materials

In this chapter, the Modified Porous Electrode Theory framework is applied to two representative porous electrode experiments: (i) surface reaction-limited intercalation in LFP, and (ii) electrolyte-diffusion limited intercalation in graphite. The analysis is based on a general Cahn-Hilliard phase-field porous electrode model, as presented in this thesis. Although the conclusions also follow from the full model, simulations and analysis of the "pseudocapacitor" limit of homogeneous intercalation in each particle are presented. This limit can be caused by fast diffusion and/or suppressed phase separation compared to experimental time scales.

7.1 Reaction-Limited Dynamics with Two Phases

This section builds on the work of Cogswell and Bazant, which showed that surface wetted nucleation combined with coherency strain (SWCS) reproduces many of the phenomena observed in LFP nanoparticles. [44] While this model addresses many of the interesting particle scale effects, many questions remain about dynamics at the scale of the porous electrode. The SWCS model is very computationally expensive. To explore the effects of hundreds of these particles inside a porous electrode, reduction of the model is necessary so that simulations can be run on a reasonable time scale

in order to fit parameters.

Previous work in this thesis has demonstrated that non-monotonic open circuit potential profiles produce very large local current densities, suppressing phase separation. Including coherency strain further suppresses this phase separation, causing particles to fill discretely and homogeneously when the electrode is discharged slowly. This is advantageous, since homogeneous filling does not require phase field models.

Cogswell demonstrated that single particle voltage profiles are always tilted due to coherency strain and that the overshoot from the standard potential on discharge varies with particle size (this effect will be explored in the next chapter of this thesis). This overshoot, which can be thought of as the half gap (i.e. the overpotential required to drive lithiation), depends on particle size since the surface wetting represents a larger percentage of the total volume for smaller particles.

One interesting property of the regular solution model (given by Equation 4.41) is that the regular solution parameter controls the overshoot (i.e. the non-monotonicity) of the chemical potential. At $\Omega = 2k_BT$, the regular solution model chemical potential has a flat region in the center. As Ω is increased, the spinodal points move towards the $x = 0$ and $x = 1$ axes and the chemical potential of the spinodal moves away from the $\mu = 0$ line. The voltage gap for the regular solution model can be solved analytically and is given by

$$\Delta V_{gap} = \frac{2k_BT}{e}\left[\sqrt{\tilde{\Omega}^2 - 2\tilde{\Omega}} - 2\tanh^{-1}\left(\sqrt{1-\frac{2}{\tilde{\Omega}}}\right)\right]. \tag{7.1}$$

Using this property of the regular solution model, the SWCS model is reduced by fitting an effective regular solution parameter to the voltage half gap from Cogswell and Bazant based on the particle's wetted area to volume ratio.

Figure 7-1a shows a plot of the half gap from Cogswell and Bazant (in blue) along with the corresponding effective regular solution parameter. The effective regular solution parameter is the value that corresponds to an equivalent overshoot on discharge. It is important to note that Cogswell and Bazant only modeled the half gap on discharge. Here, we assume that the voltage gap on charge and discharge are

the same. Figure 7-1b demonstrates representative open circuit potential profiles for different sized particles.

This reduction of the SWCS model allows multiparticle simulations to be performed using the MPET framework. The experimental work that will be focused on here is the work of Dreyer *et al.*, which observed a non-zero voltage gap in the limit of zero current. [54] The paper showed a voltage gap of 20 mV remained at charge/discharge rates of $\pm$C/1000. The benefit of this experiment is its extremely slow charge and discharge rate, which allows particle-particle interactions to be examined without the effects of transport limitation or high overpotentials.

The work of Dreyer *et al.* represents one of the first major steps towards understanding the lithiation dynamics of an LFP electrode. The authors suggested that the non-monotonic open circuit potential profile was the source of the voltage gap. However, a regression with thermodynamic data by Cogswell and Bazant suggests that the equilibrium voltage gap in homogeneous particles is on the order of 74 mV. [45] Cogswell and Bazant went on to predict that the discrepancy in the voltage gap is caused by the wetted area to volume ratio, which depends on particle size. Using the reduced SWCS model along with MPET, the model is capable of reproducing the voltage curves as well as the voltage gap with only three fitting parameters: average particle size, particle size variance, and a constant contact resistance.

Given the slow charge/discharge rates, electrolyte properties are not very important since the electrolyte does not deplete. For completeness, however, suitable numbers were chosen for transport properties. An ambipolar diffusivity of $1.5\text{x}10^{10}\text{m}^2/\text{s}$ was used for the 1M $LiPF_6$ in EC/DEC electrolyte. [125] A transference number could not be found for this electrolyte, so a value of 0.35 was assumed, which is in line with other typical battery electrolytes. [1] The electrode was assumed to be 50 μm long with a 25 μm separator. The volume fraction of the active material was assumed to be 0.5, and the porosity was 0.4. It is important to iterate that at such slow charge/discharge rates, there is no electrolyte depletion and these values have little to no effect on the simulations.

Calculation of the particle size was performed using a random normal distribution.

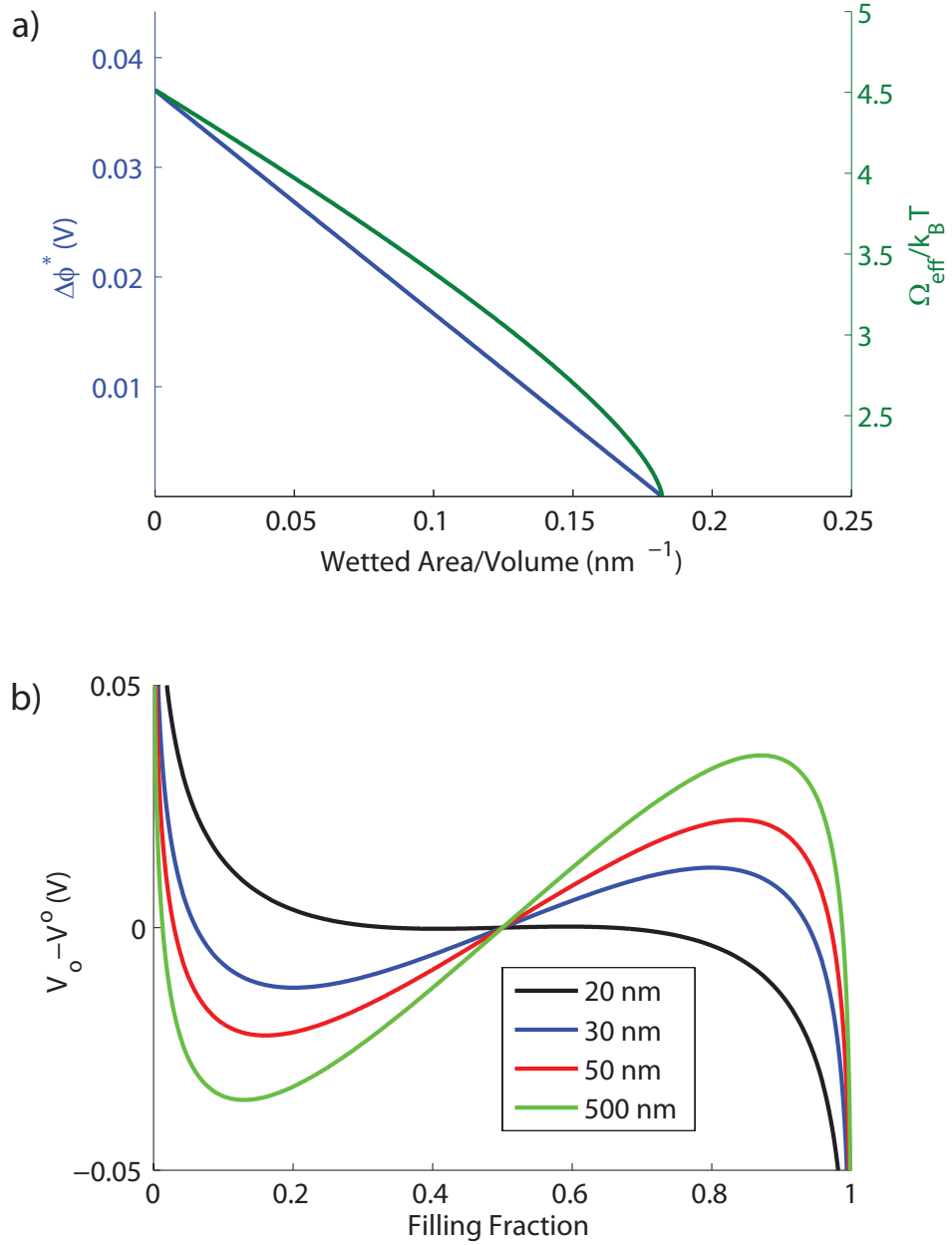

Figure 7-1: **Voltage half gap and effective regular solution**. Figure a denotes the voltage half gap on discharge from Cogswell and Bazant and the resulting effective regular solution parameter as a function of the wetted area to volume ratio. Figure b demonstrates various effective open circuit potential profiles for different sized particles.

The particle shapes were assumed to be the C3 shape from Cogswell and Bazant. [44] This shape was derived from Smith *et al.*. [121] The particles were assumed to be 20 nm thick. [121, 115] Calculation of the wetted surface area to volume ratio was calculated via $A/V = 3.6338/d$, where d is the size of the particle in the [100] direction. [44] The exchange current density used in the simulation was 1.5 A/m^2. The actual value of this parameter should not be taken literally, as will be explained later. A normal distribution was used to generate the particle sizes.

The simulation was run by starting with a fully charged electrode, which was then discharged to a filling fraction of 0.2 at a C/10 rate. The electrode was then relaxed by simulating a zero current for a long period of time (roughly 3.5 hours in dimensional time). The electrode was then discharged to a filling fraction of 0.7, relaxed, then charged back to 0.2. When calculating the voltage gaps, the data were smoothed (since discrete particle filling makes the data very noisy, although the fluctuations are very small) to make the value consistent. A constant contact resistance was used to fit the data. A value of 3.9 Ω·g was found to fit the data the best.

Figure 7-2 compares simulation results with the data from Dreyer *et al.*. Figure 7-2a overlays the voltage data on the simulation data for discharge rates of C/1000, C/200, and C/131. The simulation filling range was extended due to start up effects from the discreteness of the model. The model shows good agreement with the discharge voltage data, even matching the slope of the voltage curves. On charging, however, the agreement is not as good. While the model predicts more symmetric behavior on charge and discharge, the experimental data shows overlapping between the C/200 and C/131 charging data.

An important parameter in the simulation to mention is the exchange current density. The exchange current density used in the simulation is 1.5 A/m^2. While this value seems very high compared to other values in simulations, the difference is that this value is per *active* area. Determining the active area in a real system is very difficult unless a single particle is discharged. Given the discrete nature of the model, the active area is a very small fraction of the entire electrode. Other simulations, such as traditional porous electrode theory, assume the entire electrode is active, and

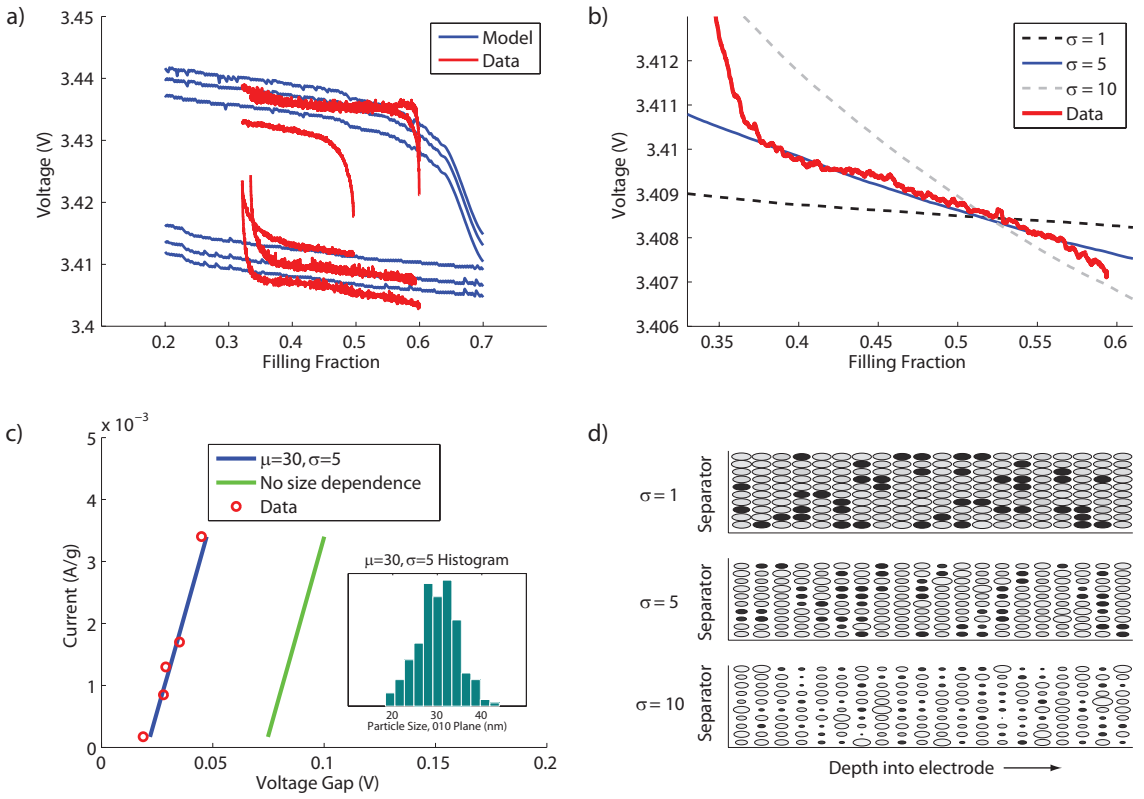

Figure 7-2: **Voltage gap fit to data**. This figure shows the fit of the model to experimental data from Dreyer *et al.* [54] Figure (a) shows an overlay of the simulation with the data for C/1000, C/200, and C/131. Figure (b) shows the effect of particle size variance on the voltage curve. Figure (c) compares the voltage gap to data with the additional C/100 and C/50 rates. Also the voltage gap with no size effect is demonstrated. The inlay shows the particle size distribution used to fit the data. Figure (d) shows representative particle sizes for the variances given in figure (b) at a filling fraction of 0.5. Experimental data in figures (a-c) from [54], provided courtesy of Miran Gaberšček

therefore treat the entire electrode area in the exchange current. This can produce a large difference in the exchange current density, on the order of many orders of magnitude. For example, values from Srinivasan and Newman [123] indicate a total electrode area of approximately 0.1 m^2, compared to these simulations, which predict an active area on the order of 0.0004 m^2 (for 30 nm C3 shaped particles).

The actual value of the exchange current density is not important as long as the value remains larger than the local current density. When the local current density is less than the exchange current density, a particle-by-particle effect is observed which

leads to the voltage profiles shown in Figure 7-1. When the exchange current density is less than or on the order of the local current density, then multiple particles (or clusters of particles) are required to satisfy the current, and the electrode fills more homogeneously. Therefore, the value used should not be taken as a literal value, since a range of values will satisfy this condition.

One unexpected finding of this simulation was the effect of the particle size variance on the voltage. Figure 7-2b shows the effect of the particle size variance. As the variance increases, the slope of the voltage curve increases. This is due to change in active particle size as the electrode is discharged. For a single particle size, the voltage gap is the same for all particles, leading to a flat voltage profile. However, as the variance in particle size increases, the voltage gap for different particles is no longer the same, and slow discharge results in filling small particles (i.e. particles with a smaller voltage gap) followed by larger particles (i.e. particles with a larger voltage gap). This sequential filling tilts the voltage plateau very slightly (on the order of millivolts) leading to small particles filling preferentially followed by larger particles.

Figure 7-2c shows a comparison between the voltage gap for more charge/discharge rates. The particle size used to fit the voltage gap is 30 nm (in the 100 direction) with a standard deviation of 5 nm. The inlay shows the particle size distribution. Additionally, the current and voltage gap relation with no size dependence is shown (i.e. using a constant regular solution parameter of 116 meV). This fitted particle size distribution is in stark contrast to the values reported by Dreyer *et al.*. [54] This could be because only a fraction of the electrode is being cycled. Since smaller particles will have a tendency to nucleate and fill first (especially if surface wetting is the main nucleation driving force), it's possible that although there were larger particles present, only the smaller particles are active and directly affect the voltage gap.

Figure 7-3d shows the relative particle sizes and fillings at a 0.5 filling fraction. Even at a standard deviation of 1, there is a strong size dependence on the particle filling, and slight differences in the voltage gap lead to preferential filling. As was

previously shown for an electrode with no size variations, on slow discharge (with a current density much less than the exchange current density), a discrete filling effect begins at the separator and propagates to the current collector (assuming negligible electron transport resistance). [58] However, with size variations, the model demonstrates more homogeneous filling throughout the electrode. Heterogeneous filling has been seen in images produced by Chueh *et al.*. [43]

In the end, there were three parameters used to fit the simulation to data: average particle size, standard deviation, and contact resistance. The exchange current density value was fitted, however, at such slow discharge rates, a range of values will produce the same effect, so this value should not be taken literally. Overall, the model demonstrates how size effects, especially with respect to surface wetting and nucleation, can be very important in $LiFePO_4$ electrodes.

7.2 Diffusion-Limited Dynamics with Three Phases

Next we consider (electrolyte) diffusion limited dynamics in a porous electrode. Graphite experiments by Harris *et al.* are an excellent representative case for these dynamics. [67] Harris "unrolled" a graphite anode to create a very long diffusion length across the electrode. The electrode was discharged at a constant potential of 2 mV (very close to short circuit).

The long diffusion path combined with near short circuit constant potential creates a large initial flux of lithium into the particles, which depletes the electrode and creates an electrolyte transport limited intercalation front that propagates from the separator to the current collector in the cathode (i.e. the graphite electrode). The speed of this reaction front is completely controlled by electrolyte transport due to depletion ahead of the reaction front. The characteristic transport time across this long electrode ($\sim$ 1 mm) is on the order of hours. By scaling the system to this rate limiting time, the kinetics of the system can be treated as very fast. The experimental setup, which bisects the electrode with the current collector, also eliminates the need to model the electron conduction, and all electrons in the electrode can be assumed to have the

same potential.

We wish to model this system using Modified Porous Electrode Theory, although it requires the use of a free energy function for graphite. Graphite is a complicated intercalation material, with multiple phases (often referred to as "stages"). [101] Here, presented for the first time, is a new model for graphite that captures multiple stable phases. This model was first introduced by Bazant. [11, 12]

There are five stages of Li_xC_6 as x varies from zero to one. The model makes use of the fact that the predominant stages (i.e., the stages whose states are most often observed) are stages I and II, which produce noticeable voltage plateaus. In addition to the voltage plateaus, graphite also undergoes a color change during lithiation. As x varies from zero to one, Li_xC_6 undergoes a color change from black to blue to red to gold. The black color is visible when x is very small. The transition from black to blue happens early on. It is difficult to say where due to the multiple stages, however, for the purpose of this model, we assume that very small values of x are blue. Stage II's color of red is reached somewhere near the quarter filling state, where the first noticeable plateau is reached. The gold color emerges when the stage I filling state is reached, which is somewhere just past the half filling point (i.e. the gold color emerges as layers begin the stage I filling). This stage produces the widest voltage plateau.

Therefore, the model must be able to capture two voltage plateaus. This is accomplished by modeling LiC_6 as two representative layers, each with its own free energy model, combined with an interaction energy between the layers. The free energy per atom is given by

$$g(x_i, x_j) = \overline{g}(x_i) + \overline{g}(x_j) + \Omega_b x_i x_j + \Omega_c x_i(1 - x_i)x_j(1 - x_j), \tag{7.2}$$

where x is the filling fraction of the representative layer, Ω_b is the interaction energy between layers, Ω_c is similar to a strain energy, and $\overline{g}$ is the regular solution model

(also per atom), given by

$$\overline{g}(x_i) = k_B T \left[x_i \ln x_i + (1 - x_i) \ln(1 - x_i)\right] + \Omega_a . x_i (1 - x_i). \tag{7.3}$$

In Equation (7.3), Ω_a is the regular solution parameter. Calculating the open circuit potential (OCP) requires the chemical potential. During intercalation, each layer is treated individually (i.e. each layer has its own OCP and subsequent reaction rate). The OCP of layer i is given by

$$\Delta\phi_{eq,i} = \Delta\phi^o_{eq} - \mu_i, \tag{7.4}$$

where $\Delta\phi^o_{eq}$ is the standard potential (in reference to lithium metal) and μ_i is the chemical potential of layer i, given by

$$\mu_i = \frac{\partial g(x_i, x_j)}{\partial x_i} = \overline{\mu}_i + \Omega_b x_j + \Omega_c x_j (1 - x_j)(1 - 2x_i). \tag{7.5}$$

In Equation (7.5), $\overline{\mu}_i$ is the homogeneous chemical potential of layer i, given by

$$\overline{\mu}_i = \frac{\partial \overline{g}}{\partial x_i} = k_B T \ln\left(\frac{x_i}{1 - x_i}\right) + \Omega_a \left(1 - 2x_i\right). \tag{7.6}$$

The total filling fraction of a "particle" is the average of the two representative layers. This model has four fitting parameters: the regular solution parameter, Ω_a (inside the layer), the interaction energy between layers, Ω_b, the strain-like energy, Ω_c, and the standard potential, V^o.

Understanding the effects of each parameter aids in fitting the values. The regular solution interaction energy, Ω_a, determines the width of the voltage plateau. The interaction energy between layers, Ω_b, determines the voltage difference between the two plateaus, and the standard potential, V^o, shifts the voltage. The strain energy term, Ω_c, only affects the homogeneous free energy (i.e. the energy when both layers have the same filling fraction). There is no way to fit the strain energy term to voltage data since it is the homogeneous free energy, which is not observed in graphite at OCP

conditions (i.e. the state is unstable). Therefore, the Ω_c parameter is chosen to be arbitrarily large, such that it forces the particles to "phase separate" (i.e. have one layer fill preferentially over the other).

First, the graphite model was fit to data using a C/1000 MPET simulation. Each representative layer was modeled as having its own reaction rate. The slow discharge simulation (which allows the transport effects to be neglected) was used to fit the model parameters. Values of $\Omega_a = 3.4\mathrm{k}_B\mathrm{T}$, $\Omega_b = 1.4\mathrm{k}_B\mathrm{T}$, $\Omega_c = 30\mathrm{k}_B\mathrm{T}$ (set), and $V^o = 0.1366$ V were found to fit the OCP data very well.

Once the free energy parameters were obtained, a constant potential discharge simulation was run. The simulation was a full cell simulation with a lithium metal anode and graphite cathode. Transport effects on the lithium metal electrode were assumed to be negligible, and the porosity on that side was treated as unity. The important transport effects are on the graphite side, where there is a sharp depletion from the separator to the intercalation front. It is necessary to simulate a full electrode since the diffusivity is fit. If a half cell is modeled, a sharp concentration gradient across the separator results, leading to a predicted diffusivity that is too small. Modeling the entire cell provides more electrolyte (namely inert anions) leading to a smaller concentration gradient across the separator and a more suitable diffusivity.

The length scale was scaled to the separator thickness, which was approximated from images provided in the original paper to be about 1.23 mm. [67] The electrodes were assumed to be on the order of 1.2 cm (or 10 times the separator thickness). The total length is not important since the color effects are observed in the first couple millimeters. The simulation time was scaled to the diffusive time across the separator which is on the order of one hour. This allows the exchange current densities (which are also scaled to the diffusive time) to be treated as arbitrarily fast. A dimensionless value of 1 was used for both exchange current densities (graphite and lithium metal), which equates to approximately 1.4 A/m^2 for 5 μm spherical particles (particle sizes of 5-20 μm were observed).

The volume fraction of graphite in the electrode was assumed to be 0.8 and the Bruggeman relation was used to model porous transport effects. The cell was simu-

lated at 2mV. The length scale was set from experiment, so the time was scaled to get the fit seen in Figure 7-3c. A time shift (along the x axis) and time scale were fit to the data using a least squares regression. The fit ambipolar diffusivity was then calculated via L^2/t_d.

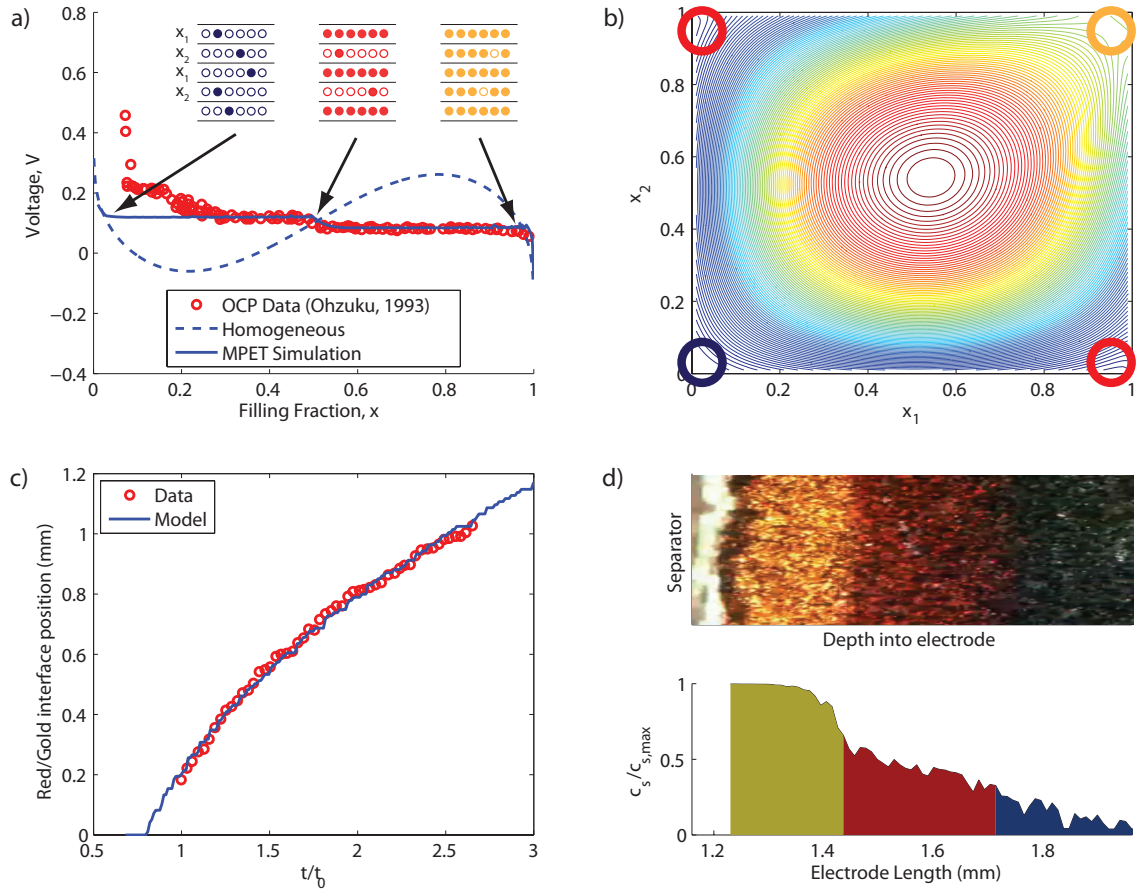

Figure 7-3: **Comparison of graphite model to OCP and the electrolyte diffusion limited case** Figure (a) shows a comparison of the graphite model with the OCP (data from [101]). Figure (b) is a contour plot of the free energy given by the model. The free energy surface has four minima near the corners. As lithium intercalates, the reaction coordinate proceeds along the lines connecting these minima. Figure (c) shows the red/gold interface position versus time compared to experimental data. Figure (d) shows a comparison between experimental data (from video of the experiment) and simulation. Experimental data in figures (c) and (d) is adapted from [67].

Figure 7-3a demonstrates the model's agreement with experimental data. The solid curve is an MPET simulation using the aforementioned graphite model at a discharge rate of C/1000. The dash curve represents the homogeneous voltage (i.e.

$x_1 = x_2$). The stress term given by Ω_c causes this voltage to go negative and makes it favorable for the particle layers to fill discretely. The inlay in Figure 7-3a shows the representative graphite particles (i.e. the two layers used to represent graphite particles). The particles consist of alternating x_1 and x_2 layers. Close to empty, lithium is randomly distributed throughout the layers. As lithium intercalates, the model causes alternating layers to fill preferentially, producing the first voltage plateau. Which layer fills (i.e. x_1 or x_2) is random, but has no effect on the voltage since both states have the same chemical potential. After one layer fills, the other layer fills preferentially, producing the second voltage plateau.

The free energy model defines three separate states in the particles (blue near empty, red near half filling, and gold near full filling), however, it does not define where this transition occurs. Somewhere past the first local minima, the transition from blue to red occurs, and somewhere past the half filling state, the transition from red to gold occurs. The model demonstrates a sharp solid concentration gradient along the electrode between the half filling and filled states. We assume that around 0.6 (i.e. just past the half filling) the particles transition from red to gold. Given the sharp gradient in solid particle concentration across the electrode, the choice of this concentration does not have a large effect on the fit diffusivity.

The blue/red interface is more difficult to define, since real graphite has multiple stages at low concentration. We assume the blue to red transition occurs around a filling fraction of 0.3. This produces a good qualitative agreement with data, although it is not required when the model is fit to the red/gold interface data and does not affect the fit diffusivity. Coincidentally, the 0.3 filling fraction is located near the beginning of the first plateau in the OCP data, which could be interpreted as the beginning of the first phase represented in this model.

The contour plot in Figure 7-3b represents the free energy as the layers are filled. The homogeneous state is penalized by a large free energy in the center of the contour plot. There are four minima located near the corners corresponding to the empty, half-full, and full states. As lithium intercalates, it starts near the blue circle (empty state), then progresses towards one of minima inside the red circles (at random) then

towards the minimum inside the gold circle.

Figure 7-3c shows a comparison of the red/gold interface position versus time. The model was fit to data using a least squares regression. Simulations were run at various cathode porosities (since this value was not reported), then the ambipolar diffusivity was fit to the data presented in the paper for the red/gold interface position versus time. Our model was scaled to the separator length (about 1.2mm, the length was obtained from images in the paper). The time was scaled to the electrolyte characteristic diffusion time (i.e. L^2/D_{amb}), which was one of the unknown parameters fit to the experimental data (via rescaling of the simulation time scale). The simulation fit to data is for a porosity of 0.4. The fit produces an ambipolar diffusivity of $4.6\text{x}10^{-10}$ m^2/s, which is good agreement with experimental values in EC/DEC. [125]

In addition to matching the color profiles and length and time scales, the model makes other predictions that qualitatively agree with the data. The mosaic effect can be seen when particles (or portions of particles) preferentially fill prior to other particles. [31] This was also observed experimentally in the graphite electrode. [67]

7.3 Conclusion

The advantage of MPET is that it couples thermodynamics inside the electrode to transport and kinetics. Phenomena such as phase transformations and hysteresis can not be captured in traditional battery models without artificially inserting them. MPET takes the free energy of the material as an input and couples it to kinetics, which then produce these phenomena. Other effects, such as temperature dependence are also handled by MPET, as thermodynamic properties scale with temperature, including the open circuit potential.

This chapter demonstrated good agreement with experimental data for two specific cases of phase transforming materials. The first case was very slow discharge of $LiFePO_4$ particles and modeling the zero current voltage gap. The second case involved electrolyte transport limited intercalation of graphite. In the case of the zero current voltage gap, the gap is a result of the non-equilibrium behavior of the

particles. At equilibrium, $LiFePO_4$ phase separates, producing a voltage plateau. However, during lithiation, particles can behave more homogeneously due to coherent stress and current induced suppression of phase transformation. [45, 8] Surface effects in the form of surface wetting can play a large role, as was shown in this paper. These effects are responsible for the voltage gap being smaller than is predicted by equilibrium thermodynamics of the particles.

In the second case, a new model for graphite was presented and fit to data with great accuracy. In the graphite model, the free energy of the particles coupled to the kinetics and transport in the electrolyte generates color profiles that match experiment. These colors emerge as a result of the free energy model. In traditional battery models, these effects would need to be artificially inserted into the model. More work is needed on this new graphite free energy model to compare with other experiments and test its validity when electrolyte transport is not limiting.

Chapter 8

Modeling Lithium Iron Phosphate Electrodes

The recent work by Cogswell and Bazant investigating the effects of particle size, surface wetting, and coherency strain on the lithiation dynamics of $LiFePO_4$ (LFP) particles represents an important step towards understanding the dynamics of the material. [44] The model, which modeled plate-like nanoparticles in 2D with the third dimension depth averaged, captured the source of the zero-current voltage gap that was first observed and explained by Dreyer *et al.*. [54] Dreyer attributed this zero-current voltage gap to particle-particle effects at the electrode scale using a non-monotonic free energy model. Cogswell and Bazant expanded on this using phase field modeling to explain why different voltage gaps were observed in different LFP electrodes, and why the 20 mV observed in Dreyer's work differs from the voltage gap predicted by solid solution (i.e. homogeneous) thermodynamics.

In the previous chapter, a simplified form of this model was presented and fit to the data of Dreyer *et al.*. [54] This is useful for very slow charge and discharge models, since the particle-by-particle filling leads to large local current densities that suppress any phase separation behavior. However, as the discharge rate is increased, the number of active particles increases. This means the local current density of the particles is smaller, and it might no longer be reasonable to assume that phase separation dynamics are suppressed. Bai *et al.* demonstrated that the local current

density with respect to the exchange current density needs to be order one to suppress phase separation. [8] Without simulations, it's difficult to know exactly what these local current densities are due to particle-particle interactions at the electrode scale.

This chapter represents the most recent work on modeling a LFP electrode. The first part of this chapter will present the single particle model that will be used. It is a simplified (i.e. 1D) version of Cogswell and Bazant's 2D model. Once the single particle model has been presented, a section on inserting it into the porous electrode, and how to include different sized particles, will be presented. Finally, some charge and discharge examples, along with comparison to experimental data will be presented.

8.1 Single Particle Model

The complete model used by Cogswell and Bazant was in 2D, with the third dimension (the depth, or [010] direction) averaged. This model is quite computationally expensive. Therefore, we wish to reduce the model to capture the same dynamics, but make it less computationally expensive. Despite the full model being in 2D, the overall dynamics of the system behave much like a 1D system, as the phase interface propagates in the [100] direction across the surface. To simplify computation, we model 1D particles. The particle shapes and sizes are the same as in Cogswell and Bazant's paper (also in the previous chapter). [44] The C3 shape particles are taken from Smith *et al.*. [121] Once again, the thickness of the particles has to be assumed, and a value of 20 nm is used. [121, 115]

To model the particles, the Cahn-Hilliard free energy functional, along with an approximated coherency strain term are used. The chemical potential, based on this free energy functional, is given by Equation 4.50. It is

$$\mu = \overline{\mu} - \nabla \cdot \left(\frac{\kappa}{\rho_s} \nabla \tilde{c} \right) + \frac{B}{\rho_s} \left(\tilde{c} - X \right). \tag{8.1}$$

Values for ρ_s, κ, and B are taken from other work by Cogswell and Bazant. [45]

In this chapter, the dimensionless LFP concentration will be represented by $\tilde{c}$. The value of B depends on the orientation of the interface as well as whether or not the particles have coherent or semi-coherent strain. This model assumes semi-coherent strain, since it is improbable that the particles are perfect crystals. The value of B in the [100] direction for the case of semi-coherent strain, is almost the same as the [101] direction in coherent strain. [45] Modeling phase separation in the [101] direction requires the full 2D model. Interestingly enough, this semi-coherent 1D model should have very similar effects from strain as the full 2D coherent case. The homogeneous chemical potential, $\overline{\mu}$, is the regular solution model, and the value of Ω is also taken from Cogswell and Bazant. [45]

One last effect that needs to be modeled in this system is the surface wetting of the particles. In the full model, surface wetting is controlled by the boundary condition, which dictates continuity of μ. Bazant referred to this as the "natural boundary condition" and it is given by

$$\frac{\partial \gamma}{\partial \nabla \tilde{c}} = \hat{n} \cdot \frac{\partial g}{\partial \nabla \tilde{c}} = \hat{n} \cdot \kappa \nabla \tilde{c}. \tag{8.2}$$

One property of LFP is that the difference between the interfacial energies on the facets is quite large, such that it's probable that specific surfaces prefer to be completely wetted or de-wetted. [44] This means the boundary condition can be approximated using either a high concentration (near full) or a low concentration (near empty) depending on the surface. Given the orientation of our 1D particles, the side facets are treated as fully wetted (i.e. the dimensionless concentration is close to 1). The top facet (the top [010] plane) should be de-wetted. However, this would increase the computational complexity. For this model, the de-wetted top surface is neglected. This surface could play an important role in the charge transfer reaction, though, so depending on how well the model fits data and how reasonable the parameters are, this effect may need to be added back into the model.

To simplify modeling the surface wetting, this model adds an additional volume at the ends of the particles where lithium concentration is held constant. In these

simulations, the value is held at $\tilde{c} = 0.98$. This surface wetting, combined with the strain, leads to interesting behavior as particle size is varied.

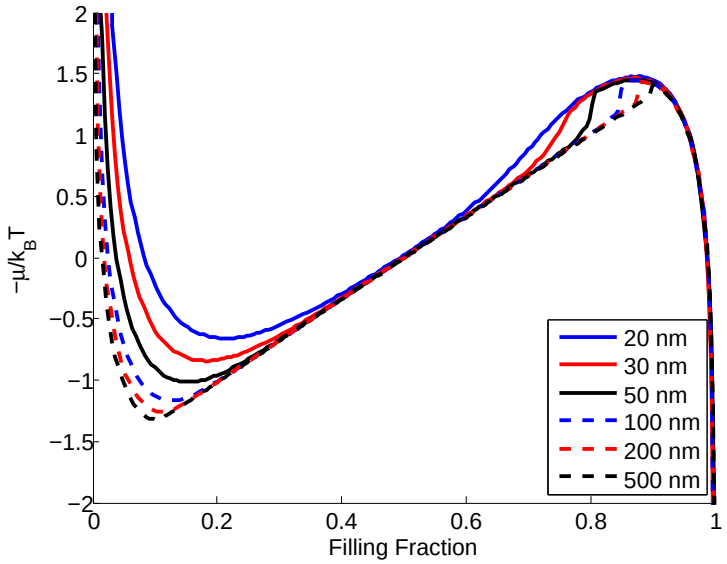

Figure 8-1: **Slow discharge of different sized particles** This plot shows the voltage profile for slow discharge of different sized particles. The shrinking of the voltage overshoot required to drive lithiation can be seen as particle size is decreased.

Figure 8-1 shows slow discharge of different sized particles. Some important features can be seen in this figure, including the position of the first local minimum, the tilted voltage plateau near half filling, and the voltage as the particle approaches its full state. The position, and value, of the first minimum is caused by the balance between strain and surface wetting. For smaller particles, the surface wetting represents a larger fraction of the particle. This reduces the potential required to drive lithiation. Another feature of the simulations is the size dependent miscibility gap (i.e. the gap between the minimum and maximum). This is a bulk effect caused by the ratio of the particle size to the width of the phase interface. The miscibility gap shrinks as the particle size decreases, since the phase interface corresponds to a larger fraction of the particle.

The tilting of the voltage plateau in the center is caused by strain in the particle, which is alleviated as the particle fills. Near the local maximum on the right side, interesting behavior can be seen for different sized particles. The effect observed is

the result of the particle size dependence and the phase separated behavior. With surface wetted nucleation, the lithium rich phases begin at the edges of the particles and propagate towards the center. For smaller particles, this phase interface occupies a larger fraction of the particle. Conversely, for larger particles, the phase interface occupies a smaller portion of the particle. The width of the phase interface relative to the particle size is important when the two phase interfaces collide and the particle becomes homogeneous. For very small particles, the interfaces overlap and smoothly fill, producing the smooth voltage curve. At intermediate sizes, there is a sharp voltage spike associated with the interfaces colliding and filling quickly to a homogeneous state. For very large particle sizes, this sharp voltage jump is reduced since the volume that fills quickly is a very small fraction of the particle (i.e. its behavior does not strongly affect the voltage curve).

This figure is very similar to Figure 4a in Cogswell and Bazant. [44] Despite the reduction of the model (i.e. from 2D to 1D), the figures are similar because of the properties of $LiFePO_4$. Cogswell and Bazant demonstrated previously that coherent strain leads to intercalation front propagation along the [101] direction. Furthermore, imperfections in the crystal, leading to semi-coherent strain, lead to intercalation front propagation in the [100] direction. [45] For this material, it just so happens that the strain energies of the coherent and semi-coherent cases are approximately the same. Therefore, the 1D case has very similar energetics to the 2D case. There are slight differences, however, since the full 2D case, even with semi-coherent strain, has effects from phase propagation along the [101] direction. For the purposes of this simulation, though, this 1D model is a suitable representation of the $LiFePO_4$ particles, as it demonstrates similar behavior and effects from particle size and surface wetting.

8.2 Porous Electrode Modeling of Surface Wetted LFP Particles with Coherency Strain

The overall goal is to use single particle models to gain insight into how porous electrodes behave. Before that can be accomplished, though, the single particle model must be inserted into a model for the porous electrode. Modified Porous Electrode Theory (MPET), the focus of this thesis, is such a framework, as it couples all of the effects inside the electrode to the thermodynamics of the system, including reaction kinetics, transport, and the potential boundary condition. This section will deal with incorporating the single particle model in the porous electrode, as well as how to accurately represent a particle size distribution in a volume averaged system.

Inserting the ACR equation itself into the MPET framework is straightforward based on the equations presented in this thesis. The chemical potential in Equation 8.1 can be used to calculate the activity. Transport in the electrolyte is handled via the aforementioned mass conservation equations. One of the most important features to add to the simulation is the particle size distribution. The size of the particles affects the voltage profile as well as the distribution of current in the electrode.

In the previous chapter, where a size distribution was fit, the pseudocapacitor model was used, which allowed concentration profiles inside the particles to be neglected. This allowed for hundreds of particles to be modeled. In this model, though, concentration profiles inside the particles need to be modeled with a resolution of at least 1 nm in order to capture any phase interfaces. This corresponds to about a hundred volumes per particle for particles on the order of 100 nm. Hundreds of particles means there will be tens of thousands of solid volumes. This makes the system very slow to simulate.

It's advantageous to try to represent the electrode using as few particles as possible. This is problematic, though, because too few particles won't accurately represent the electrode, and too many particles will take a very long time to compute. Adding a particle size distribution makes this more difficult. If particle sizes are chosen at random, then a suitable number of particles needs to be added such that the size

distribution is accurately represented. Figure 8-2 represents a couple different ways the particle size distribution can be added.

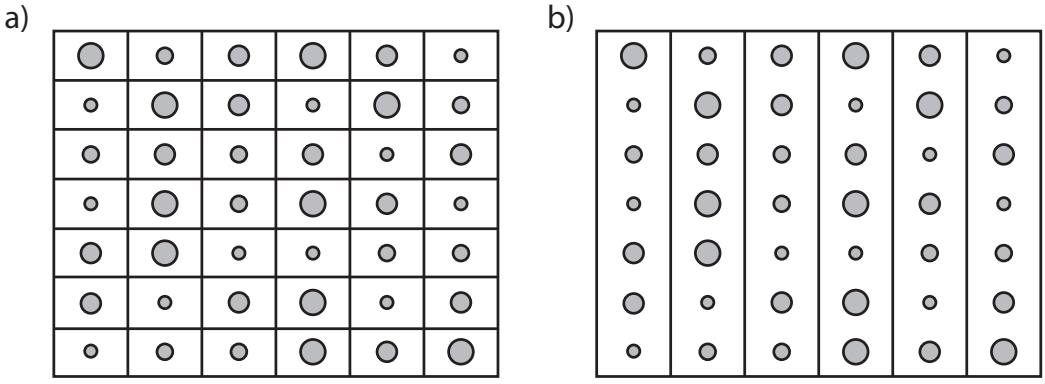

Figure 8-2: **Different schemes for addressing particle size distributions** The figure denotes two possible methods to include particle size distributions. The scheme on the left uses a 2D grid with one particle size in each volume while the scheme on the right uses a 1D grid with a particle size distribution inside each volume. For fewer discretizations, the scheme on the right captures the active area better than the scheme on the left.

Figure 8-2a shows a 2D grid, with random sized particles inserted into each of the volumes. If it is assumed that the volume of active material is roughly constant throughout the volume, then this method assumes that the representative particles are repeated inside the volume until the solid volume is reached. While this achieves the proper active solid volume fraction, the area of the active particles is not well represented. This is due to the surface to volume ratio of such small particles. Any volume that contains small particles will require more particles to match the volume of the active material, resulting in too large of an active area. Additionally, mass and charge conservation in the vertical direction need to be accounted for, adding computational complexity.

Figure 8-2b represents a suitable solution to this problem. Since transport in the vertical direction does not often have strong concentration gradients (i.e. gradients are predominantly along the horizontal axis, perpendicular to the separator), it makes sense to reduce the model to 1D, but add a particle size distribution inside each of the volumes. Each particle inside a respective volume is exposed to the same electrolyte concentration and potential. This simplifies the computation a bit. Furthermore, the

area of the active material in the volume is more accurate, since a correct number of large and small particles are represented. When scaling the simulation to the full porous electrode, now each volume is repeated to match the total active volume. This yields a better representation of the electrode.

8.3 Simulations

This section will present simulation results for the ACR model inside a porous electrode. Three different discharge rates were selected: C/50, 1.5C, and 5C. The particle concentration profiles are shown at filling fractions of 0.25 and 0.67 for each simulation to highlight the differences in the electrode filling mechanisms. These filling fractions were arbitrarily chosen.

The values selected here are chosen to highlight the particle-particle effects. A 50 μm electrode with a 25 μm separator was simulated. The electrode porosity was set to 0.4 and the volume loading percent was 0.7. This porosity is larger than typical batteries, and prevents electrolyte limitations at modest discharge rates (e.g. 5C). The electrolyte was 1M $LiPF_6$ in EC/DMC. [1] The particle size distribution was set to an average particle size of 160 nm with a 20 nm standard deviation. Five volumes inside the electrode were simulated (i.e. each volume is approximately 10 μm long) with four representative particles in each volume. A charge transfer coefficient of 0.5 was used.

First, the C/50 discharge simulation is considered. Figure 8-3 shows the voltage versus filling fraction and solid concentration profiles for the representative particles throughout the electrode. The most noticeable effects in the voltage plot are the small bumps observed towards the end of the discharge. These bumps are caused by the discreteness of the model. With only 20 particles, single particle effects (namely the non-monotonic voltage profile of a single particle) are observed as the number of particles capable of sustaining the current approaches the single particle limit. In a real electrode, this effect would not be observed since there are millions of particles. Similarly, if millions of particles could be simulated, the effect would not be seen here

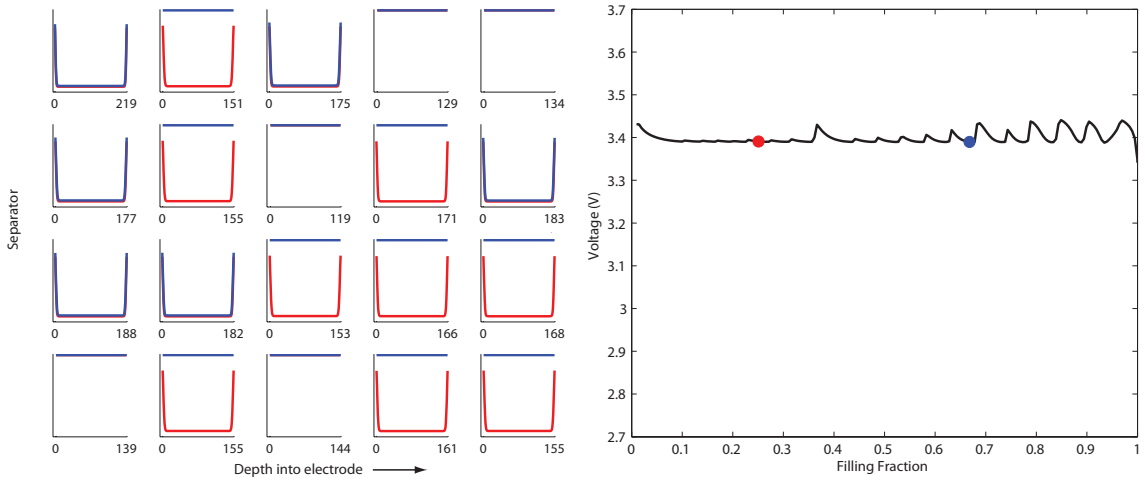

Figure 8-3: **C/50 discharge of ACR MPET model** This figure shows solid concentration profiles and a voltage versus filling fraction for C/50 discharge. The red and blue dots correspond to the colored solid concentration profiles.

either.

It's difficult to see the method by which particles fill based on the provided figure. Movies of the intercalation inside the particle show that the particles fill homogeneously, despite the phase separation being nucleated with surface wetting. This is because the local current density is large enough to suppress phase separation. As more representative particles are added to the simulation, the actual particle size distribution is approached. For such slow discharge rates, the particles fill preferentially from smallest to largest. This is a consequence of the surface wetting and coherency strain in the particles, which leads to different overpotentials required to drive lithiation. This model predicts that even with slow discharge the particles fill homogeneously.

The red and blue dots denote the solid concentration profiles at different depths of discharge. The red dot (which accompanies the red concentration profiles) is located at a filling fraction of 0.25, while the blue dot (which matches the blue concentration profiles) is located at a filling fraction of 0.67 (i.e. two thirds filling). The strong size dependence can be seen in the concentration profiles, as the smaller particles fill first followed by the larger particles. This is due to the size dependence from the surface wetting and coherency strain, as demonstrated in Figure 8-1. Smaller particles require

less overpotential to drive lithiation. At two thirds filling (i.e. the blue point), it can be seen that the next smallest particles have filled, and the largest particles remain delithiated. This progression of filling from smallest to largest progresses until the electrode is filled.

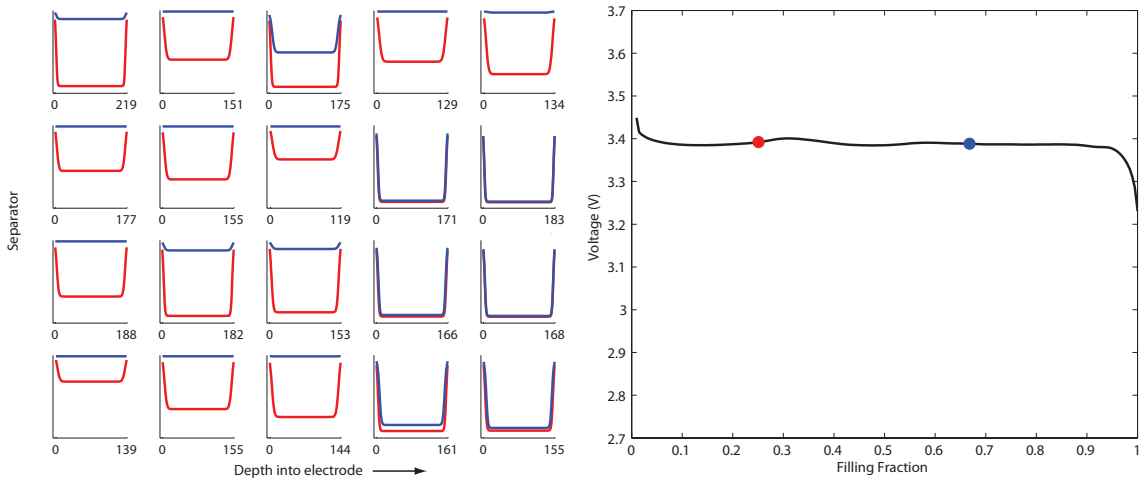

Figure 8-4: **1.5C discharge of ACR MPET model** This figure shows solid concentration profiles and a voltage versus filling fraction for 1.5C discharge. The red and blue dots correspond to the colored solid concentration profiles.

At a 1.5C discharge, lithium transport in the electrolyte begins to compete with the particle size effect. In Figure 8-4, the same particle sizes are used as in Figure 8-3. The first noticeable difference is that the voltage curve no longer has the spikes from single particle behavior. This is because multiple particles are active to satisfy the current. Another noticeable effect is the emergence of a lithiation front, as larger particles that are closer to the separator fill before smaller particles deeper in the electrode. This is not completely the case, though, since some smaller particles deeper in the electrode still fill first.

The reason for this is due to concentration polarization in the electrolyte. In these simulations, electrons are assumed to be readily available, and the potential drop in the carbon black phase is not modeled. If all the particles had the same capacitance, they would fill from the separator to the current collector. The coherency strain and surface wetting breaks this effect, but for particles close to the same size, there is a positional dependence. As lithium diffuses through the separator, it is easier to

fill particles closer to the separator rather than particles deeper in the electrode (i.e. closer to the current collector). This positional dependence becomes more pronounced with faster discharge.

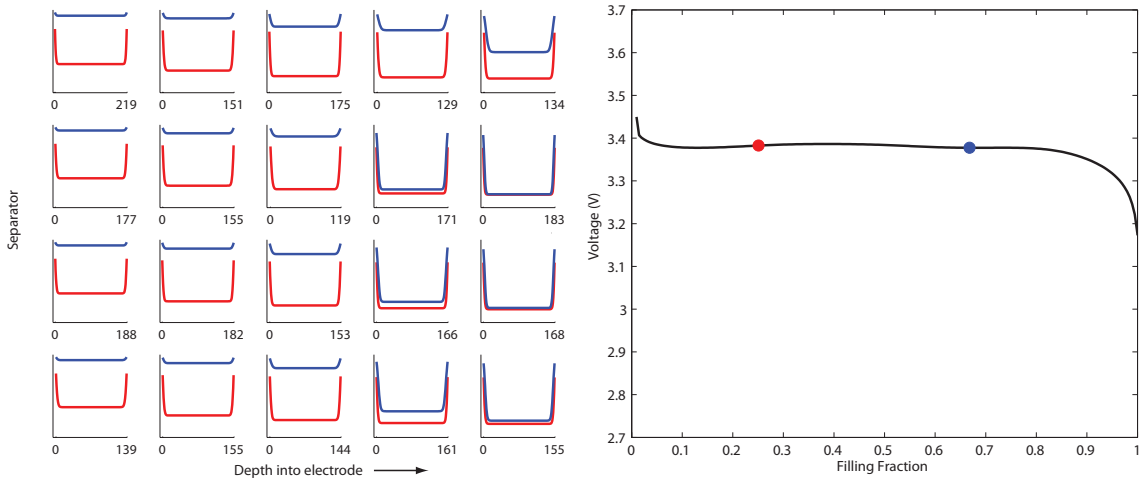

Figure 8-5: **5C discharge of ACR MPET model** This figure shows solid concentration profiles and a voltage versus filling fraction for 5C discharge. The red and blue dots correspond to the colored solid concentration profiles.

Figure 8-5 shows the discharge of the same electrode (i.e. the same particle sizes) at 5C. The solid concentrations are very similar to the 1.5C discharge in Figure 8-4. The main difference is in the voltage curve, though, which has been smoothed. This is because the number of active particles has increased, reducing the fluctuations in voltage associated with discrete filling in the electrode. Another difference is the end of the voltage plateau, which shows a sweeping dropoff. This dropoff is caused by variations in particle size. At constant current, as particles fill, fewer particles are forced to sustain the same current, leading to increased overpotential. A particle size distribution enhances this effect. Despite multiple particles being active, smaller active particles still fill ahead of larger particles due to their smaller capacity. At the end of the discharge, the current needs to be sustained by fewer particles. This leads to increasing overpotential as particles "turn off", leading to this sweeping dropoff that has also been observed experimentally. [76]

Next, we look at how particles behave when charging. Figures 8-6 and 8-7 show charging at C/50 and 1.5C rates. In Figure 8-6 the particles empty discretely and

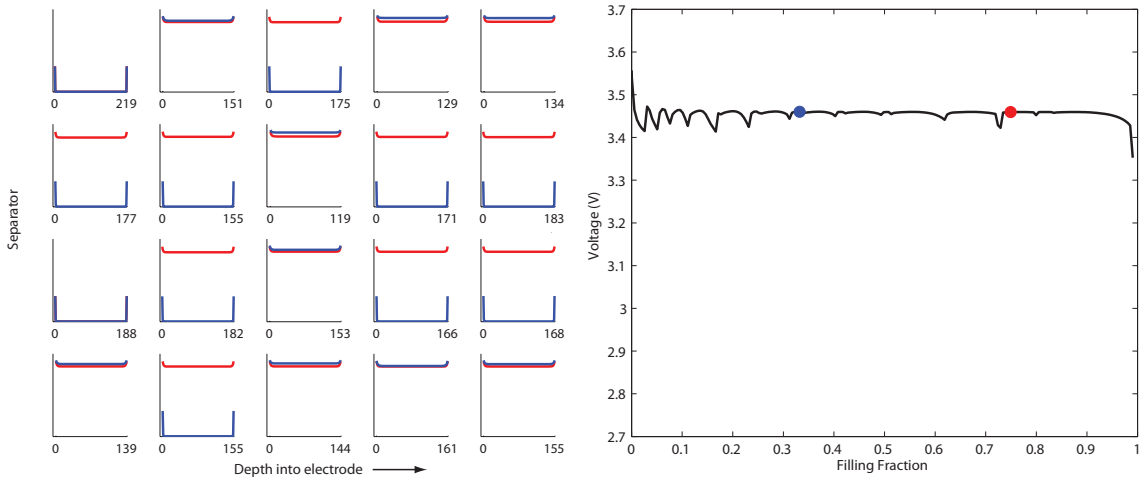

Figure 8-6: **C/50 charge of ACR MPET model** This figure shows solid concentration profiles and a voltage versus filling fraction for C/50 charge. The red and blue dots correspond to the colored solid concentration profiles.

based on size, as in the discharge example. Similarly, the bumps in the voltage plateau denote the discrete emptying events. The dots denote the same filling fractions as before, however, since the electrode is being charged, the red dot is reached first, then the blue dot. All of the particles reach roughly the same concentration near 0.9, and then proceed to discretely empty. The voltage plateau is located above 3.42V standard potential, demonstrating that this model also captures the voltage gap previously shown.

The more interesting behavior of charging is demonstrated when the charging rate is increased. Figure 8-7 shows the results for a 1.5C charging rate. After an initial climb in overpotential to drive the delithiation, all the particles reach a concentration around 0.6 (note the end of the line in the voltage profile) after which the particles discretely empty again, similar to the C/50 charging behavior. This behavior demonstrates the difference between discharge and charge dynamics. The model predicts that discharge at higher C-rates produce more homogeneous solid concentration profiles, whereas in charging, increasing the charging C-rate still produces some discrete effects.

Next, some experimental results from Li and Chueh will be presented to show the qualitative similarities between real electrodes and the ACR model presented in this

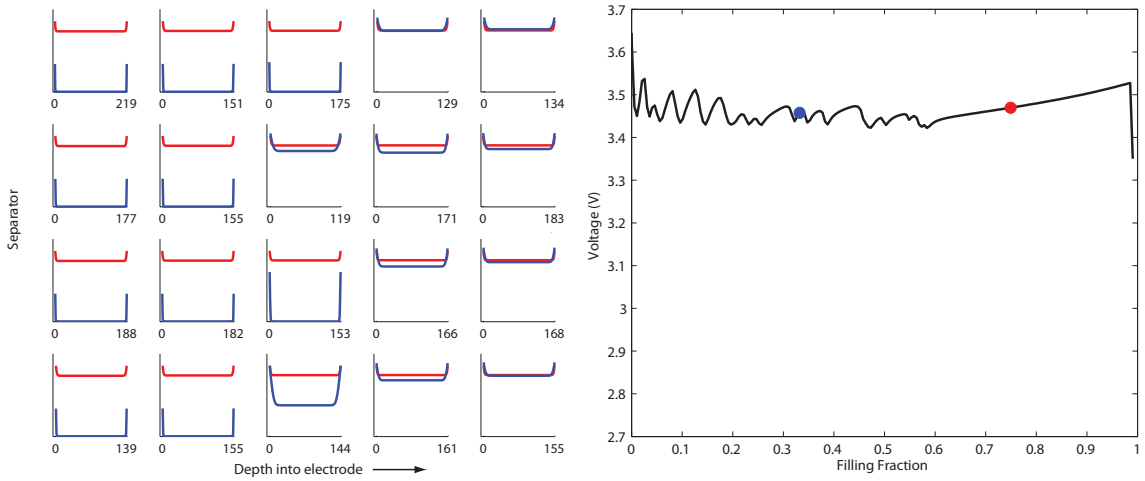

Figure 8-7: **1.5C charge of ACR MPET model** This figure shows solid concentration profiles and a voltage versus filling fraction for 1.5C charge. The red and blue dots correspond to the colored solid concentration profiles.

section.

8.3.1 Comparison to LFP Electrodes on Charge and Discharge

The data presented here are from Li and Chueh. [43, 91] The figures are a combination of TEM images and X-ray absorption spectroscopy taken on slices of a partially charged/discharged electrode (around half filling). The left image (TEM) denotes the position of solid intercalation particles in the electrode (the black masses) and the right image (X-ray absorption) denotes the filling fraction. The red sections are fully lithiated, the green sections are delithiated, and the yellow sections are intermediate concentrations. These yellow particles are considered to be "mixed", and can contain portions of red and green along with yellow. The number of mixed particles is what will be compared to the model in this section.

Figure 8-8 shows the number of mixed particles for discharge rates of C/50, 1.5C, and 5C. The C/50 and 1.5C discharge rates show that the number of mixed particles is low. This is similar to the behavior predicted by the ACR model in this chapter (near half filling). However, the model predicts more mixed particles for the 1.5C

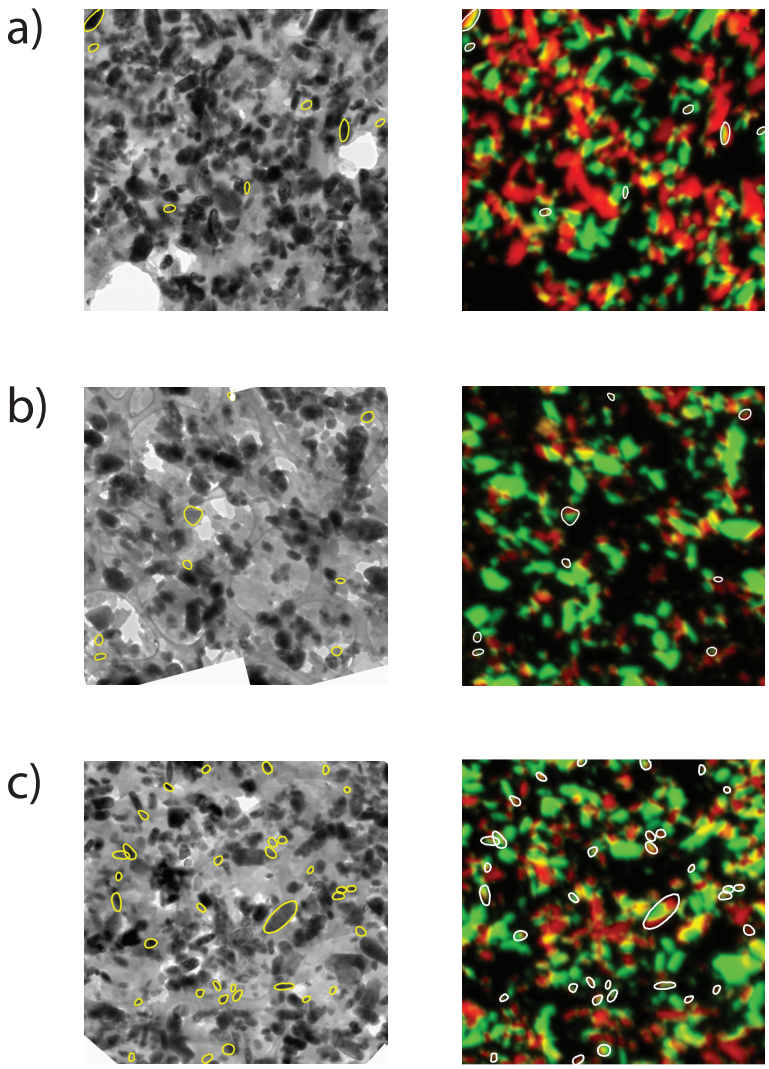

Figure 8-8: **Electrode after discharge** This figure shows the TEM and X-ray absorption spectroscopy images for discharge rates of (a) C/50 (b) 1.5C and (c) 5C. The circles indicate the positions of "mixed" particles which are either homogeneous or a mixture of full and empty portions, denoted by the yellow color. Figure courtesy of Li and Chueh. [91]

discharge. The 5C figure shows that there is a large percentage of mixed particles, which is similar to the behavior of the ACR model around half filling. The discrepancy at medium discharge rates (i.e. around 1.5C) will be discussed later in this section.

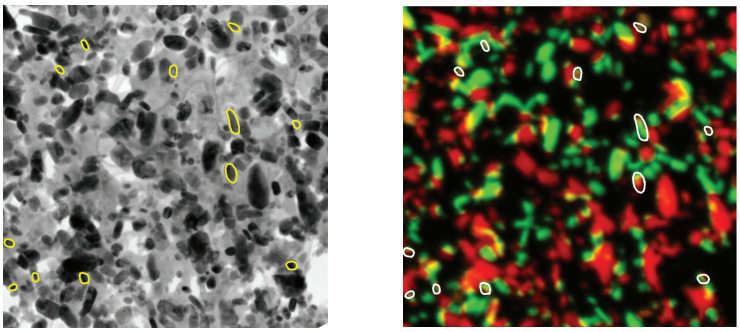

Figure 8-9: **Electrode after 1.5C charge** This figure shows the TEM and X-ray absorption spectroscopy images for a 1.5C charging rate. The circles indicate the positions of "mixed" particles which are either homogeneous or a mixture of full and empty portions, denoted by the yellow color. Figure courtesy of Li and Chueh. [91]

Figure 8-9 shows particles after a 1.5C charge. Similar to the discharge figures, the number of mixed particles is small. Other data from Li and Chueh (not shown here) suggest that on charging, despite the charging rate, the number of mixed particles remains much lower than on discharge. [91]

Given this experimental data, there are currently two discrepancies present between the model and the data. The first is that the number of mixed particles predicted by the model at intermediate discharge rates is too high. The 1.5C discharge model shows many mixed particles around half filling, although the data does not. The second discrepancy is that on charging, the model predicts that many particles (almost the entire electrode) is close to the partially filled state. Figure 8-7 shows all of the particles reach a filling fraction of approximately 0.6 prior to discretely emptying. This is in contrast to the charging data which show a small number of mixed particles.

In order to reconcile these differences, it's important to consider the method used in obtaining these images. The electrodes were prepared and then charged/discharged. After the charge/discharge, the cell electrolyte was drained and replaced

with resin to keep the electrode in tact. However, there is an approximate 5 minute relaxation time as the electrolyte is drained. To address this part of the experimental procedure, a relaxation time (i.e. open circuit conditions, no net current) is added to the end of the simulations.

Figures 8-10, 8-11, and 8-12 have the same format as the previous figures. The profiles on the left represent the solid concentration profiles. Instead of a voltage versus filling fraction figure, the right figure has been replaced with a voltage versus time figure to denote the open circuit potential evolution as the electrode relaxes. The voltage fluctuations are caused by charge transfer inside the electrode as lithium shifts between particles and the electrolyte relaxes to its initial state (i.e. uniform concentration).

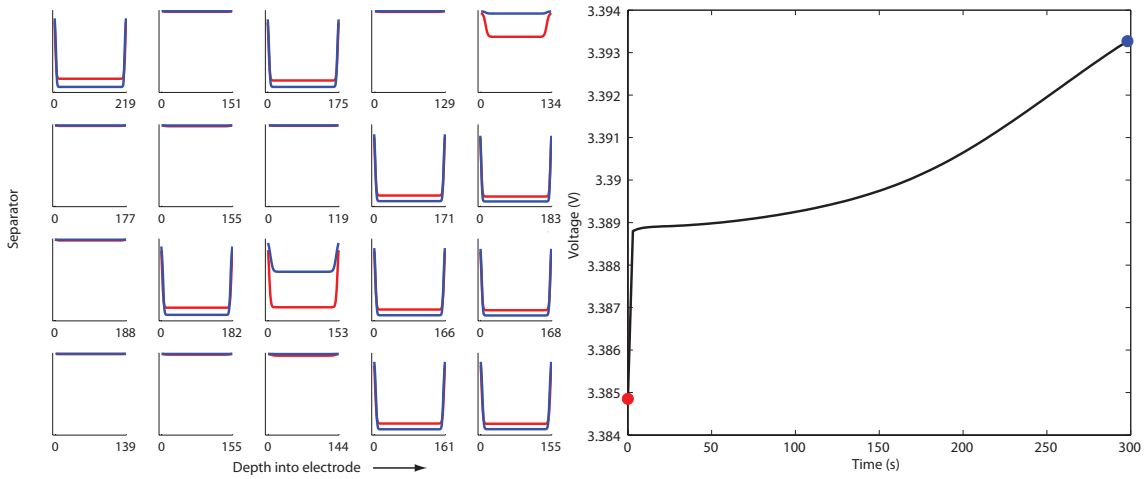

Figure 8-10: **Relaxation after 1.5 discharge of ACR MPET model** This figure shows solid concentration profiles and a voltage versus time for relaxation after a 1.5C discharge. The red and blue dots correspond to the colored solid concentration profiles at the beginning and end of the relaxation.

Figure 8-10 shows the concentration profiles after discharging at 1.5C to the half filled state then letting the cell relax for 5 minutes. The red and blue dots (which denote the potential at the different solid concentration profiles) are located at the beginning and end points. In this figure, the voltage jumps quickly to about 3.389V then slow relaxes towards the standard potential of 3.42V. This is because many of the particles are closer to their equilibrium state when the current is turned off. At

the end of the relaxation, there is one particle in the half filled (i.e. the "mixed") state. The figure demonstrates how the particles relax and explains why so few mixed particles are observed at 1.5C. Despite there being clusters of particles that fill discretely, these particles relax to empty and filled states and not many particles remain in the mixed state.

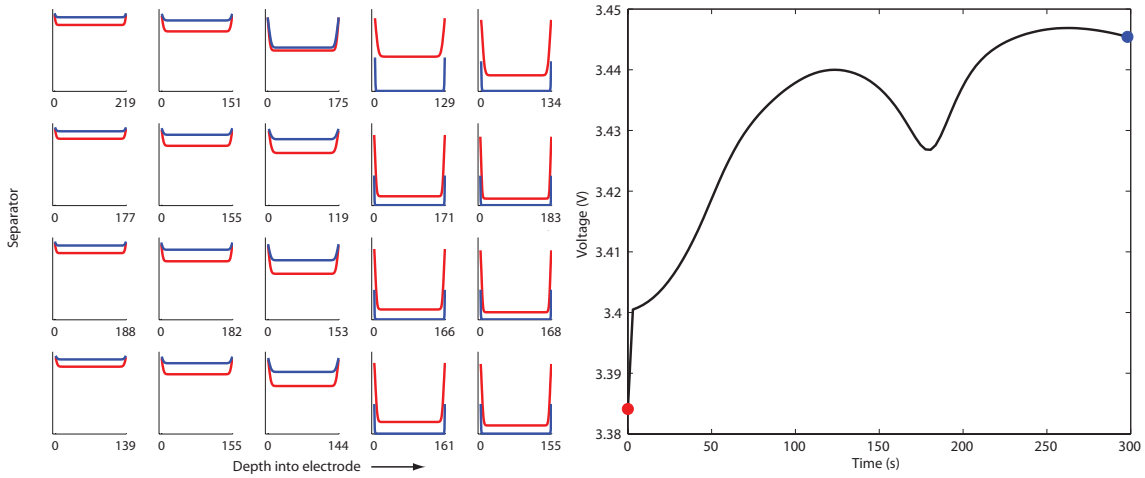

Figure 8-11: **Relaxation after 5C discharge of ACR MPET model** This figure shows solid concentration profiles and a voltage versus time for relaxation after a 5C discharge. The red and blue dots correspond to the colored solid concentration profiles at the beginning and end of the relaxation.

Figure 8-11 demonstrates relaxation after a 5C discharge to a filling fraction of 0.5. This voltage curve shows a lot more activity since there are more active particles near the half filled state when the current is turned off. To explain the kinetics of the relaxation, we must refer to the single particle voltage profiles in Figure 8-1. The phase separated and homogeneous voltage profiles are both non-monotonic. There happens to be three points in the profile at the standard potential. The two on the sides (i.e. near empty and full) are stable and the center point is meta-stable.

If the current is turned off, the model predicts that it may be possible for some particles to be trapped near the half filled state (whether they are homogeneous or phase separated). Although the voltage slopes upward (meaning the particle prefers to have more lithium), this process is driven by delithiation of surrounding particles. If nearest neighbors aren't in a suitable state for lithium exchange, then extra time

is needed to communicate to other particles via the electrolyte.

It is because of this that many of the particles remain in the mixed state even after relaxation. Particles closer to the minimum/maximum open circuit potential solid concentrations have a higher driving force to relax to the zero chemical potential state, either by lithiation or delithiation. Particles closer to the half filled state have a smaller driving force (i.e. overpotential) relative to other particles near the spinodal concentrations (i.e. the concentrations that correspond to the minimum and maximum potentials). Therefore even after relaxation, they could become "stuck" at this point, and take a long time to relax back to their empty or filled state.

It is important to note that the C/50 relaxation has been omitted here. This is because the relaxation shows little to no change in solid concentration. Because of how the particles fill, that is, discretely and nearly one-by-one, there is almost never a time in the system where large numbers of particles are largely out of equilibrium. When the current is turned off, the particles, which are already close to the stable points (full or empty) relax quickly, and no changes are observed.

These two figures show, qualitatively, why intermediate discharge rates such as 1.5C show so few mixed particles, and why faster discharge rates show so many mixed particles. A prediction from the model is that at even higher rates, the number of mixed particles (for the same ending filling fraction and relaxation time) will be the same. This has to do with how many of the particles in the electrode are active. Finally, the discrepancy on charging will be addressed.

Figure 8-12 shows the relaxation after a 1.5C charging to a filling fraction of 0.5. At the beginning of the relaxation, many of the particles are close to the half filled state. This was seen in Figure 8-7 as well, at the end of the sloping line. However, when the particles are relaxed, the active particles quickly relax and the particles near the half filling state deeper in the electrode lithiate back to near full states. This relaxation shows how despite there being many mixed particles, the relaxation process can reduce the number of mixed particles after charging.

The asymmetry between the number of mixed particles on charge and discharge is very interesting in the experiment. In the model, this is a consequence of the

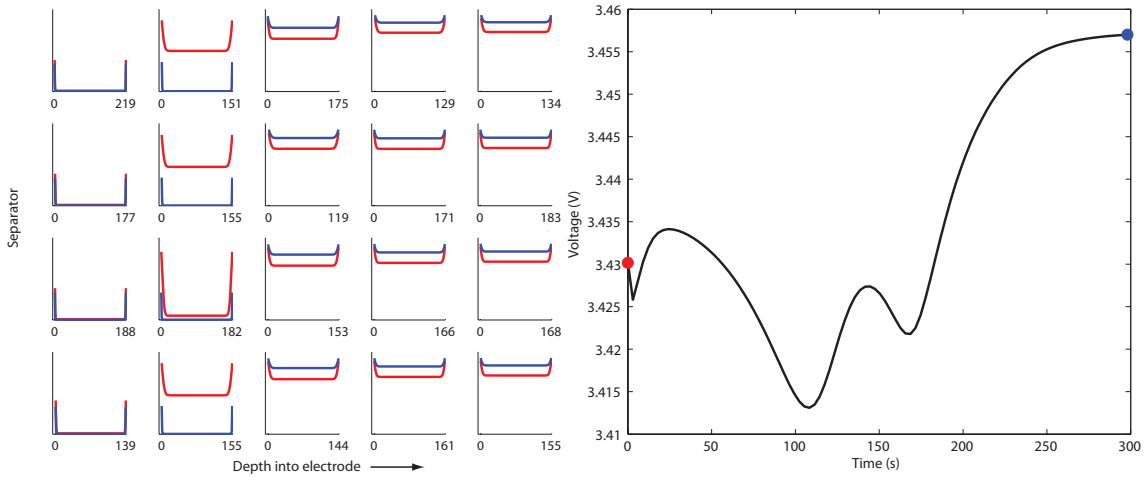

Figure 8-12: **Relaxation after 1.5C charge of ACR MPET model** This figure shows solid concentration profiles and a voltage versus time for relaxation after a 1.5C charge. The red and blue dots correspond to the colored solid concentration profiles at the beginning and end of the relaxation.

exchange current density model used, which includes the enthalpic effects from the regular solution model in the reductant activity. This enthalpic interaction skews the exchange current density, making it asymmetric and giving it a maximum near the lower concentration spinodal point. This term indicates that lithiation could be easier than delithiation, and that delithiation may require a larger overpotential, as shown in the charging simulations.

This term was naively included in some of the earliest forms of LFP models done by our group. [120, 33, 8] However, more work is needed to determine the accuracy of this term and whether it is accurate for the kinetics. An additional effect not included in the model is the de-wetting of the active surface. [44] Although the side facets are wetted and can nucleated the phase separation, the top facet, through which intercalation actually occurs is energetically favored to be de-wetted. This could affect the kinetics on charge and discharge, making charging more difficult since lithium needs to be brought to the de-wetted surface before it can undergo a charge transfer reaction to leave the particle.

8.4 Comparison with LFP Discharge Curves

Towards the end of this research, some work on fitting actual discharge curves was performed. The model itself has progressed a lot over the years, starting with the most basic features and evolving to a full phase field model with different effects added including coherency strain and surface wetting. This final model includes bulk electronic conduction as well, inserted using Ohm's Law in the solid matrix. The fitting shown here was performed by Moses Ender using data from his own work. [56] The model used was the ACR model presented in this chapter with electron conduction in the solid matrix added.

The simulation values used were an electronic conductivity of 0.0015 S/m, a contact resistance of .00025 Ohm·m^2, a porosity of 0.44, a volume loading percent of 0.79, a 300 μm separator, and a 24 μm electrode. The particle size distribution used was a 208 nm average particle size with a standard deviation of 73 nm. The exchange current used was 0.1 A/m^2, and a charge transfer coefficient of 0.2 was used. The electrolyte used was 1M $LiPF_6$ in EC/DMC (as in the previous simulations).

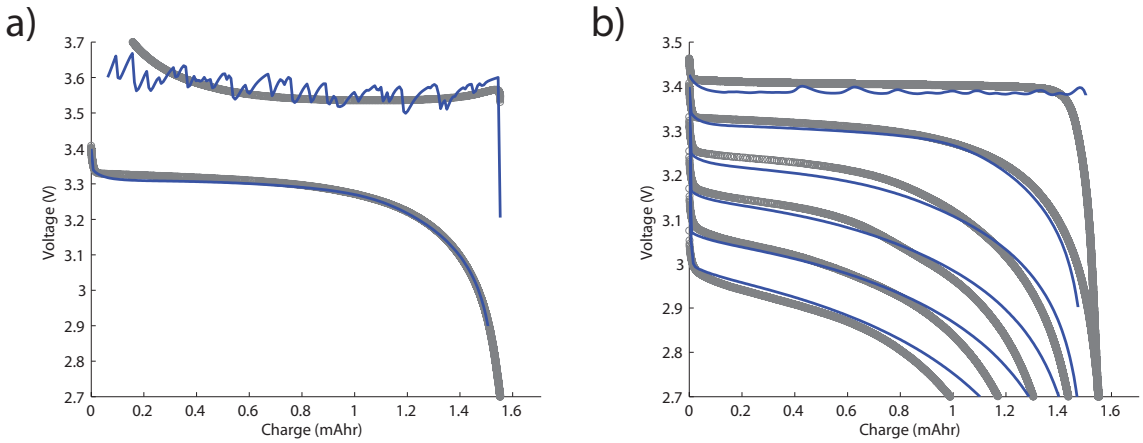

Figure 8-13: **Comparison of ACR MPET model with electronic effects to discharge curves** Figure (a) shows the fit to the 1C charge and discharge curves. Using the same parameters, figure (b) shows simulations at C/40, 1C, 2C, 3C, 4C, and 5C compared to experimental data. Figures provided courtesy of Moses Ender. The fit was performed using the MPET model presented in this chapter including electron conduction in the solid matrix.

Figure 8-13 shows the comparison between the ACR MPET model and experi-

mental discharge curves. The figure in 8-13a shows the initial fit to 1C charge and discharge curves. The initial fit captures the data very well. The 1C charging curve has some strong oscillations due to the discreteness of the model, but seems to capture the overall effects and the experimental data follows the average of the simulation values. In Figure 8-13b, the model captures the initial voltage for each of the discharge rates quite well. However, the model does not accurately predict the capacity of the cell.

The parameters used in this simulation were predominantly taken from experimental measurements and analysis of the microstructure. This is promising since the number of fitted parameters was small. However, the conductivity of the solid phase used is orders of magnitude smaller than that predicted by microstructure analysis. Given such a large difference, it's possible that effects are missing from the model, such as electron conduction in the poorly conducting LFP particles.

Despite not accurately capturing all the data, this fit shows that the model is proceeding in the correct direction. As this work continues and more effects are added to the model, fitting of voltage curves should improve.

8.5 Conclusion

This chapter highlights the most recent work using MPET. While showing great qualitative and even quantitative agreement with data, it still shows that there is work to do to accurately model LFP. One of the main areas that needs focus is the single particle modeling. A full 3D single particle model that addresses coherency strain as well as surface wetting is needed to better understand the active and inactive facets during lithiation and delithiation. Using this information, important effects can be included into the porous electrode model.

Another potentially important feature of LFP that needs to be researched is electron conduction. LFP is a poor electron conductor, which is why carbon coated LFP particles perform so much better than non-coated particles. [113] These coatings aren't necessarily uniform, though, and more research on the effect of electron

conduction in the surfaces needs to be done.

A third area of research for LFP is the reaction rate. The reaction rate used in MPET, which is a self consistent formulation, is dependent on understanding the material as well as how the reaction proceeds (namely the transition state). To date, not much is understood about the charge transfer kinetics of LFP, including the energy of the transition state. Additionally, it is unknown if there are any rearrangement energies that require Marcus theory to address [94], which could also affect the charge transfer coefficient. As research continues, these questions will be answered and provide better insight into how lithiation occurs in LFP and potentially how it can be improved even further.

Chapter 9

Conclusion

The overall goal of this thesis was to build a thermodynamically self-consistent framework for modeling lithium-ion batteries. The motivation for this is phase separating materials, which previously required artificial insertion of phase interfaces and other effects. Modified Porous Electrode Theory accomplishes this goal. It provides a consistent approach to modeling lithium transport in the electrolyte, the solid, as well as a consistent approach to modeling the open circuit potential and charge transfer kinetics. However, this isn't the end of this research. In fact, it has only just begun.

In our quest to create this framework, we have included additional energetic effects inside our intercalation materials that tend to yield more questions than answers. More complicated effects, such as surface wetting and coherency strain in $LiFePO_4$, are required to explain the complicated dynamics, and this is only material. Many other battery materials demonstrate different phenomena including phase transformations over a narrow range of lithium concentrations, multiple phase transformations (as demonstrated for graphite), and zero coherency strain. The MPET framework provides the necessary equations to simulate discharge of these complicated materials, however, a thorough understanding of the material itself, including various material property energies, is required first. Once these things are known, though, MPET has the ability to not only capture complicated dynamics, but also predict non-equilibrium dynamics of the material.

This thesis work has demonstrated the ability of the model to explain the voltage

gap in LFP, capture multiple phase separations in graphite, and qualitatively explain charge and discharge lithiation in an LFP electrode. As the research progresses, the understanding of these materials will improve, enabling researchers to build better performing batteries by exploiting particle properties as well as particle-particle interactions.

Bibliography

[1] *Handbook of Battery Materials*. Wiley, 2 edition, 2011.

[2] S.M. Allen and J.W. Cahn. Microscopic theory for antiphase boundary motion and its application to antiphase domain coarsening. *Acta Metallurgica*, 27:1085–1095, 1979.

[3] Pankaj Arora, Marc Doyle, Antoni S. Gozdz, Ralph E. White, and John Newman. Comparison between computer simulations and experimental data for high-rate discharges of plastic lithium-ion batteries. *Journal of Power Sources*, 88:219–231, 2000.

[4] Uri M. Ascher and Linda R. Petzold. *Computer methods for ordinary differential equations and differential-algebraic equations*. Society for Industrial and Applied Mathematics, 1998.

[5] H. Assadi. Phase-field modelling of electro-deoxidation in molten salt. *Modelling and Simulation in Materials Science and Engineering*, 14:963–974, 2006.

[6] S. Atlung, K. West, and T. Jacobsen. Dynamic aspects of solid solution cathodes for electrochemical power sources. *Journal of the Electrochemical Society*, 126(8), 1979.

[7] Ali Awarkea, Sven Lauerb, Stefan Pischingera, and Michael Wittlera. Percolation-tunneling modeling for the study of the electric conductivity in $LiFePO_4$ based li-ion battery cathodes. *Journal of Power Sources*, 196:405–411, 2011.

[8] Peng Bai, Daniel Cogswell, and Martin Z. Bazant. Suppression of phase separation in $LiFePO_4$ nanoparticles during battery discharge. *Nano Letters*, 11(11):4890–4896, 2011.

[9] N. Balke, S. Jesse, A. N. Morozovska, E. Eliseev, D. W. Chung, Y. Kim, L. Adamczyk, R. E. Garca, N. Dudney, and S. V. Kalinin. Nanoscale mapping of ion diffusion in a lithium-ion battery cathode. *Nature Nanotechnology*, 5, 2010.

[10] Robert W. Balluffi, Samuel M. Allen, and W. Craig Carter. *Kinetics of materials*. Wiley, 2005.

[11] M. Z. Bazant. *Mathematical Modeling of Electrochemical Energy Systems*. Massachusetts Institute of Technology, 2009. lecture notes for subject 10.95.

[12] M. Z. Bazant. *10.626 Electrochemical Energy Systems*. Massachusetts Institute of Technology: MIT OpenCourseWare, http://ocw.mit.edu, License: Creative Commons BY-NC-SA, 2011.

[13] M. Z. Bazant. Theory of chemical kinetics and charge transfer based on nonequilibrium thermodynamics. *Accounts of Chemical Research*, 46:1144–1160, 2013.

[14] M. Z. Bazant, K. T. Chu, and B. J. Bayly. Current-voltage relations for electrochemical thin films. *SIAM Journal on Applied Mathematics*, 65:1463–1484, 2005.

[15] M. Z. Bazant, M. S. Kilic, B. D. Storey, and A. Ajdari. Nonlinear electrokinetics at large voltages. *New Journal of Physics*, 11:075016, 2009.

[16] M. Z. Bazant, M. S. Kilic, B.D. Storey, and A. Ajdari. Towards an understanding of nonlinear electrokinetics at large voltages in concentrated solutions. *Advances in Colloid and Interface Science*, 152:48–88, 2009.

[17] M. Z. Bazant, B. D. Storey, and A. A. Kornyshev. Double layer in ionic liquids: Overscreening versus crowding. *Physical Review Letters*, 106:046102, 2011.

[18] M. Z. Bazant, K. Thornton, and A. Ajdari. Diffuse charge dynamics in electrochemical systems. *Physical Review E*, 70:021506, 2004.

[19] P. M. Biesheuvel, A. A. Franco, and M. Z. Bazant. Diffuse-charge effects in fuel-cell membranes. *Journal of the Electrochemical Society*, 156:B225–B233, 2009.

[20] P. M. Biesheuvel and J. Lyklema. Sedimentation–diffusion equilibrium of binary mixtures of charged colloids including volume effects. *Journal of Physics: Condensed Matter*, 17:6337, 2005.

[21] P. M. Biesheuvel and M. van Soestbergen. Counterion volume effects in mixed electrical double layers. *Journal of Colloid and Interface Science*, 316:490–499, 2007.

[22] P.M. Biesheuvel and M.Z. Bazant. Nonlinear dynamics of capacitive charging and desalination by porous electrodes. *Physical Review E*, 81, 2010.

[23] P.M. Biesheuvel, Y. Fu, and M.Z. Bazant. Diffuse charge and faradaic reactions in porous electrodes. *Physical Review E*, 83, 2011.

[24] P.M. Biesheuvel, Y. Fu, and M.Z. Bazant. Electrochemistry and capacitive charging of porous electrodes in asymmetric multicomponent electrolytes. *Russian Journal of Electrochemistry*, 2012.

[25] P.M. Biesheuvel, R. Zhao, S. Porada, and A. van der Wal. Theory of membrane capacitive deionization including the effect of the electrode pore space. *Journal of Colloid and Interface Science*, 360:239–248, 2011.

[26] W.J. Boettinger, S.R. Coriell, A.L. Greer, A. Karma, W. Kurz, M. Rappaz, and R. Trivedi. Solidification microstructures: Recent developments, future directions. *Acta Materialia*, 48:43–70, 2000.

[27] W.J. Boettinger and J.A. Warren. The phase-field method: Simulation of alloy dendritic solidification during recalescence. *Metallurgical and Materials Transactions A*, 27:657–669, 1996.

[28] W.J. Boettinger, J.A. Warren, C. Beckermann, and A. Karma. Phase-field simulation of solidification. *Annual Review of Materials Research*, 32:163–194, 2002.

[29] A. Bonnefont, F. Argoul, and M.Z. Bazant. Analysis of diffuse-layer effects on time-dependent interfacial kinetics. *Journal of Electroanalytical Chemistry*, 500:52–61, 2001.

[30] D.A.G. Bruggeman. Berechnung verschiedener physikalischer konstanten von heterogenen substanzen. *Annalen der Physik*, 1935.

[31] Damian Burch. *Intercalation Dynamics in Lithium-Ion Batteries*. Ph.D. Thesis in Mathematics, Massachusetts Institute of Technology, 2009.

[32] Damian Burch and Martin Z. Bazant. Size-dependent spinodal and miscibility gaps for intercalation in nanoparticles. *Nano Letters*, 9(11):3795–3800, 2009.

[33] Damian Burch, Gogi Singh, Gerbrand Ceder, and Martin Z. Bazant. Phase-transformation wave dynamics $LiFePO_4$. *Solid State Phenomena*, 139:95–100, 2008.

[34] J. W. Cahn and J. W. Hilliard. Free energy of a non-uniform system: I. interfacial energy. *Journal of Chemical Physics*, 28:258–267, 1958.

[35] John Cahn. Free energy of a nonuniform system. ii. thermodynamic basis. *Journal of Chemical Physics*, 30(5):1121–1124, 1959.

[36] John Cahn. On spinodal decomposition. *Acta Metallurgica*, 9(9):795–801, 1961.

[37] John Cahn. Coherent fluctuations and nucleation in isotropic solids. *Acta Metallurgica*, 10, 1962.

[38] John Cahn. On spinodal decomposition in cubic crystals. *Acta Metallurgica*, 10, 1962.

[39] John Cahn and John Hilliard. Free energy of a nonuniform system. iii. nucleation in a two-component incompressible fluid. *Journal of Chemical Physics*, 31(3):688–699, 1959.

[40] G. Ceder, Y.-M. Chiang, D.R. Sadoway, M.K. Aydinol, Y.-I. Jang, and B. Huang. Identification of cathode materials for lithium batteries guided by first-principles calculations. *Nature*, 392:694–696, 1998.

[41] Guoying Chen, Xiangyun Song, and Thomas Richardson. Electron microscopy study of the $LiFePO_4$ to $FePO_4$ phase transition. *Electrochemical and Solid State Letters*, 9(6):A295–A298, 2006.

[42] L. Q. Chen. Phase-field models for microstructural evolution. *Annual Review of Materials Research*, 32:113–140, 2002.

[43] William C Chueh, Farid El Gabaly, Josh D Sugar, Norman C. Bartelt, Anthony H. McDaniel, Kyle R Fenton, Kevin R. Zavadil, Tolek Tyliszczak, Wei Lai, and Kevin F. McCarty. Intercalation pathway in many-particle $LiFePO_4$ electrode revealed by nanoscale state-of-charge mapping. *Nano Letters*, 13:866 – 872, 2013.

[44] D. A. Cogswell and M. Z. Bazant. Theory of coherent nucleation in phase-separating nanoparticles. *Nano Letters*, Article ASAP, 2013.

[45] Daniel A. Cogswell and Martin Z. Bazant. Coherency strain and the kinetics of phase separation in $LiFePO_4$ nanoparticles. *ACS Nano*, 6:2215–2225, 2012.

[46] S. Dargaville and T.W. Farrell. Predicting active material utilization in $LiFePO_4$ electrodes using a multiscale mathematical model. *Journal of the Electrochemical Society*, 157(7):A830–A840, 2010.

[47] R. de Levie. On porous electrodes in electrolyte solutions. *Electrochimica Acta*, 8:751–780, 1963.

[48] R. de Levie. On porous electrodes in electrolyte solutions - iv. *Electrochimica Acta*, 9:1231–1245, 1964.

[49] C. Delmas, M. Maccario, L. Croguennec, F. Le Cras, and F. Weill. Lithium deintercalation of $LiFePO_4$ nanoparticles via a domino-cascade model. *Nature Materials*, 7:665–671, 2008.

[50] Pauline DeVidts and Ralph E. White. Governing equations for transport in porous electrodes. *Journal of the Electrochemical Society*, 144(4), 1997.

[51] Marc Doyle, Thomas F. Fuller, and John Newman. Modeling of galvanostatic charge and discharge of the lithium/polymer/insertion cell. *Journal of the Electrochemical Society*, 140(6):1526–1533, 1993.

[52] Marc Doyle, Antoni S. Gozdz, Caroline N. Schmuts, Jean-Marie Tarascon, and John Newman. Comparison of modeling predictions with experimental data from plastic lithium ion cells. *Journal of the Electrochemical Society*, 143(6), 1996.

[53] D. Dreyer, C. Guhlke, and R. Huth. The behavior of a many-particle electrode in a lithium-ion battery. *Physica D*, 240:1008–1019, 2011.

[54] Wolfgang Dreyer, Janko Jamnik, Clemens Guhlke, Robert Huth, Joze Moskon, and Miran Gaberscek. The thermodynamic origin of hysteresis in insertion batteries. *Nature Materials*, 9:448–453, 2010.

[55] M. Eikerling, A. A. Kornyshev, and E. Lust. Optimized structured of nanoporous carbonbased double-layer capacitors. *Journal of the Electrochemical Society*, 152:E24, 2005.

[56] Moses Ender, Todd R. Ferguson, Raymond B. Smith, and Martin Z. Bazant. In preparation, 2013.

[57] J. Euler and W. Nonnenmacher. Current distribution in porous electrodes. *Electrochimica Acta*, 2:268–286, 1960.

[58] T. R. Ferguson and M. Z. Bazant. Non-equilibrium thermodynamics of porous electrodes. *Journal of the Electrochemical Society*, 159:A1967–A1985, 2012.

[59] Thomas Fuller, Marc Doyle, and John Newman. Simulation and optimization of the dual lithium ion insertion cell. *Journal of the Electrochemical Society*, 141(1):1–10, 1994.

[60] R. Edwin Garcia and Yet-Ming Chiang. Spatially resolved modeling of microstructurally complex battery architectures. *Journal of the Electrochemical Society*, 154(9):A856–A864, 2007.

[61] R. Edwin Garcia, Yet-Ming Chiang, W. Craig Carter, Pimpa Limthongkul, and Catherine M. Bishop. Microstructural modeling and design of rechargeable lithium-ion batteries. *Journal of the Electrochemical Society*, 152(1):A255–A263, 2005.

[62] S. R. De Groot and P. Mazur. *Non-equilibrium Thermodynamics*. Interscience Publishers, Inc., New York, NY, 1962.

[63] I.G. Gurevich and V.S. Bagotzky. Steady-state operation of a porous electrode polarized from one side with diffusion supply of liquid reactants from both sides. *Electrochimica Acta*, 12:593–614, 1967.

[64] J. E. Guyer, W. J. Boettinger, J. A. Warren, and G. B. McFadden. Phase field modeling of electrochemistry i: Equilibrium. *Physical Review E*, 69:021603, 2004.

[65] J. E. Guyer, W. J. Boettinger, J. A. Warren, and G. B. McFadden. Phase field modeling of electrochemistry ii: Kinetics. *Physical Review E*, 69:021604, 2004.

[66] B.C. Han, A. Van der Ven, D. Morgan, and G. Ceder. Electrochemical modeling of intercalation processes with phase field models. *Electrochimica Acta*, 49:4691–4699, 2004.

[67] Stephen J. Harris, Adam Timmons, Daniel R. Baker, and Charles Monroe. Direct in situ measurements of li transport in li-ion battery negative electrodes. *Chemical Physics Letters*, 485:265–274, 2010. Video of experiment available at `http://lithiumbatteryresearch.com/`.

[68] Kuei-Feng Hsu, Sun-Yuan Tsay, and Bing-Joe Hwang. Synthesis and characterization of nano-sized $LiFePO_4$ cathode materials prepared by a citric acid-based sol-gel route. *Journal of Materials Chemistry*, 14:2690–2695, 2004.

[69] H. Huang, S.C.Yin, and L.F. Nazar. Approaching theoretical capacity of $LiFePO_4$ at room temperature at high rates. *Electrochemical and Solid State Letters*, 4(10):A170–A172, 2001.

[70] R. A. Huggins. *Advanced Batteries: Materials Science Aspects*. Springer, 2009.

[71] E.A. Grens II. On the assumptions underlying theoretical models for flooded porous electrodes. *Electrochimica Acta*, 15:1047–1057, 1970.

[72] E.A. Grens II and C.W. Tobias. The influence of electrode reaction kinetics on the polarization of flooded porous electrodes. *Electrochimica Acta*, 10:761–772, 1965.

[73] E. M. Itskovich, A. A. Kornyshev, and M. A. Vorotyntsev. Electric current across the metal-solid electrolyte interface. i. direct current, current-voltage characteristic. *Physica Status Solidi (a)*, 39:229–238, 1977.

[74] J. Jamnik and J. Maier. Generalised equivalent circuits for mass and charge transport : chemical capacitance and its implications. *Physical Chemistry Chemical Physics*, 3:1668–1678, 2001.

[75] A. M. Johnson and John Newman. Desalting by means of porous carbon electrodes. *Journal of the Electrochemical Society*, 118:510–517, 1971.

[76] Byoungwoo Kang and Gerbrand Ceder. Battery materials for ultrafast charging and discharging. *Nature*, 458:190–193, 2009.

[77] A. Karma. Phase-field model of eutectic growth. *Physical Review E*, 49:2245–2250, 1994.

[78] Dirk Kehrwald, Paul R. Shearing, Nigel P. Brandon, Puneet K. Sinha, and Stephen J. Harris. Local tortuosity inhomogeneities in a lithium battery composite electrode. *Journal of the Electrochemical Society*, 158(12):A1393–A1399, 2011.

[79] M. S. Kilic, M. Z. Bazant, and A. Ajdari. Steric effects in the dynamics of electrolytes at large applied voltages: I double-layer charging. *Physical Review E*, 75:021502, 2007.

[80] M. S. Kilic, M. Z. Bazant, and A. Ajdari. Steric effects on the dynamics of electrolytes at large applied voltages: II modified nernst-planck equations. *Physical Review E*, 75:021503, 2007.

[81] A. A. Kornyshev and M. A. Vorotyntsev. Conductivity and space charge phenomena in solid electrolytes with one mobile charge carrier species, a review with original material. *Electrochimica Acta*, 26:303–323, 1981.

[82] O.S. Ksenzhek. Macrokinetics of processes on porous electrodes. *Electrochimica Acta*, 9:629–637, 1964.

[83] O.S. Ksenzhek and V.V. Stender. *Doklady Akademiia nauk SSSR*, 106:486, 1956.

[84] O.S. Ksenzhek and V.V. Stender. *Doklady Akademiia nauk SSSR*, 107:280, 1956.

[85] O.S. Ksenzhek and V.V. Stender. *Zhurnal prikladnoi khimii*, 32:110, 1959.

[86] Karthikeyan Kumaresan, Yuriy Mikhaylik, and Ralph E. White. A mathematical model for a lithium-sulfur cell. *Journal of The Electrochemical Society*, 155:A576–A582, 2008.

[87] W. Lai and F. Ciucci. Thermodynamics and kinetics of phase transformation in intercalation battery electrodes - phenomenological modeling. *Electrochimica Acta*, 56:531–542, 2010.

[88] W. Lai and S. M. Haile. Impedance spectroscopy as a tool for chemical and electrochemical analysis of mixed conductors: A case study of ceria. *Journal of the American Ceramic Society*, 88:2979–2997, 2005.

[89] Wei Lai. Electrochemical modeling of single particle intercalation battery materials with different thermodynamics. *Journal of Power Sources*, 196:6534–6553, 2011.

[90] Wei Lai and Francesco Ciucci. Mathematical modeling of porous battery electrodes - revisit of newman's model. *Electrochimica Acta*, 56:4369–4377, 2011.

[91] Yiyang Li, Todd R. Ferguson, Raymond B. Smith, Martin Z. Bazant, and William Chueh. In preparation, 2013.

[92] Rahul Malik, Damian Burch, Martin Bazant, and Gerbrand Ceder. Particle size dependence of the ionic diffusivity. *Nano Letters*, 10:4123–4127, 2010.

[93] Rahul Malik, Fei Zhou, and Gerbrand Ceder. Kinetics of non-equilibrium lithium incorporation in $LiFePO_4$. *Nature Materials*, 10:587–590, 2011.

[94] R. A. Marcus. Electron transfer reactions in chemistry. theory and experiment. *Reviews of Modern Physics*, 65:599–610, 1993.

[95] Graeme Walter Milton. *The Theory of Composites*. Cambridge University Press, 2002.

[96] D. Morgan, A. Van der Ven, and G. Ceder. Li conductivity in Li_xMPO_4 (m=mn,fe,co,ni) olivine materials. *Electrochemical and Solid State Letters*, 7(2):A30–A32, 2004.

[97] E. Bruce Nauman and D. Qiwei Heb. Nonlinear diffusion and phase separation. *Chemical Engineering Science*, 56:1999–2018, 2001.

[98] John Newman and Karen E. Thomas-Alyea. *Electrochemical Systems*. Prentice-Hall, Inc., Englewood Cliffs, NJ, third edition, 2004.

[99] John Newman and William Tiedemann. Porous-electrode theory with battery applications. *AIChE Journal*, 21(1):25–41, 1975.

[100] John Newman and Charles Tobias. Theoretical analysis of current distribution in porous electrodes. *Journal of The Electrochemical Society*, 109(12):1183–1191, 1962.

[101] Tsutomu Ohzuku, Yasunobu Iwakoshi, and Keijiro Sawai. Formation of lithium-graphite intercalation compounds in nonaqueous electrolytes and their application as a negative electrode for a lithium ion (shuttlecock) cell. *Journal of the Electrochemical Society*, 140:2490–2498, 1993.

[102] L. H. Olesen, M. Z. Bazant, and H. Bruus. Strongly nonlinear dynamics of electrolytes in large ac voltages. *Physical Review E*, 82:011501, 2010.

[103] Gosuke Oyama, Yuki Yamada, Ryuichi Natsui, Shinichi Nishimura, and Atsuo Yamada. Kinetics of nucleation and growth in two-phase electrochemical reaction of $LiFePO_4$. *The Journal of Physical Chemistry C*, 116:7306–7311, 2012.

[104] A.K. Padhi, K.S. Nanjundaswamy, and J.B. Goodenough. Phospho-olivines as positive-electrode materials for rechargeable lithium batteries. *Journal of the Electrochemical Society*, 144(4):1188–1194, 1997.

[105] Mauro Pasquali, Alessandro DellEra, and Pier Paolo Prosini. Fitting of the voltage-li+ insertion curve of $LiFePO_4$. *Journal of Solid State Electrochemistry*, 13:1859–1865, 2009.

[106] E. E. Petersen. Diffusion in a pore of varying cross section. *AIChE Journal*, 4:343–345, 1958.

[107] R. Pollard and J. Newman. Transient behavior of porous electrodes with high exchange current densities. *Electrochimica Acta*, 25:315–321, 1980.

[108] W. Pongsaksawad, A. C. Powell, and D. Dussault. Phase-field modeling of transport-limited electrolysis in solid and liquid states. *Journal of The Electrochemical Society*, pages F122–F133, 2007.

[109] S. Porada, L. Weinstein, R. Dash, A. van der Wal, M. Bryjak, Y. Gogotsi, and P.M. Biesheuvel. Water desalination using capacitive deionization with microporous carbon electrodes. *ACS Applied Materials and Interfaces*, 4:1194–1199, 2012.

[110] David V. Ragone. *Thermodynamics of Materials: Volume 1.* John Wiley and Sons, Inc., 1995.

[111] Venkatasailanathan Ramadesigan, Paul W. C. Northrop, Sumitava De, Shriram Santhanagopalan, Richard D. Braatz, and Venkat R. Subramanian. Modeling and simulation of lithium-ion batteries from a systems engineering perspective. *Journal of The Electrochemical Society*, 159:R31–R45, 2012.

[112] S.K. Rangarajan. Theory of flooded porous electrodes. *Electroanalytical Chemistry and Interfacial Electrochemistry*, 22:89–104, 1969.

[113] N. Ravet, Y. Chouinard, J.F. Morgan, S. Besner, M. Gauthier, and M. Armand. Electroactivity of natural and synthetic triphylite. *Journal of Power Sources*, 97-98:503–507, 2001.

[114] Muhammad Sahimi. *Heterogeneous Materials I Linear Transport and Optical Properties*, volume 22 of *Interdisciplinary Applied Mathematics*. Springer, 2003.

[115] Kuppan Saravanan, Palani Balaya, M.V. Reddy, B.V.R Chowdar, and Jagadese J. Vittal. Morphology controlled sythesis of lifepo$_4$/c nanoplates for li-ion batteries. *Energy and Environmental Science*, 3:457–464, 2010.

[116] Lawrence F. Shampine and Mark W. Reichelt. The matlab ode suite. *SIAM Journal on Scientific Computing*, 18(1):1–22, 1997.

[117] Lihua Shen and Zhangxin Chen. Critical review of the impact of tortuosity on diffusion. *Chemical Engineering Science*, 62:3748 – 3755, 2007.

[118] Y. Shibuta, Y. Okajima, and T. Suzuki. A phase-field simulation of bridge formation process in a nanometer-scale switch. *Scripta Materialia*, 55:1095–1098, 2006.

[119] G. K. Singh, M. Z. Bazant, and G. Ceder. Anisotropic surface reaction limited phase transformation dynamics in $LiFePO_4$. arXiv:0707.1858v1 [cond-mat.mtrl-sci], 2007.

[120] Gogi Singh, Gerbrand Ceder, and Martin Z. Bazant. Intercalation dynamics in rechargeable battery materials: General theory and phase-transformation waves in $LiFePO_4$. *Electrochimica Acta*, 53:7599–7613, 2008.

[121] Kyle C. Smith, Partha P. Mukherjee, and Timothy S. Fisher. Columnar order in jammed $LiFePO_4$ cathodes: ion transport catastrophe and its mitigation. *Physical Chemistry Chemical Physics*, 14:7040–7050, 2012.

[122] Madeleine Smith, R. Edwin Garcia, and Quinn C. Horn. The effect of microstucture on the galvanostatic discharge of graphite anode electrodes in $LiCoO_2$-based rocking-chair rechargeable batteries. *Journal of the Electrochemical Society*, 156(11):A896–A904, 2009.

[123] Venkat Srinivasan and John Newman. Discharge model for the lithium iron-phosphate electrode. *Journal of the Electrochemical Society*, 151(101):A1517–A1529, 2004.

[124] D. Stauffer and A. Aharony. *Introduction to Percolation Theory*. CRC Press, 1994.

[125] Sarah G. Stewart and John Newman. The use of uv/vis absorption to measure diffusion coefficients in lipf$_6$ electrolytic solutions. *Journal of the Electrochemical Society*, 155:F13–F16.

[126] B. D. Storey, Lee R. Edwards, M. S. Kilic, and M. Z. Bazant. Steric effects on ac electro-osmosis in dilute electrolytes. *Physical Review E*, 77:036317, 2008.

[127] Ke Sun and Shen J. Dillon. A mechanism for the improved rate capability of cathodes by lithium phosphate surficial films. *Electrochemistry Communications*, 13:200–202, 2011.

[128] Ming Tang, James F. Belak, and Milo R. Dorr. Anisotropic phase boundary morphology in nanoscale olivine electrode particles. *The Journal of Physical Chemistry C*, 115:4922–4926, 2011.

[129] J.M. Tarascon and M. Armand. Issues and challenges facing rechargeable lithium batteries. *Nature*, 414:359–367, 2001.

[130] Jefferson W. Tester and Michael Modell. *Thermodynamics and its applications*. Prentice Hall PTR, 3 edition, 1997.

[131] Ralf Theidmann, Ole Stenzel, Aaron Spettl, Paul R. Shearing, Stephen J. Harris, Nigel P. Brandon, and Volder Schmidt. Stochastic simulation model for the 3d morphology of composite materials in Li-ion batteries. *Computational Materials Science*, 50:3365–3376, 2011.

[132] Indrajeet V. Thorat, Tapesh Joshi, Karim Zaghib, John N. Harb, and Dean R. Wheeler. Understanding rate-limiting mechanisms in lifepo4 cathodes for li-ion batteries. *Journal of the Electrochemical Society*, 158(11):A1185–A1193, 2011.

[133] Indrajeet V. Thorat, David E. Stephenson Nathan A. Zacharias, Karim Zaghib, John N. Harb, and Dean R. Wheeler. Quantifying tortuosity in porous Li-ion battery materials. *Journal of Power Sources*, 188:592–600, 2009.

[134] William Tiedemann and John Newman. Double-layer capacity determination of porous electrodes. *Journal of the Electrochemical Society*, 122(1):70–74, 1975.

[135] Salvatore Torquato. *Random Heterogeneous Materials Microstructure and Macroscopic Properties*, volume 16 of *Interdisciplinary Applied Mathematics*. Springer, 2002.

[136] Lars Ole Valoen and Jan N. Reimers. Transport properties of lipf6-based li-ion battery electrolytes. *Journal of the Electrochemical Society*, 152(5):A882–A891, 2005.

[137] Katja Weichert, Wilfried Sigle, Peter A. van Aken, Janez Jamnik, Changbao Zhu, Ruhul Amin, Tolga Acarturk, Ulrich Starke, and Joachim Maier. Phase boundary propagation in large $LiFePO_4$ single crystals on delithiation. *Journal of the American Chemical Society*, 134:2988–2992, 2012.

[138] K. West, T. Jacobsen, and S. Atlung. Modeling of porous insertion electroes with liquid electrolyte. *Electrochemical Science and Technology*, 129(7):1480–1485, 1982.

[139] Yujie Zhu and Chunsheng Wang. Galvanostatic intermittent titration technique for phase-transformation electrodes. *Journal of Physical Chemistry C*, 114:2830–2841, 2010.